

## Thèse

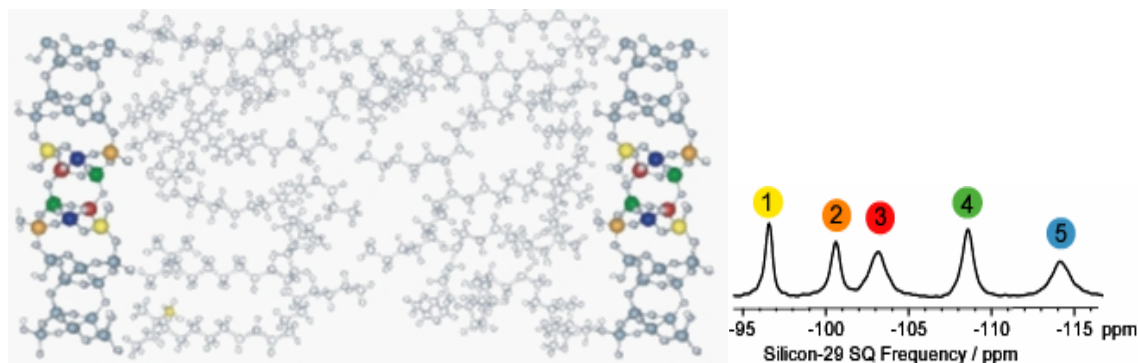
En vue d'obtenir le grade de :  
**Docteur de l'Ecole Normale Supérieure de Lyon**  
**Spécialité Chimie**

Ecole doctorale de Chimie de Lyon.  
Ecole Normale Supérieure de Lyon, Laboratoire de Chimie – UMR 5182  
CNRS/ENSL

Présentée et soutenue publiquement le 20 Septembre 2007 par Monsieur :

**Nicolas MIFSUD**

# ***Structure Determination in Ordered and Disordered Solids by High-Resolution NMR Spectroscopy***



Directeur de thèse :

Prof. Lyndon EMSLEY

Après avis de :

Dr. Michel BARDET, Rapporteur  
Prof. Dominique MASSIOT, Rapporteur

Commission d'examen :

Dr. Michel BARDET, Rapporteur  
Dr. Steven P. BROWN, Membre  
Prof. Stefano CALDARELLI, Membre  
Prof. Lyndon EMSLEY, Membre  
Prof. Dominique MASSIOT, Rapporteur



<b>Acknowledgements</b>	6
<b>Abstract</b>	8
<b>Resume</b>	10
<b>General Introduction</b>	12
<b>References</b>	18
<b>Part A. Small Organic Molecules: Towards NMR Crystallography</b>	20
<b>Introduction</b>	20
<b>A.1. Review of Proton Spectroscopy in Solids</b>	22
A.1.1. Introduction	22
A.1.2. NMR Line Shapes	23
A.1.3. Homonuclear Dipolar Decoupling	30
A.1.4. Conclusion	34
<b>A.2. Assigning Powders to Crystal Structures</b>	35
A.2.1. Introduction	35
A.2.2. Proton Correlation Spectroscopy – DQ CRAMPS	38
A.2.2.1 Introduction	38
A.2.2. Experimental Results	41
A.2.3. Trough-Bond Spectroscopy – INEPT	43
A.2.3.1. Introduction	43
A.2.3.2. Experimental Results	46
A.2.4. Crystal Structure by First Principle Calculations	48
A.2.4.1. Introduction	48
A.2.4.2. Results	50
2.5. Conclusion	56
<b>A.3. Molecular Structure Determination in Powders</b>	57
A.3.1. Introduction	57
A.3.2. Proton-Proton Spin Diffusion	61
A.3.2.1. Introduction	61
A.3.2.2. Experimental	63
A.3.3. Introduction to Xplor-NIH	68
A.3.4. Structure Determination	69
A.3.4.1. Combined PSD and Molecular Modeling	69
A.3.4.2. Results and Discussion	75

A.3.5. Perspectives	83
<b>A.4. Conclusion</b>	84
<b>A.5. References</b>	85
<b>Part B. Silicate Framework Materials</b>	99
<b>B.1. Generalities on Disordered Solids</b>	99
B.1.1. Introduction	99
B.1.2. Order / Disorder in NMR	101
B.1.2.1. Review	101
B.1.2.2. Order / Disorder in surfactant-templated layered silicates	106
B.1.3. Through Bond Spectroscopy – INADEQUATE	110
B.1.3.1. Introduction	110
B.1.3.2. The refocused INADEQUATE experiment	114
<b>B.2. Analysis of NMR Lineshapes</b>	125
B.2.1. Primary results – Temperature dependence	125
B.2.2. Homogeneous and inhomogeneous broadening via INADEQUATE experiment	127
B.2.3. Results	131
<b>B.3. Characterizing Chemical Exchange in Disordered Solids</b>	134
B.3.1. Experimental	134
B.3.2. Review on Chemical Exchange	138
B.3.3. Results	140
B.3.4. Discussion	142
<b>B.4. Characterizing Static Structural Disorder in Disordered Solids</b>	146
B.4.1. Extraction of Site to Site Chemical Shift Correlation Slopes	146
B.4.2. Static and Temperature-Dependent Disorder	148
B.4.2.1. Results	148
B.4.2.2. Discussion	155
B.4.3. Measuring ${}^2J({}^{29}\text{Si-O-}{}^{29}\text{Si})$ couplings in solid-state NMR	157
B.4.3.1. Introduction	157
B.4.3.2. Experimental	159
B.4.3.3. Results and Discussion	162
B.4.4. Distribution of ${}^2J_{\text{SiSi}}$ Couplings: Results and Interpretation	165

<b>B.5. Conclusion</b>	169
<b>B.6. References</b>	171
<b>General Conclusion</b>	178

# ACKNOWLEDGEMENTS

First and foremost, I would like to thank you, dear reader, to take some of your time to read this manuscript or maybe only part of it. In particular, I am grateful to Dr. Michel Bardet and Prof. Dominique Massiot who agreed to be the two referees of this dissertation. I also thank Dr. Steven Brown and Prof. Stefano Caldarelli for accepting to be members of my jury.

I am very grateful to my thesis director Prof. Lyndon Emsley who gave me the opportunity to do my PhD in his group. His large knowledge in science and his patience and advices were really helpful during these three years.

I also thank Dr. Anne Lesage whose strong competence and calm have made many things possible.

I thank particularly Dr. Benedicte Elena and Dr. Sylvian Cadars with whom I made my beginning in solid-state NMR and with whom I worked during these three years.

Then I thank all the members of the NMR group: Guido, Gwendal, Julien, Nicolas, Frederic, Benjamin, Elodie, Segolene, Marc, Sabine, Odile and Robin and the members of the IBCP group: Anja, Carole and Antoine with whom it was a pleasure to work and discuss.

I would also like to thank people I met in conferences for the discussions which were really helpful: Dr. Sasa Antonijevic, Prof. Geoffrey Bodenhausen, Prof.

Philip Grandinetti, Prof. Bradley Chmelka, Dr. Dimitris Sakellariou, Prof. Jean-Paul Amoureux, Dr. Stefan Steuernagel,...

Thank you to all the members of the “laboratoire de chimie de l’ENS-Lyon “ and especially to Prof. Philippe Sautet, Christian, Valerie, Stephanie, Fathia and Fatima for their precious help.

Enfin, je remercie ma famille et mes amis et particulièrement Vincent et Fabien pour leur soutien et leurs encouragements pour et hors travail.

# Abstract

Nuclear Magnetic Resonance is a potential powerful probe of structure and dynamics for a large range of materials in the solid-state. However, the resolution of proton spectra is the limiting factor due to strong  $^1\text{H}$ - $^1\text{H}$  dipolar couplings.

In this thesis, we show how powder samples at natural isotopic abundance can be assigned to crystal structures by using high-resolution proton and carbon-13 solid-state NMR spectra in combination with first principles calculations. Homonuclear proton double-quantum spectra in combination with through-bond proton-carbon HSQC spectra are used to assign the NMR spectra. We then show that the proton chemical shifts can be included in the process of assigning the spectra to a crystal structure using first principles calculations. The method is demonstrated on the K salt of penicillin G.

Similarly, the determination of the three-dimensional structure of an organic compound in powder form and at natural isotopic abundance is presented. It is obtained by an approach that combines molecular modeling with experimental spin diffusion data obtained from high-resolution solid-state nuclear magnetic resonance of protons.

Finally, temperature dependent  $^{29}\text{Si}$  NMR studies of the order and disorder in silicate framework materials are presented. Notably, we introduce and demonstrate the idea that Silicon-29 NMR transverse dephasing times can be used to probe dynamic processes independently of static disorder.

Moreover, lineshapes can be analyzed in terms of disorder. Specifically, temperature-dependent changes in the  $^{29}\text{Si}$  transverse dephasing times  $T_2'$  allow quantitative characterization of the two-fold reorientational dynamics of the surfactant headgroups. The reversible broadening of the  $^{29}\text{Si}$  NMR spectra at low temperature can not be explained by this chemical exchange process, so must be due to a change in local order.

A discussion of 2D correlation NMR lineshapes and their temperature dependence allows the demonstration that the temperature-dependent shifts, broadening of the  $^{29}\text{Si}$  NMR peaks, and the two-site  $^{29}\text{Si}$  chemical shift correlations result from a single physical process. We show that the  $^{29}\text{Si}$   $T_2'$  behavior can be explained on the basis of such a two-site exchange, where the  $^{29}\text{Si}$  nucleus acts as a spectator probe of the surfactant dynamics.

# Résumé

La résonance magnétique nucléaire du solide est un outil potentiellement puissant pour déterminer la structure et la dynamique d'une large variété de composés. Cependant, la résolution des spectres proton, qui est l'atome le plus abondant dans la plupart des composés, est limitée due à des couplages dipolaires proton-proton importants.

Dans cette thèse, nous montrons tout d'abord comment assigner un échantillon en poudre et en abondance isotopique naturelle telle que la pénicilline G sel de potassium à une structure cristalline en utilisant la RMN du solide haute résolution proton et carbone associée à des calculs théoriques. Les avantages des expériences  $^1\text{H}$ - $^1\text{H}$  DQ CRAMPS et INEPT-HSQC sont utilisés pour effectuer l'attribution de la molécule.

De même, la détermination de la structure tridimensionnelle d'un composé organique en poudre et en abondance isotopique naturelle est présentée. Elle est obtenue par une méthode qui combine modélisation moléculaire et données expérimentales de diffusion de spin proton haute résolution à l'état solide. L'interprétation des courbes de diffusion de spin proton permet ainsi de déterminer la position des protons de la molécule en complémentarité avec la diffraction par rayons X.

Enfin, une étude de la dynamique et du désordre structurel a été réalisée sur des matériaux composés de silice par l'intermédiaire de la RMN du silicium. Ainsi, on

montre que le temps de déphasage transverse  $T_2'$  du silicium peut être utilisé comme une sonde de la dynamique indépendamment du désordre statique. Il permet une caractérisation quantitative de la dynamique concernant la double réorientation de la tête du surfactant.

Cependant, l'élargissement réversible du spectre silicium à basse température ne peut pas être expliqué par ce procédé d'échange chimique et doit provenir d'un changement d'ordre local. Une interprétation des corrélations entre l'élargissement et le déplacement des pics du silicium suivant la température avec le déplacement chimique des pics 2D du silicium montre que l'origine est un procédé physique.

L'interprétation des mesures de couplage  $J$  montre que ce type de méthode ouvre de nouvelles voies pour la caractérisation du désordre structurel.

# GENERAL INTRODUCTION

NMR was discovered by Purcell<sup>1</sup> and Bloch<sup>2</sup> in 1945-46 and was considered, at its beginning, as a technique of limited interest. However, the discovery of the chemical shift interaction showed that the NMR signal is very sensitive to the local environment of the nucleus and thus its chemical shift<sup>3</sup>. In addition to that, in the early 1950s, another discovery was made: the scalar coupling interaction which arises from a coupling between nuclear spins via the electronic spins involved in the chemical bonds between the two nuclei. The J coupling proved to be strongly correlated to local structural parameters and become of crucial importance for NMR spectroscopy.

NMR sensitivity was poor until 1970s when Ernst showed that Fourier Transform NMR was an order of magnitude more sensitive. Since then with the technological advances and the development of 2D NMR techniques,<sup>4, 5</sup> both the sensitivity and resolution of NMR have greatly increased leading nowadays to the study of soluble proteins of tens of kDa. The domain of application of NMR is currently very large and goes from chemistry or structural biology to medical diagnostics with imaging or metabonomics, or in physics with the characterization of conductivity properties.

The case of solid-state NMR is different to that of solutions (where most NMR is done today) because molecular motion is largely absent in solids, leading to broad resonances and to very low sensitivity. To overcome these difficulties, Andrew, Lowe

and co-workers introduced the concept of magic angle spinning (MAS) in 1958<sup>6, 7</sup> using the description of the spatial part of the dominant anisotropic interactions in solids and in particular their  $(3\cos^2\theta - 1)$  dependence (where  $\theta$  is the angle between the principal axis of the interaction tensor and the static magnetic field). Thus, the rotation of a polycrystalline sample around the magic angle  $\theta=54.7^\circ$  leads in principle to an averaging to zero of the dipolar couplings and to the isotropic chemical shift value of the chemical shift anisotropy (CSA). Nevertheless, the technological limitation of spinning frequencies (around 70 kHz nowadays) sometimes leads to only partial averaging which can result in spinning sidebands and/or broadening due to residual couplings (Figure 1).

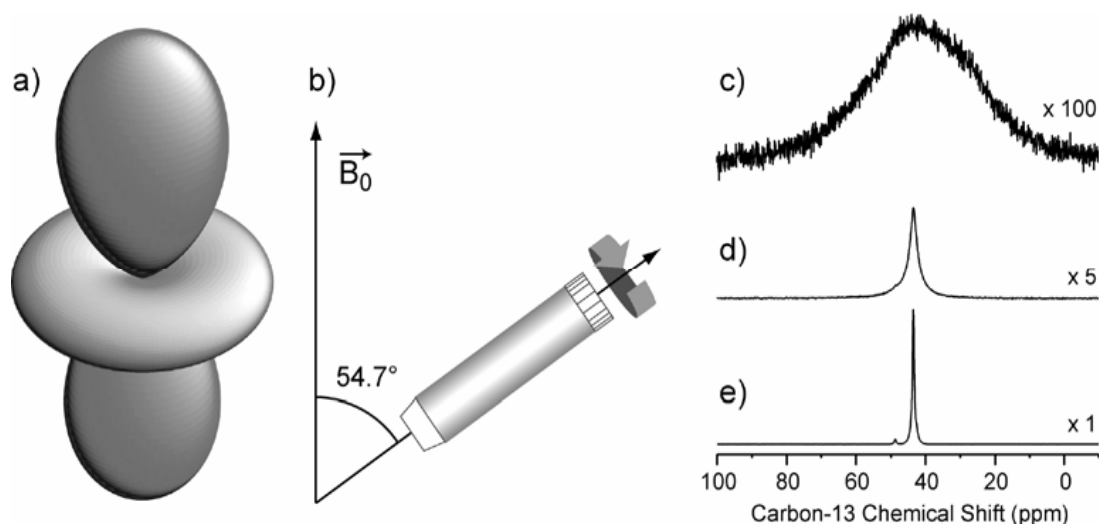


**Figure 1.** (a) Iso-surface showing the angular dependence of the spatial part of the anisotropic interactions. Dark grey represent positive values while light grey corresponds to negative values. (b) schematic representation of a rotor spinning at magic angle. (c, d & e) Comparison of one-dimensional (1D) single-pulse spectra of a sample of powdered glycine, being selectively  $^{13}\text{C}$ -labelled on the  $\text{CH}_2$  ( $\text{C}_\alpha$ ). (c) Static spectrum. (d) Spectrum recorded spinning the sample at 30 kHz at the magic angle. (e) Single-pulse spectrum obtained at 30 kHz MAS, applying continuous wave (CW) heteronuclear decoupling during acquisition, at a proton nutation frequency of 100 kHz.

Many other developments have been made over the past thirty years. For example, in 1973, Pines and co-workers<sup>8</sup> proposed the concept of cross polarization (CP) transfer which enables to transfer the large magnetization from protons having a high magnetogyric ratio to the less sensitive nuclei such as  $^{13}\text{C}$ ,  $^{15}\text{N}$  or  $^{29}\text{Si}$  for instance. This technique has three main advantages: it improves the sensitivity, it enables faster repetition delays due to much shorter limiting  $T_1$  of protons, and it allows efficient polarization transfer for multi-dimensional spectroscopy.

However, in organic solids in particular, the presence of abundant protons leads to a dense network of strong couplings that cannot be fully averaged out by MAS. As a consequence, additional methods are required for a more efficient averaging of the residual heteronuclear dipolar interactions under MAS, leading to technique such as heteronuclear decoupling. In solid-state NMR, the heteronuclear dipolar couplings are typically several orders of magnitude larger than heteronuclear J couplings and low power decoupling is therefore inefficient. As a consequence, high power continuous wave irradiation has been widely applied at proton nutation frequencies typically ranging from 50 to 150 kHz (which, in addition, limits the impact of off-resonance effects) (Figure 1.e).

For about a decade however, renewed interest has been found for the development of more sophisticated high power decoupling techniques in solids under MAS, since the introduction of the two-pulse phase modulated technique (TPPM)<sup>9</sup>. This technique consists in successive rf pulses of 180° (or near 180°) flip angle with alternate phase of typically  $\pm 15^\circ$ , and turned out to provide significantly increased efficiency and robustness with respect to offset effects compared to CW irradiation. Some variations of the TPPM scheme were proposed, which involve either phase or amplitude continuous/discrete modulations of the rf irradiation, the most successful methods being probably SPINAL64<sup>10</sup>, XiX<sup>11</sup>, and CM<sup>12</sup> decoupling. An important advance for heteronuclear decoupling has been proposed by de Paëpe *et al.* with the introduction of the principle of transverse dephasing optimization (TDOP)<sup>13, 14</sup>. The basic idea of this approach is that good decoupling schemes can easily lead to nearly identical apparent linewidths, whereas they may correspond to significantly different coherence lifetimes during a spin-echo. Thus, the quality of the heteronuclear

decoupling can be probed in an extremely sensitive way by measuring the signal intensity after a long spin-echo, which enables a fine optimization of a given decoupling scheme. This aspect is particularly relevant in the case of disordered solids, as will be discussed later.

Whereas NMR was rapidly accepted as a fundamental tool for identification and structural analysis of molecules in the liquid-state in most areas of chemistry, the technique was only recently adopted in this field as broadly applicable to solid-state materials<sup>15, 16</sup>. NMR has now proved to be suitable for probing the versatile nature of solid matter, from heterogeneous systems, locally disordered arrangements, to ordered crystalline structures, where in all cases dynamics at the molecular level can also be observed.

This thesis is with developing new methods for solid-state NMR.

The first chapter is concerned with the study of small organic molecules by solid-state NMR. The first section of chapter 1 briefly outlines the basic principles concerning proton spectroscopy in solids.

The second part of this chapter is dedicated to the assignment of powders to crystal structures. Through the use of proton correlation spectroscopy (DQ CRAMPS) and through-bond  $^1\text{H}$ - $^{13}\text{C}$  polarization transfer experiment (INEPT) in combination with first principles calculations, we show how powder samples at natural isotopic abundance can be assigned to crystal structures.

The third part of chapter 1 focuses on proton-proton high-resolution correlation experiments and their use for structural determination in crystalline solids. Through the analysis of 2D proton-proton spin diffusion CRAMPS experiments with a

phenomenological approach, based on a rate matrix analysis in combination with molecular modelling, we show the determination of the three dimensional structure of an organic compound in powder form and at natural isotopic abundance.

The second chapter is concerned with the study of dynamics and chemical exchange in silicate framework materials. The first section of this chapter gives a brief review of the literature on order and disorder in NMR and focuses more specifically on the refocused INADEQUATE technique.

The second part of chapter 2 shows that lineshapes can be analysed in terms of disorder.

Such correlation lineshapes are extremely rich in chemical information and we will see in the third section that temperature-dependent changes in the  $^{29}\text{Si}$  transverse dephasing times  $T_2'$  allow quantitative characterization of the two-fold reorientational dynamics of the surfactant headgroups. However, the reversible broadening of the  $^{29}\text{Si}$  NMR spectra at low temperature can not be explained by this chemical exchange process, so must be due to a change in local order and will be discussed in the next part.

In the fourth part of this chapter, we will turn our attention to the measurement of two bond silicon-silicon coupling across siloxane bridges  $^2J(\text{Si-O-Si})$  in partially  $^{29}\text{Si}$  enriched surfactant templated silicate layers lacking long range 3D crystallinity. Such correlation lineshapes can be analysed in terms of conditional probability matrices that are proved extremely sensitive to structure compared to one-dimensional chemical shift distributions.

## References

1. Purcell, E.M.; Torrey, H.C.; Pound, R.V., Resonance absorption by nuclear magnetic moments in a solid. *Phys. Rev.* 1946, 69 (1-2), 37-38.
2. Bloch, F.; Hansen, W.W.; Packard, M., The nuclear induction experiment. *Phys. Rev.* 1946, 70 (7-8), 474-485.
3. Ramsey, N.F., Magnetic shielding of nuclei in molecules. *Phys. Rev.* 1950, 78 (6), 699-703.
4. Ernst, R.R., 2-Dimensional spectroscopy. *Chimia.* 1975, 29 (4), 179-183.
5. Muller, L.; Kumar, A.; Ernst, R.R., 2-Dimensional C-13 NMR spectroscopy. *J. Chem. Phys.* 1975, 63 (12), 5490-5491.
6. Andrew, E.R.; Bradbury, A.; Eades, R.G., Nuclear magnetic resonance spectra from a crystal rotated at high speed. *Nature.* 1958, 182 (4650), 1659-1659.
7. Lowe, I.J., Free induction decays of rotating solids. *Phys. Rev. Lett.* 1959, 2 (7), 285-287.
8. Pines, A.; Gibby, M.G.; Waugh, J.S., Proton-enhanced NMR of dilute spins in solids. *J. Chem. Phys.* 1973, 59 (2), 569-590.
9. Bennett, A.E.; Rienstra, C.M.; Auger, M.; Lakshmi, K.V.; Griffin, R.G.J., Heteronuclear decoupling in rotating solids. *Chem. Phys.* 1995, 103 (16), 6951-6958.
10. Fung, B.M.; Khitrin, A.K.; Ermolaev, K., An improved broadband decoupling sequence for liquid crystals and solids. *J. Magn. Reson.* 2000, 142 (1), 97-101.
11. Detken, A.; Hardy, E.H.; Ernst, M.; Meier, B.H., Simple and efficient decoupling in magic-angle spinning solid-state NMR: the XiX scheme. *Chem. Phys. Lett.* 2002, 356 (3-4), 298-304.
12. De Paepe, G.; Elena, B.; Emsley, L., Characterization of heteronuclear decoupling through proton spin dynamics in solid-state nuclear magnetic resonance spectroscopy. *J. Chem. Phys.* 2004, 121 (7), 3165-3180.
13. De Paepe, G.; Giraud, N.; Lesage, A.; Hodgkinson, P.; Bockmann, A.; Emsley, L., Transverse dephasing optimized solid-state NMR spectroscopy. *J. Am. Chem. Soc.* 2003, 125 (46), 13938-13939.
14. De Paepe, G.; Lesage, A.; Steuernagel, S.; Emsley, L., Transverse dephasing optimised NMR spectroscopy in solids: Natural-abundance C-13 correlation spectra. *ChemPhysChem.* 2004, 5 (6), 869-875.

15. Brown, S.P.; Spiess, H.W., Advanced solid-state NMR methods for the elucidation of structure and dynamics of molecular, macromolecular, and supramolecular systems. *Advanced solid-state NMR methods for the elucidation of structure and dynamics of molecular, macromolecular, and supramolecular systems.* Chem. Rev. 2001, 101 (12), 4125-4155.

16. Laws, D.D.; Bitter, H.M.L.; Jerschow, A., Solid-state NMR spectroscopic methods in chemistry. *Solid-state NMR spectroscopic methods in chemistry.* Angew. Chem.-Int. Edit. 2002, 41 (17), 3096-3129.

# Part A. Small Organic Molecules: Towards NMR Crystallography

## Introduction

The ability to determine three-dimensional atomic or molecular structures by X-ray diffraction on single crystal samples is the keystone on which much of our understanding of chemistry has developed over the last century. Today single crystal diffraction methods (with either X-rays or neutrons) are capable of characterising systems as diverse as membrane proteins<sup>1, 2</sup>, whole virus particles<sup>3</sup>, complex inorganic materials<sup>4</sup>, supramolecular nanostructures<sup>5, 6</sup>, or even transient time-resolved structures<sup>7, 8</sup>.

In contrast, if the sample is a powder, structural characterisation represents an enormous challenge. Samples can be powders either because of their intrinsic nature (in the case of pharmaceutical preparations for example) or commonly because crystals large enough for diffraction cannot be formed. Such samples are becoming increasingly widespread, notably in the area of new materials, and the development of experimental methods to study the three dimensional atomic structure of powdered solids is thus an area of great current interest. Significant recent progress has been made in the application of X-ray and neutron diffraction methods<sup>9</sup>, and spectacular advances have been made in solid-state Nuclear Magnetic Resonance (NMR) methods for powdered solids<sup>10</sup>. This latter method has recently led to the first

determination of the three-dimensional structure of a powdered microcrystalline protein<sup>11</sup>, to structural models of amyloid fibrils<sup>12-14</sup>, and to models for extended inorganic framework structures<sup>15-18</sup>. Curiously, in some ways macromolecules are easier to handle by NMR than small molecular compounds. For example, macromolecules can often be treated without considering the crystalline environment, and sophisticated isotopic labelling schemes are available to facilitate spectral assignment and geometry measurements. However, structural studies of small molecules, especially at natural isotopic abundance, remain challenging.

Thus, solid-state NMR has identified itself as a valuable probe of local molecular structure, in particular because of its ability to accurately determine distances or identify close proximities between specific nuclei. Most solid-state NMR techniques, which exploit dipolar couplings in this way, probe rare spins such as <sup>13</sup>C and <sup>15</sup>N. However, the potential of techniques that directly probe <sup>1</sup>H-<sup>1</sup>H dipolar couplings is being increasingly recognized<sup>19-26</sup>.

In this chapter, we present two approaches for structure determination. In a first part, we describe proton double-quantum single-quantum CRAMPS correlation experiments and we emphasize their exploitability to characterize powders in terms of known structures with the help of the <sup>1</sup>H-<sup>13</sup>C INEPT through-bond coherence transfer technique and DFT calculations. In a second part, we describe how 2D proton-proton correlation spectra can be used for de novo structure characterization of powders.

# A.1. Review of Proton Spectroscopy in Solids

## A.1.1. Introduction

The exploration of solid and liquid-state spectroscopy principles, as well as experimental methodology cohabited from the first premises of NMR developments. As seen before, NMR has principally built its foundations on theory and investigation of solids, before large routes were opened towards applications of NMR for the characterization of molecules in solution. Protons have early become the ideal nuclei for NMR observation due to the omnipresence of protons in various types of organic and inorganic materials, their natural spin  $1/2$  property, coupled with a large gyromagnetic ratio that allows good sensitivity and their natural 100% abundance. Therefore, from the beginning of NMR development, protons have been the focus of extensive methodological and experimental investigations, and most to the basic theory concerning proton NMR spectroscopy in the solid-state was described as early as in the 60's, for example coherent averaging principles for high-resolution spectroscopy in solids<sup>27-29</sup>, or later dynamics of proton spin diffusion<sup>30, 31</sup>.

However, research in high-resolution solid-state NMR of protons has been limited by demanding hardware requirements, thus leading to slow progress and application of proton solid-state methodology in the past decades. Whereas spins  $I=1/2$  benefit from an intrinsic high-resolution in solution NMR spectroscopy due to molecular tumbling which averages the different anisotropic interactions, namely chemical shifts and nuclear dipole-dipole couplings<sup>32</sup>. In the solid-state, those interactions are naturally fully observable. Their magnitude depends, for a given

crystallite, on its orientation with respect to the external magnetic field, which leads for powdered samples to observation of very broad overlapping spectral lines<sup>33</sup>. For the protons, dipolar couplings among the dense proton network, which have a magnitude of tens of kilohertz, typically limit NMR resolution and cover the chemical information carried by chemical shielding.

In order to improve the resolution in solid-state NMR, the sample is usually rotated at the so-called magic angle, i.e. around an axis directed along  $\theta=54.7^\circ$  with respect to the external magnetic field<sup>34, 35</sup>. This rotation averages the anisotropic interactions described by second-rank spatial tensors, notably the chemical shift and dipolar couplings, provided the spinning frequency is fast enough compared to the magnitude of the averaged interactions.

Magic-Angle Spinning (MAS) offers high-resolution for observation of most nuclei at low natural abundance in solid-state powders. Thus solid-state NMR has become a major spectroscopic tool in various areas of chemistry and materials science<sup>10, 19</sup>. However, NMR acquisition of high-resolution proton spectra in solids is particularly challenging. Indeed, magic-angle spinning alone cannot provide sufficient averaging of the strong proton-proton dipolar interactions in the solid-state due to strong dipolar couplings and their abundant spins and thus further averaging methods must be combined with MAS in order to obtain narrow spectral lines.

### **A.1.2. NMR Line Shapes**

The principal barrier to the widespread use of proton NMR experiments in powdered solids is resolution. Indeed, even if the natural abundance of protons is

very high and can be, with high sensitivity, a ubiquitous probe for the characterization of structure and dynamics in organic materials, this NMR spectroscopy requires, as a counterpart, handling of the strong dipolar couplings that affect dense proton networks.

In the liquid-state, the isotropic averaging of the dipolar couplings is done by molecular tumbling, which allows straightforward acquisition of very high-resolution proton spectra as seen in figure A.1a. Unlike this case, when we use static solid NMR spectroscopy, the proton spectrum reveals the presence of large dipolar broadening that fully obstructs spectral resolution as illustrated in figure A.1b. The magnitude of this broadening typically reaches a few tens of kilohertz, in the case of rigid non-deuterated powdered solids. Magic-angle spinning alone does not average completely the strong dipolar couplings present among the proton network and does not yield very high-resolution proton spectra, even when using the highest accessible spinning frequencies<sup>36</sup> (figure A.1c).

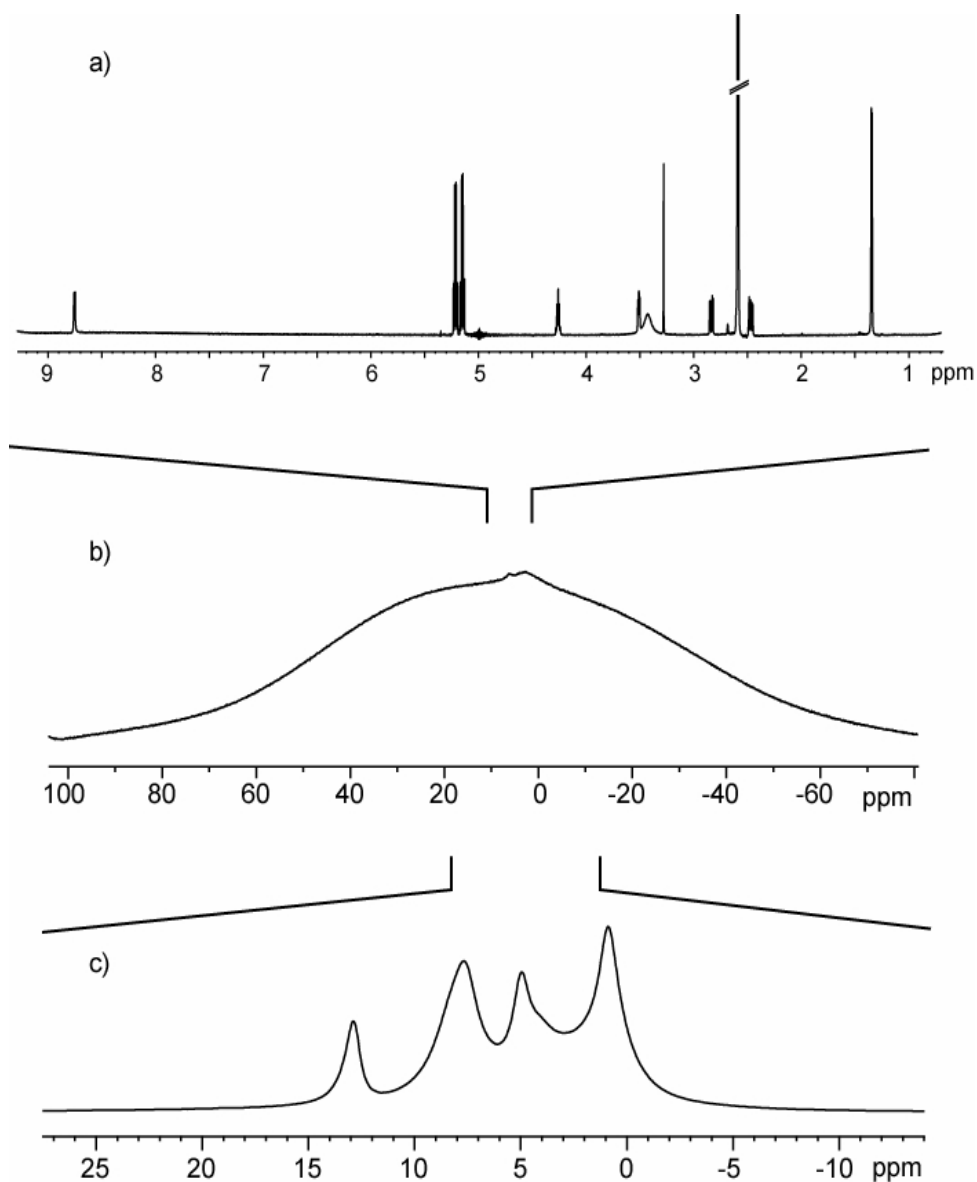


**Figure A.1.**  $^1\text{H}$  spectra of (**1**) recorded (a) in solution in DMSO- $d_6$ , (b-c) in the solid state for a crystalline powder (b) in static conditions and (c) under magic-angle spinning at  $\omega_R=30\text{kHz}$ .

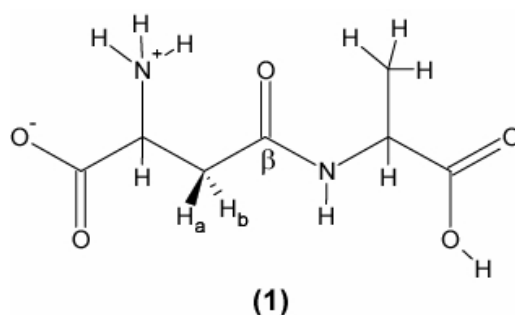


**Figure A.2.** Chemical formula of dipeptide  $\beta$ -L-Aspartyl-L-Alanine (1)

Therefore, a deeper insight into proton spin dynamics and dipolar Hamiltonian, and development of coherent averaging methods in combination with MAS, is necessary to achieve high-resolution proton spectroscopy of powdered solids.

The high field truncated dipolar Hamiltonian<sup>33, 37</sup> is defined for a pair of spins with

$$H_D = \frac{1}{2} \frac{\mu_0 \hbar \gamma_1 \gamma_2}{4\pi r^3} (1 - 3 \cos^2 \theta) (3I_{1z} I_{2z} - I_1 \cdot I_2)$$

where  $r$  stands for the internuclear distance between spins 1 and 2, and  $\theta$  is the angle between the internuclear vector and the external field ( $z$ -axis). This equation defines the homonuclear dipolar Hamiltonian.  $H_D$  typically corresponds to terms of magnitude tens of kHz. Its dependence on  $r$  and  $\theta$  shows that dipolar couplings can provide information about molecular structure and dynamics. However, the complexity of corresponding NMR spectrum increases exponentially with the size of the considered spin system.

Magic angle spinning generates a time dependence of the spin Hamiltonian, and performs averaging of the spatial part of the dipolar and chemical shift interactions<sup>33, 38</sup>. However, reaching a pure isotropic average Hamiltonian (e.g. for a dipolar coupling  $\overline{H_D^{(0)}} = 0$ ) is feasible, in the general case, only if the spinning frequency can be significantly greater than the size of the averaged interaction. Concerning proton homonuclear dipolar couplings, this condition is not fulfilled when

studying rigid solids, with no isotopic dilution. Therefore, decoupling methods that additionally make use of radio-frequency (rf) irradiation have been developed for averaging this homonuclear dipolar interactions.

Most of these methods have been designed and analysed within the context of so-called Average Hamiltonian Theory (AHT), which stands as the standard analytical framework for the concept of coherent averaging<sup>28, 33, 37, 39</sup>. By creating a coherent perturbation (for example by applying a time-dependent rf irradiation), it is possible to control the evolution of the spin system, which then effectively behaves as if driven by a time-independent average Hamiltonian  $\overline{H}$ . This effective Hamiltonian can be described with the Magnus expansion:

$$\overline{H} = \overline{H}^{(0)} + \overline{H}^{(1)} + \overline{H}^{(2)} + \dots$$

with a zero-order average Hamiltonian defined as:

$$\overline{H}^{(0)} = \frac{1}{t} \int_0^t H(t') dt'$$

This average Hamiltonian  $\overline{H}^{(0)}$  can describe the evolution of the system accurately if  $\overline{H}$  converges rapidly.

In order to average properly both dipolar interactions and chemical shift anisotropies, it is worth combining the effects of magic-angle spinning with coherent averaging in the spin space using multiple-pulse rf irradiation of the spins. This technique is known as CRAMPS (Combined Rotation and Multiple Pulse Spectroscopy)<sup>40, 41</sup>, and constitutes the foundation of high-resolution spectroscopy of protons in the solid-state.

In practice, many efficient homonuclear decoupling sequences developed in the last decade<sup>27, 42-55</sup>, like FSLG and variants<sup>46, 47, 49, 52</sup> or DUMBO<sup>54, 55</sup>, were

designed as continuous radio-frequency irradiation, and therefore are implemented in an indirect dimension of acquisition of a two-dimensional experiment. FSLG<sup>46, 47, 49</sup> is a very commonly used technique for proton line-narrowing in solids, in which the continuous rf irradiation frequency is periodically switched between the two Lee-Goldburg conditions  $\pm \nu_1 / \sqrt{2}$ . Identical line-narrowing conditions can be provided by replacing the frequency switch by an equivalent phase modulation, as implemented in the PMLG scheme<sup>52, 56</sup>. The 2D pulse sequence for indirect acquisition of high-resolution proton spectra is presented in figure A.3a<sup>52, 55</sup>. As an illustration of the resolution achieved using optimized eDUMBO decoupling conditions, a corresponding 2D spectrum recorded at 500 MHz (proton resonance frequency), for a crystalline powder of dipeptide  $\beta$ -L-Aspartyl-L-Alanine (**1**), is shown in figure A.3b.

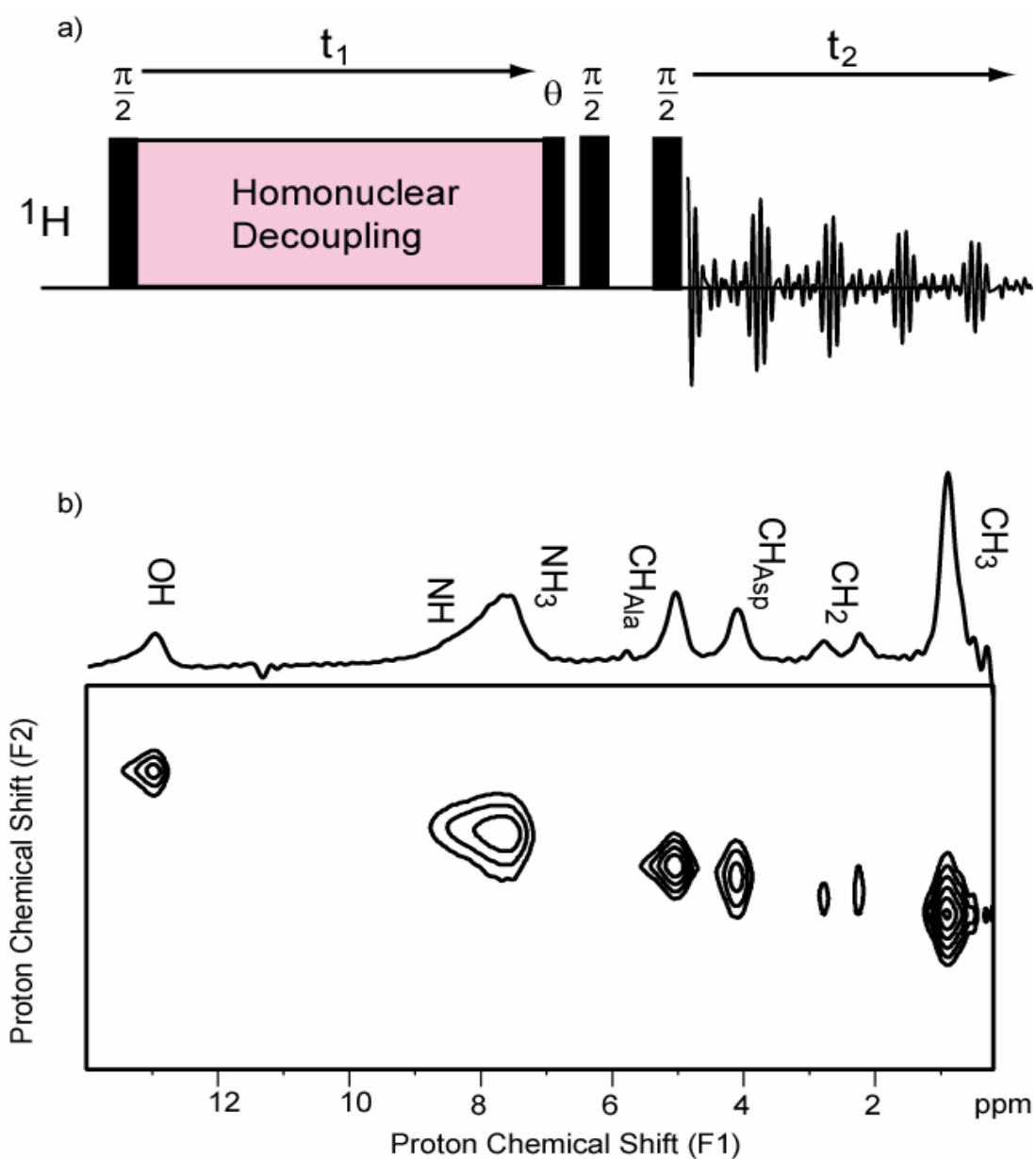


**Figure A.3.** (a) 2D Pulse sequence for indirect detection of high-resolution proton spectra, and (b) corresponding spectrum of dipeptide  $\beta$ -L-Aspartyl-L-Alanine (**1**) recorded at 12.5 kHz MAS and 100 kHz eDUMBO decoupling.

In the following section, we will provide more insight into proton homonuclear decoupling techniques, and more specifically about the DUMBO continuous phase modulated irradiation scheme that was developed in our laboratory<sup>55</sup>.

### A.1.3. Homonuclear Dipolar Decoupling

Various types of radio-frequency (rf) irradiation schemes have been developed in the past to average out the spin part of proton dipolar interactions, and are usually applied in addition to magic-angle spinning for acquisition of high-resolution proton spectra in solid-state NMR. In such combined rotation and multiple-pulse techniques (CRAMPS)<sup>40, 41</sup>, proton resolution is mainly determined by the quality of the applied homonuclear dipolar decoupling sequence.

As seen previously, pioneering ideas behind proton dipolar decoupling were introduced in the very early stages of NMR development, by Lee and Goldburg<sup>42</sup>, and Waugh and co-workers<sup>27</sup>. By means of rf irradiation, they designed a rotation in the spin space that mimics the isotropic movement that is produced by rotating the sample at the magic-angle, and which averages the spatial part of the dipolar Hamiltonian<sup>33</sup>. Following these ideas, different homonuclear averaging strategies have then been proposed in order to improve proton resolution in solids<sup>43-46, 48-53</sup>. In particular, their main objective was to reduce sensitivity to experimental imperfections and rf inhomogeneity. Among these various approaches, Vega and co-workers proposed in the late 90's the so-called PMLG<sup>52, 54</sup> rf irradiation schemes, that constitute the continuous phase-modulated equivalents to the standard Frequency-Switched Lee-Goldburg (FSLG) homonuclear decoupling sequences<sup>49</sup>. The main advantage of continuous phase modulated irradiation schemes is that they can provide a better quality of homonuclear decoupling and a subsequent increase in the observed proton spectral resolution. Note that continuous advances in proton homonuclear dipolar decoupling have been driven by a few common needs: not only

an improvement of the proton resolution in solids is important but also the design of proton homonuclear decoupling sequences that are easy to use efficiently on the spectrometer and that work at high magic-angle spinning frequencies is targeted.

During their Ph.D. work in our group, Dimitris Sakellariou and Benedicte Elena developed a continuous phase modulated approach to decoupling, the so called DUMBO sequence<sup>55</sup>. The first attempts involved numerically optimised sequences using a computer model spin system under static conditions which led to the DUMBO-1 sequences. This sequence was shown to give very good experimental performance for high resolution proton observation under reasonably fast magic angle spinning (up to 25 kHz)<sup>56</sup>. The DUMBO homonuclear decoupling scheme consists of a continuous phase modulated radio-frequency irradiation:

$$H_{rf}(t) = \omega_1 [I_x \cos \phi(t) + I_y \sin \phi(t)]$$

with a rf amplitude  $\omega_1$  and a periodic time-dependant phase function  $\phi(t)$  defined as a Fourier series<sup>55</sup>.

It is also possible using DUMBO-1 decoupling to acquire one dimensional proton high-resolution spectra by introducing 5  $\mu$ s windows for detection, every three cycles of DUMBO-1 decoupling. The corresponding pulse sequence is depicted in figure A.4a. The observed resolution is such that all resonances can be fully resolved and assigned from a one-dimensional spectrum of a small organic molecule, and this spectrum is directly comparable to the corresponding data from solution NMR as compared in figures A.4b and A.4c.

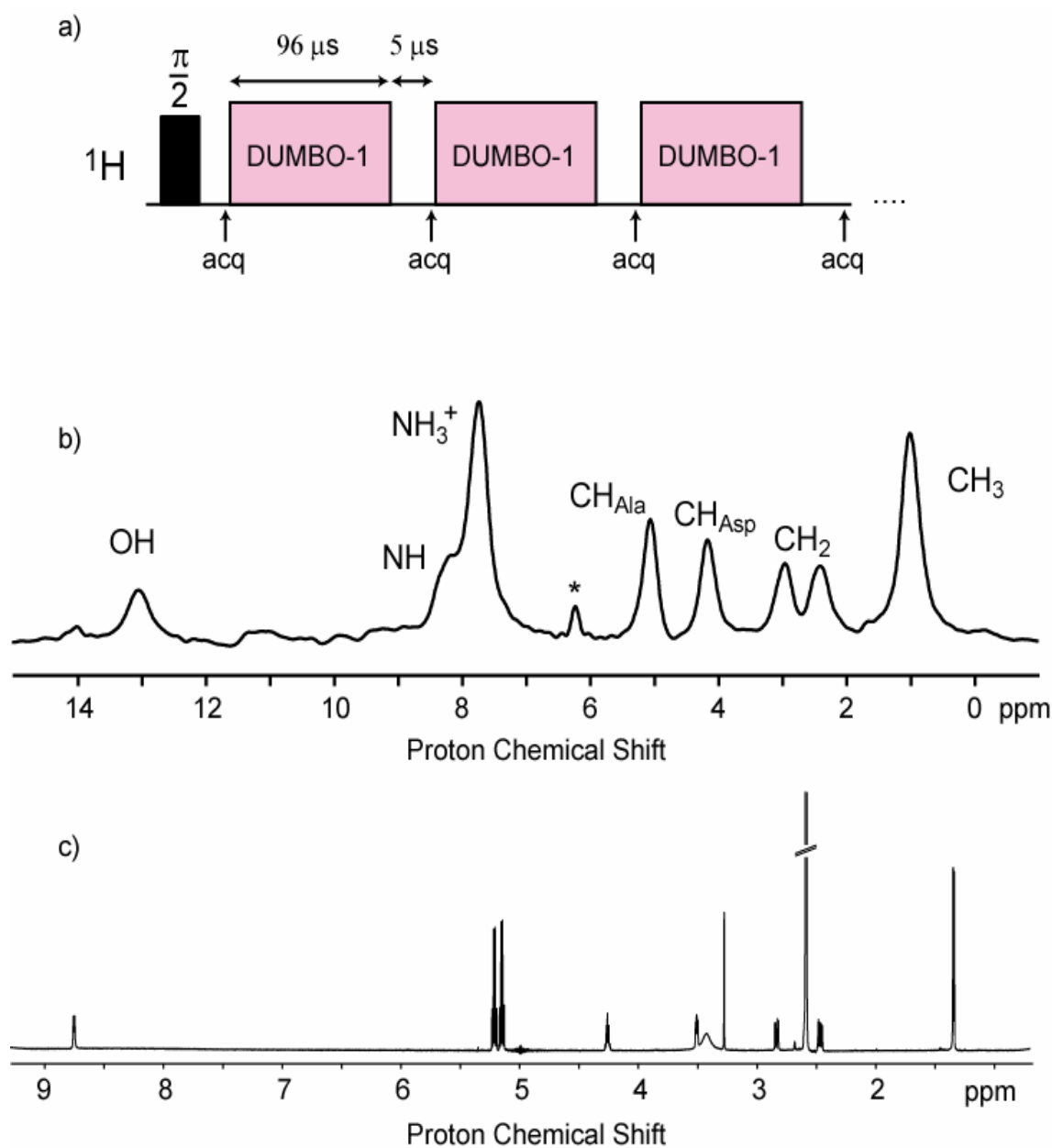


**Figure A.4.** (a) Pulse sequence for acquisition of 1D high-resolution  $^1\text{H}$  spectra. Short windows are left for acquisition every 3 cycles of the DUMBO-1 sequence. (b) Corresponding  $^1\text{D}$  spectrum for (**1**) recorded at a proton resonance frequency of 700 MHz at 12.5 kHz MAS (c) Spectrum of (**1**) recorded at a proton resonance frequency of 700 MHz in solution in DMSO- $d_6$ . This spectrum is not shown to compare the assignment but to show that we can see all the individual lines of the proton in the solid-state NMR.

Moreover, the “eDUMBO” direct experimental optimisation procedure originally developed for improving broadband heteronuclear decoupling in solid-state NMR can be transferred to the proton homonuclear dipolar decoupling case. The best performing continuous phase modulated scheme, dubbed eDUMBO-1<sub>22</sub>, designed with this method leads to a significant resolution enhancement on proton NMR experiments in the solid-state<sup>57</sup>. These optimised sequences seem also to work at different spinning speeds, as long as direct interference effects are avoided between  $\nu_1$  and  $\nu_r$ . To evaluate proton resolution under continuous phase modulated decoupling, simple two-dimensional <sup>1</sup>H-<sup>1</sup>H experiments under MAS, with homonuclear decoupling during  $t_1$  evolution and MAS only in  $t_2$ <sup>52, 56</sup> were acquired. A comparison of the performances for the two optimised sequences eDUMBO-1<sub>22</sub> and eDUMBO-1<sub>12.5</sub> with the original DUMBO-1 scheme is presented in table A.1. After correction with the scaling factor, the resolution is shown to reach less than 0.2 ppm when working at 700 MHz proton Larmor frequency<sup>57</sup>.

@ 500 MHz			
a)			
12.5 kHz MAS:	$\Delta^*(\text{CH}_3)$	$\lambda_{\text{exp}}$	$\Delta^{\text{cor}}(\text{CH}_3)$
DUMBO-1	72 Hz	0.48	152 Hz (0.30 ppm)
eDUMBO-1 <sub>12.5</sub>	72 Hz	0.54	133 Hz (0.27 ppm)
eDUMBO-1 <sub>22</sub>	72 Hz	<b>0.56</b>	<b>128 Hz (0.26 ppm)</b>
b)			
22 kHz MAS:	$\Delta^*(\text{CH}_3)$	$\lambda_{\text{exp}}$	$\Delta^{\text{cor}}(\text{CH}_3)$
DUMBO-1	82 Hz	0.48	171 Hz (0.34 ppm)
eDUMBO-1 <sub>12.5</sub>	88 Hz	0.55	161 Hz (0.32 ppm)
eDUMBO-1 <sub>22</sub>	80 Hz	<b>0.57</b>	<b>141 Hz (0.28 ppm)</b>
@ 700 MHz			
c)			
12.5 kHz MAS:	$\Delta^*(\text{CH}_3)$	$\lambda_{\text{exp}}$	$\Delta^{\text{cor}}(\text{CH}_3)$
DUMBO-1	76 Hz	0.475	160 Hz (0.23 ppm)
eDUMBO-1 <sub>12.5</sub>	80 Hz	0.55	150 Hz (0.21 ppm)
eDUMBO-1 <sub>22</sub>	78 Hz	<b>0.575</b>	<b>135 Hz (0.19 ppm)</b>

**Table A.1.** Experimental measured linewidth for  $\beta$ -L-Aspartyl-L-Alanine, decoupling scaling factors, and corresponding corrected linewidth ( $\Delta^{\text{cor}} = \Delta^* / \lambda_{\text{exp}}$ ) in Hz or ppm, observed at (a-b) 500 MHz  $^1\text{H}$  resonance frequency respectively at (a) 12.5 kHz and (b) 22 kHz MAS frequencies, and at (c) 700 MHz and 12.5 kHz MAS frequency<sup>57</sup>.

#### A.1.4. Conclusion

Proton spectra clearly provide a much more sensitive source of NMR spectra for compounds at natural abundance. Recently, substantial progress has been made in the development of homonuclear dipolar decoupling sequences that allow the acquisition of high-resolution proton NMR spectra in rigid solids<sup>56-59</sup>. These sequences have then allowed the development of multi-dimensional correlation methods for both homonuclear proton-proton spectroscopy<sup>60, 61</sup> and heteronuclear proton-carbon INEPT based HSQC type correlations<sup>62</sup>.

This increase in resolution and lifetimes of coherences allows new applications of high resolution proton NMR spectroscopy in the solid-state, through the development and analysis of both homonuclear or heteronuclear correlation methods. Different examples of such experiments will be presented in the following parts.

## **A.2. Assigning Powders to Crystal Structures**

### **A.2.1. Introduction**

Structural characterisation of solids plays an increasingly key role in organic chemistry in general, and in pharmaceutical chemistry in particular. Even though reference structures from single crystal diffraction studies are commonly available, nevertheless when the sample is in powder form characterisation becomes exceedingly difficult. Powder forms are increasingly important, especially in relation to detailed and reliable characterisation of pharmaceutical formulations for example<sup>63-66</sup>.

One solution would be to use powder X-ray diffraction and a large number of papers have been published on the determination of crystal structure using this method. Indeed, much progress has been made and mainly concerning advances in ab initio methods such as the integration of intensities<sup>67, 68</sup>, the phase-annealing procedure<sup>69</sup> and the Montecarlo method<sup>70</sup>. However, there are still some major problems which limit the crystal structure determination procedure. And the main limiting factor remains the limits in the measurement of intensity<sup>71</sup>.

Our approach to determining powder forms is to assign the NMR spectrum of the powder to a possible known reference crystal structure<sup>72</sup>. This approach has recently been shown to be viable through the use of carbon-13 cross polarisation magic angle spinning spectra of powders, in combination with first principles calculation<sup>66, 72-80</sup>. This approach seems highly promising. The major handicap in this approach, however is that the carbon-13 spectrum needs to be unambiguously assigned (at least for the large majority of signals) before the resonance frequencies can be compared to those expected for different crystalline forms in order to determine which form is present. If the compounds are enriched in carbon-13, assignment is straightforward, but at natural isotopic abundance assignment becomes a challenge. It was recently demonstrated that INADEQUATE spectra could be used at natural abundance to assign carbon-13 spectra, and examples have been shown for several medium sized molecular systems (for example, testosterone, cholesteryl acetate, brucine, simvastatin, vitamin D, oxybuprocaine hydrochloride)<sup>73, 80-82</sup>. However, most of these compounds required acquisition time of a few days for the INADEQUATE spectra.

In this section we will demonstrate how both proton and carbon spectra can be assigned using homonuclear proton double-quantum spectra in combination with proton-carbon HSQC spectra. We then show that the proton chemical shifts can be included in the process of assigning the spectra to a crystal structure using first principles calculations. The method is demonstrated with the example of the K salt of penicillin G (**2**) (Figure A.5), a model compound which has already been studied by solid-state NMR<sup>83</sup>.

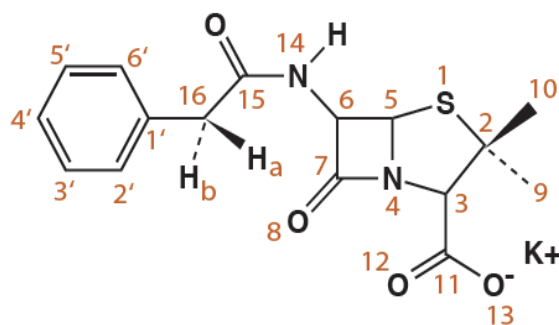


**Figure A.5.** Chemical formula of penicillin G K salt.

The one-dimensional carbon-13 CPMAS spectrum of (**2**) is shown in figure A.6. It clearly shows seven well resolved peaks between 20 and 80 ppm for the seven aliphatic carbons, three peaks for the three carbonyl groups at around 175 ppm, and three peaks for the aromatic region around 135 ppm. However, a more detailed assignment is not possible at this stage.

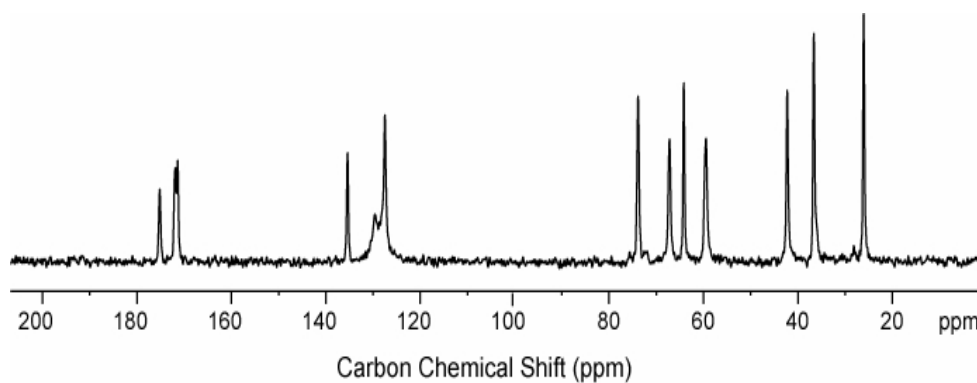


**Figure A.6.** One-dimensional 125 MHz carbon-13 CPMAS spectrum of the K salt of penicillin G (**2**). The spectrum was obtained with 2048 scans (105 min. total acquisition time), at a spinning speed of 30 kHz, and a CP contact time of 1.4 ms, with temperature regulated at 293K.

## A.2.2. Proton Correlation Spectroscopy – DQ CRAMPS

### A.2.2.1 Introduction

Despite the handicaps discussed above the study of proton-proton contacts in the solid-state has nonetheless been shown to be particularly valuable, when possible, and such proton-proton NMR constraints are increasingly exploited for characterization of isotopically enriched molecular systems<sup>22, 23, 84, 85</sup>, mostly micro-crystalline proteins, using isotopic dilution and indirect detection schemes. Spiess and coworkers have shown that double-quantum (DQ) proton NMR spectra, obtained under fast MAS, can have very important applications in non-biological systems<sup>19</sup>.

Thus, two-dimensional  $^1\text{H}$ - $^1\text{H}$  double-quantum (DQ) magic-angle spinning (MAS) experiments have become a method of choice to probe proton-proton proximities and have provided much insight into the solid-state structures adopted by various materials<sup>19</sup>. However, as seen before, the strong proton-proton dipolar couplings usually obscure detailed chemical shift information. And for organic solids containing networks of many dipolar-coupled protons, the resolution of multiple-quantum  $^1\text{H}$  solid-state NMR is the limiting factor. But it has been shown that employing fast MAS alone (typically 30 kHz) yields, in many cases, sufficient resolution to resolve specific DQ peaks. The proton-proton proximities identified in this way have allowed, for example, the identification of intermolecular hydrogen-bonds or  $\pi$ - $\pi$  packing arrangements in a variety of organic materials<sup>86, 87</sup>. However, using only MAS is often insufficient to achieve resolution in the crowded regions of  $^1\text{H}$

DQ MAS spectra. One solution to enhance resolution of  $^1\text{H}$  spectra is to combine the rotation of the sample with the application of carefully synchronized multiple-pulse sequences in the so-called CRAMPS approach<sup>26, 40, 41, 56, 88</sup> as seen previously.

Along these lines, Schnell and co-workers<sup>89</sup>, and more recently Vega and co-workers<sup>60</sup> have reported, by employing windowless and windowed homonuclear decoupling in the indirect ( $t_1$ ) and direct ( $t_2$ ) dimensions respectively, an improvement in resolution of proton DQ spectra. However, a major problem in such spectra was so far the presence of artefacts as compared to the fast MAS approach.

To avoid this, Brown et al.<sup>61</sup> showed how double-quantum (DQ) excitation and reconversion can be achieved using the POST-C7 pulse sequence<sup>90</sup>. POST-C7 was chosen because of its inherent offset compensation and its  $\gamma$ -encoding property. This latter gives an enhanced overall sensitivity and yields DQ spectra free of rotor-encoded spinning sidebands<sup>91</sup>.

POST-C7 is a DQ recoupling pulse sequence with a phase dependence on the rotor phase. This is to be compared with BABA<sup>92</sup> which has an amplitude dependence on the rotor phase. Thus, the rotor-encoded DQ set of spinning-sidebands<sup>19, 93, 94</sup> observed in DQ MAS spectra recorded with BABA recoupling and with  $\Delta t_1 \neq \tau_R$  is not observed with POST-C7; instead, all the intensity is concentrated on the first sideband at  $\nu_{DQ} - \nu_R$ <sup>91</sup>. As no synchronization is required between the MAS and the  $t_1$  increment (which has to correspond to an integral number of decoupling cycles), interference conditions between the MAS and the homonuclear decoupling scheme can easily be avoided.

The pulse sequence for the  $^1\text{H}$  DQ CRAMPS experiment employed in this work is shown in figure A.7. Two phase-modulated homonuclear decoupling

schemes, carefully designed to provide optimal proton resolution in strongly coupled systems, the windowless eDUMBO-1<sub>22</sub><sup>57</sup> and windowed-DUMBO-1<sup>56</sup>, were applied in the  $t_1$  and  $t_2$  dimensions, respectively. The length and the phases of the pre-pulses  $\theta_1$  were carefully calibrated to minimize axial peaks and quadrature images in  $F_1$ . In the same way, the orientation of the effective field of the DUMBO-1 sequence was adjusted to suppress zero frequency peaks in  $F_2$ . In addition pre-pulses  $\theta_2$  were inserted before and after each detection window to minimize quadrature images in the direct dimension. For both eDUMBO-1<sub>22</sub> (during  $t_1$ ) and w-DUMBO-1 (during  $t_2$ ) homonuclear decoupling, a single cycle was constructed from 64 steps of 500 ns each, yielding a total cycle duration of 32  $\mu$ s.

As noted above, the phase dependence on the rotor phase of the POST-C7 sequence means that there is a frequency shift of all peaks by  $\nu_R$  from the centerband position. Since the  $F_1$  spectral width is smaller than  $\nu_R$ , the DQ peaks are folded in from their  $\nu_R$ -shifted frequencies. Sign discrimination in  $F_1$  is achieved by incrementing the DQ excitation block according to the States-TPPI protocol. A 8-step phase cycle selected  $\Delta p = \pm 2$  for the POST-C7 DQ reconversion block (4 steps) and  $\Delta p = \pm 1$  for the  $90^\circ$  pulse of the z-filter (2 steps).

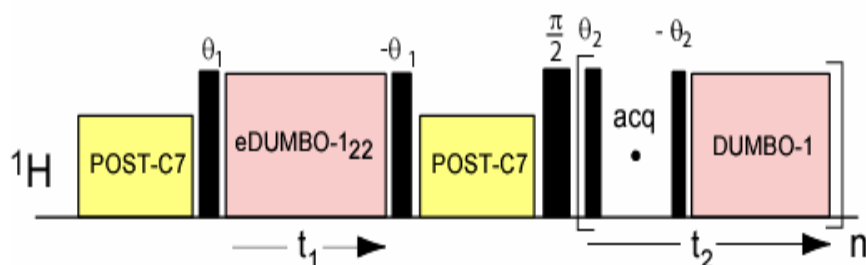


**Figure A.7.** Pulse sequence for the  $^1\text{H}$  DQ CRAMPS experiment

### A.2.2.2. Experimental Results

Using the previously described sequence (figure A.7)<sup>95</sup>, the two-dimensional  $^1\text{H}$ - $^1\text{H}$  DQ-CRAMPS spectrum of (**2**) is shown in figure A.8. Homonuclear dipolar decoupling was achieved using the experimentally optimised eDUMBO-1<sub>22</sub> sequence with an rf decoupling field of 100 kHz nutation frequency and a 12.5 kHz magic angle spinning frequency on a 2.5mm probe. Heteronuclear decoupling was achieved using a SPINAL-64 scheme. The DQ-CRAMPS spectrum was acquired with 32 scans for each of 340 increments in  $t_1$ , and a repetition delay of 2 seconds, leading to a total experimental time of 6 hours. C7 was implemented with a  $^1\text{H}$  rf field amplitude of 87.5 kHz, using 3 post C7 basic elements cycles, for a total excitation or reconversion time of 68.5  $\mu\text{s}$ .

It is clear from this spectrum that while the one-dimensional CRAMPS proton spectrum (shown above the DQ spectrum) is only partially resolved, the intrinsic resolution of the spectrum is very good (about 0.2 ppm) and allows the identification of about 16 correlations that allow the assignment of all the proton chemical shifts. The DQ-CRAMPS pulse sequence provides correlations between protons due to through-space dipolar couplings. The assignment procedure is carried out by considering the crystal structure of the molecule and determining the expected correlations in the spectrum in terms of short range distances between pairs of protons obtained by either intra- or intermolecular contacts. In the figure red lines indicate correlations consistent with short-range intra-molecular contacts ( $<2.75\text{\AA}$ ), blue lines indicate short-range intermolecular contacts ( $<2.75\text{\AA}$ ), and green lines indicate expected intra- or inter-molecular longer-range contacts ( $>2.75\text{\AA}$ ). In this way

a coherent assignment of all the protons is achieved in combination with the study of the proposed crystal structure (which in this example case is not in doubt). We note that only the aromatic protons (resonating around 7 ppm) cannot be individualised. The two diastereotopic protons of the CH<sub>2</sub> group (resonating at 3.9 and 4.7 ppm) can in principle be specifically assigned, since we can see a correlation between the resonance at 3.9 ppm and the protons of the CH<sub>3</sub> group which are in the same plane (16b with 9). However, we note that there is some doubt present for these two protons.

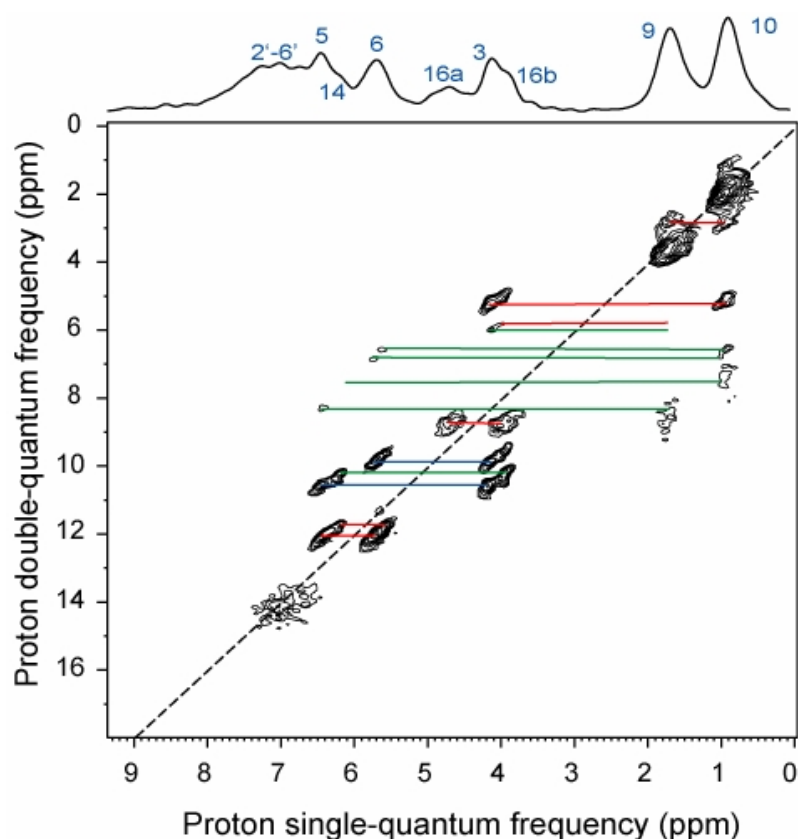


**Figure A.8.** Contour plot of the two-dimensional <sup>1</sup>H-<sup>1</sup>H DQ-CRAMPS spectrum of (2). The observed correlations are indicated with red lines for intra-molecular near 150 neighbour correlations (<2.75 Å), blue lines indicate inter-molecular near neighbour contacts (<2.75 Å), and green lines indicate intra- and intermolecular longer range correlations, as described in the text. The one-dimensional CRAMPS spectrum is shown above, together with the determining assignment.

## A.2.3. Through-Bond Spectroscopy – INEPT

### A.2.3.1. Introduction

Due to the lack of resolution available for direct proton spectroscopy, NMR of solids has mainly developed through the study of low abundance nuclei, for example mainly carbon-13 or nitrogen-15 for organic molecules. Nevertheless, observation of those rare nuclei cannot be conducted ignoring the presence of the dense network, which does still control, in many cases, the behavior of the whole spin system. Therefore, most NMR experiments performed on heteronuclei include, at least, two crucial steps that directly involve protons: polarization transfer, and heteronuclear dipolar decoupling.

With the developments of cross-polarization and magic angle spinning, as well as multi-dimensional correlation methods via through-space dipolar interactions, solid-state NMR of carbon-13 can be handle more easily than proton solid NMR. Moreover, as heteronuclear scalar couplings are extremely reliable probes of direct proximities, such kind of experiments can be used to assign and characterize powdered rigid solids. It has been shown that J couplings can be successfully resolved for powders under MAS, and various techniques that employ heteronuclear J couplings in solids are currently applied for spectral editing<sup>96, 97</sup>, or acquisition of through-bond correlation spectra<sup>98</sup>.

As an illustration of the good resolution available for  $^1\text{H}$ - $^{13}\text{C}$   $^1\text{J}$  couplings for crystalline rigid solids, figure A.9b represents a 1D  $^{13}\text{C}$  CP-MAS spectrum of the

dipeptide  $\beta$ -AspAla (**1**), acquired with proton homonuclear dipolar decoupling (eDUMBO-1<sub>22</sub> decoupling scheme at 150 kHz  $\nu_1$  nutation frequency) and fast magic-angle spinning (30 kHz). Under these conditions, we remark that the characteristic features of the different expected multiplicities, particularly for CH, CH<sub>2</sub>, and CH<sub>3</sub> types of carbon-13 resonances, are properly observed.

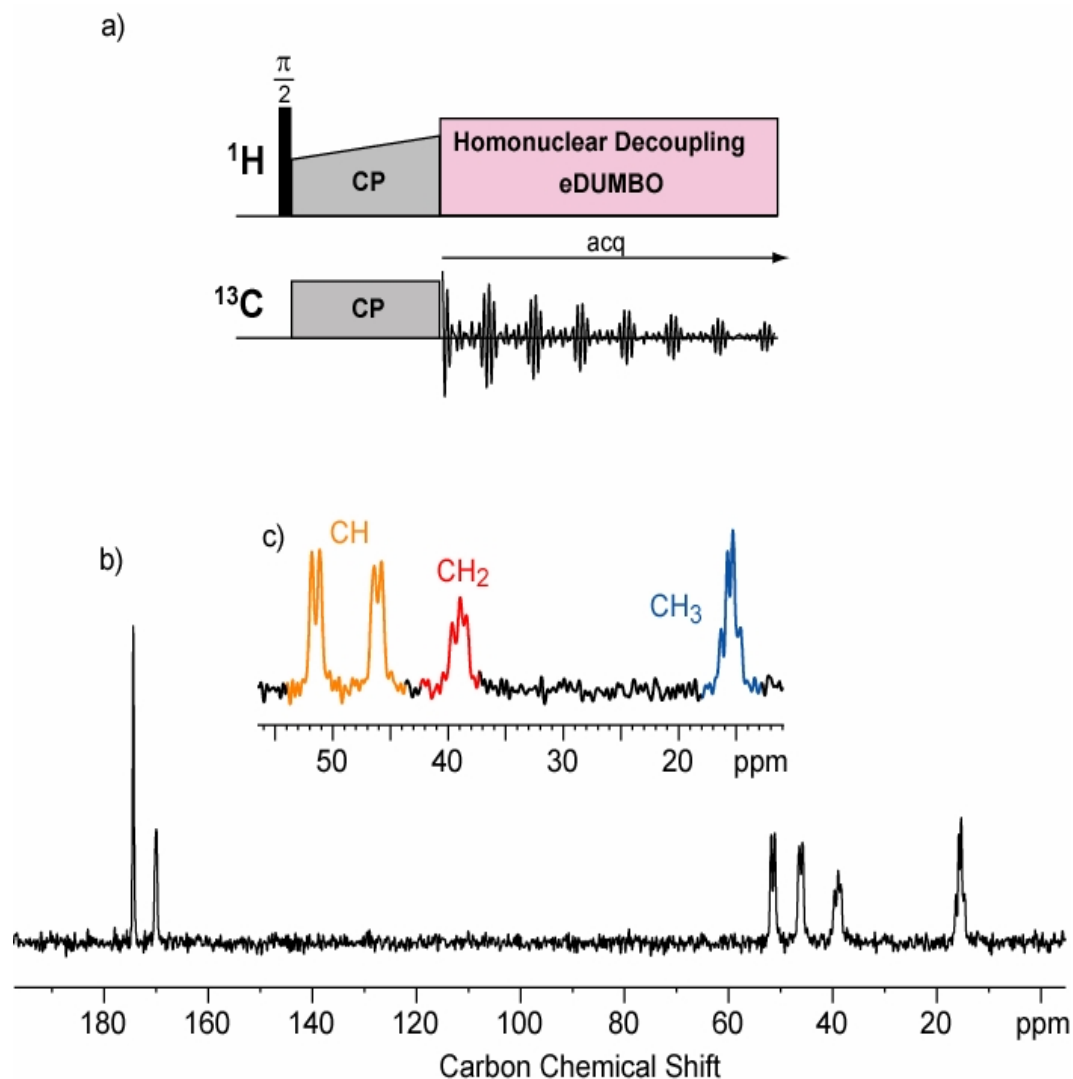


**Figure A.9.** a) Pulse sequence. b) <sup>13</sup>C CP-MAS spectrum of the dipeptide (**1**), acquired under proton homonuclear eDUMBO-1 decoupling with  $\nu_1 = 150$  kHz (20  $\mu$ s decoupling cycle type, i.e 50 steps of 400 ns each), at  $\omega_R = 30$  kHz. c) zoom of region between 0 and 60 ppm.

In solution, the INEPT technique is well known as the method of choice for heteronuclear through-bond polarization transfer<sup>99-101</sup>. A few examples in the literature show applications of INEPT  $^1\text{H}$ - $^{13}\text{C}$  transfer to heterogeneous systems in the case of rather mobile systems, like lipid/water systems<sup>102</sup>, cholesterol embedded in membranes<sup>103, 104</sup>, or mesostructured silica-based particles<sup>105</sup>. However, the fast decay of transverse magnetization coherences thus  $T_2'$  not  $T_2^*$  in crystalline solids has prevented until now any straightforward relevance of the INEPT technique to NMR spectroscopy of rotating powders. Therefore spectral editing techniques and 2D heteronuclear correlation (HETCOR) methods employing J-couplings, such APT<sup>96</sup> or MAS-J-HMQC<sup>98</sup> experiments have so far relied on a first step of cross-polarization, followed by editing or filtering of carbon transverse magnetization via heteronuclear J couplings. One similarity of these sequences is their avoiding of any evolution delay of proton transverse magnetization.

The pulse sequence for the  $^1\text{H}$ - $^{13}\text{C}$  solid-state refocused INEPT experiment introduced recently by Elena et al.<sup>62</sup> is shown in figure A.10. The original liquid-state technique<sup>101</sup> was adapted for rotating solids by adding proton homonuclear decoupling during the  $\tau$  and  $\tau'$  transfer periods, in order to remove proton-proton dipolar couplings. During those delays, fast magic-angle spinning averages chemical shift anisotropy and heteronuclear dipolar couplings, so that only scalar couplings are preserved together with isotropic chemical shifts. The simultaneous  $180^\circ$  pulses on proton and carbon induce refocusing of isotropic chemical shifts after  $2\tau$  and  $2\tau'$ , such that during these delays only  $J_{\text{CH}}$  couplings are controlling coherence transfer and evolution, beside  $J_{\text{CC}}$  couplings in the case of  $^{13}\text{C}$ -labelled compounds. Note that the presence of proton homonuclear decoupling leads to effective scaled  $J_{\text{CH}}$

couplings, the scaling factor close to  $1/\sqrt{3}$  being specific to the employed decoupling scheme.

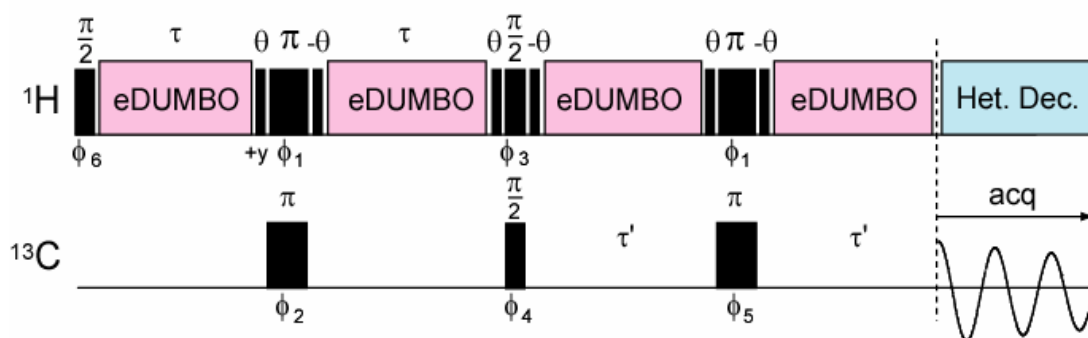


**Figure A.10.** Pulse sequence for the solid-state refocused INEPT experiment.

### A.2.3.2. Experimental Results

Once we have established the assignment of the protons, the carbon-13 resonances can be assigned in a straightforward manner using the through-bond INEPT-HSQC experiment of figure A.10. As seen previously, this experiment has the great advantage, for assignment purposes, that it relies on scalar couplings to obtain correlation between bonded C-H pairs, and contains no through-space correlations that can be source of confusion.

The two-dimensional  $^1\text{H}$ - $^{13}\text{C}$  HSQC spectrum of **(2)** is shown in figure A.11. This spectrum allows the direct identification and assignment of the non-protonated quaternary carbons  $\text{C}_2$  and  $\text{C}_{1'}$ . From the assignment of the proton chemical shifts above, we also directly obtain the complete  $^{13}\text{C}$  chemical shift assignment of all the aliphatic resonances for the compound at natural abundance. At this stage, the only signals that are not assigned are the unresolved aromatic signals, and the three carbonyl  $^{13}\text{C}$  resonances.

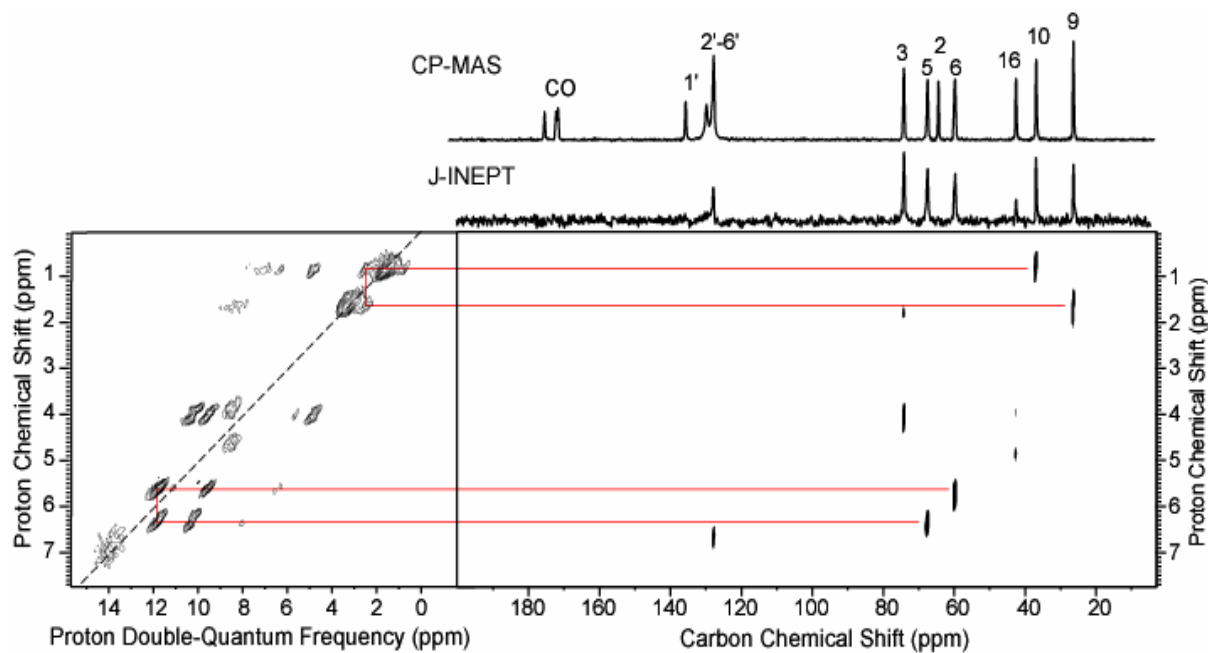


**Figure A.11.** Contour plot of the two-dimensional through-bond INEPT-HSQC spectrum of (2) juxtaposed with the  $^1\text{H}$ - $^1\text{H}$  DQ spectrum. The red lines illustrate the type of sequential connectivity used to finalise the assignments, with the example of the assignment of  $\text{C}_9$  and  $\text{C}_{10}$  through the near neighbour proton contact, and  $\text{C}_5$  and  $\text{C}_6$  similarly.

## A.2.4. Crystal Structures and First Principle Calculations

### A.2.4.1. Introduction

The establishment of links between structural information and NMR parameters is quite a general issue, which has concerned liquid-state as well as solid-state NMR for decades. The widespread tables that have been (empirically) established in liquid-state NMR to correlate the chemical environment of a given atom to its Larmor frequency are a good example of such a link. These tables are extensively used by organic chemists, since they enable the direct identification of chemical functions on the simple basis of the peak positions in a one-dimensional NMR spectrum obtained (in most cases) in a few minutes.

The situation is however more complicated in powdered solids under MAS, where especially long-range range effects and inter-molecular interactions may significantly change the isotropic chemical shifts. As a consequence, methods have been developed to predict the chemical shifts from a given structure, including in particular long-range interactions. Such methods include either semi-empirical, *ab initio* or first principles (meaning density functional theory, DFT) approaches and currently provide quite accurate results in a wide range of systems<sup>73, 106</sup>. Here, we have focused more specifically on *ab initio* and first principle methods, whose fast development in the past ten years have made more and more attractive compared to semi-empirical methods.

Today, the most popular level of theory for calculating NMR chemical shifts is undoubtedly the density functional theory (DFT), which explicitly includes electron correlation effects in the calculations at very low computational cost compared to beyond-CHF methods. This method is therefore extremely attractive, and has been applied to predict the chemical shifts in an incredibly wide range of systems.

The implementation of first principles calculations, using plane waves and pseudo-potentials, in the presence of an external magnetic field has first been addressed by Mauri and co-workers<sup>107</sup>, who developed a theory later adapted to codes based on norm-conserving pseudo-potentials. Few applications of this method were yet proposed because of the limitations inherent to norm-conserving pseudo-potentials, and because it has long been expected that the approaches using pseudo-potentials would not be suitable for the prediction of chemical shifts, as this property requires an accurate description of the wave function at the nucleus.

However, the use of the PAW approach may overcome this problem, as demonstrated by Pickard and Mauri, who implemented a gauge-including PAW formalism (GIPAW) for the accurate calculation of NMR chemical shifts from periodical DFT calculations<sup>108</sup>. They took advantage of the ability to obtain expectation values for the all-electron operators in the PAW approach. In the GIPAW formalism, this field-dependent term ensuring translational invariance is carried out by the operators whose expectation values are to be evaluated, in contrast with the GIAO or IGLO methods (for non-periodical DFT), in which the field-dependant phase is attached to the basis functions and to the occupied electronic orbitals respectively. The advantage of CASTEP is that, contrary to Gaussian which uses only a single molecule, it uses a periodic calculation all around the crystal.

Recently incorporated into the CASTEP program<sup>109</sup>, NMR calculations have been successfully applied to various chemical problems in combination with solid-state NMR studies<sup>74, 77, 78, 110, 111</sup>.

### **A.2.4.2. Results**

The crystal structure for the K salt of penicillin G (**2**) was obtained from the Cambridge Crystallographic Database. The positions of the hydrogen atoms were adjusted in a constrained DFT geometry optimisation using CASTEP<sup>109</sup>. The difference between this code and quantum chemical techniques is that the charge density and wavefunctions are described using a planewave basis set and so the translational symmetry of the system is implicit. The electron-ion interaction of the core electrons is represented by a pseudo-potential, the use of which greatly enhances the computational efficiency of the approach. In all of our calculations the electron correlation effects are modelled using the generalised gradient approximation of Perdew, Burke and Ernzerhof<sup>112</sup>. For the geometry optimisation, we employ “ultrasoft” pseudopotentials<sup>113</sup>, a planewave cut-off energy of 400eV and a 1x1x2 Monkhorst-Pack<sup>114</sup> grid to sample the Brillouin zone. The NMR calculations were performed using the Gauge Including Projector Augmented Wave approach (GIPAW)<sup>108</sup> at the larger cut-off of 440eV, with “ultrasoft” potentials<sup>115</sup>, also using CASTEP<sup>109</sup>. This method allows for a fully solid-state treatment of the system under investigation.

The positions of only the hydrogen atoms were allowed to relax since location of heavy atoms by diffraction methods is significantly more accurate than those for

hydrogens. However, it is well known that, even for nuclear positions determined by neutron diffraction, reported errors in atomic locations significantly influence computed chemical shifts.

To compare directly with experiment, the absolute shielding must be converted to the chemical shift using an appropriate reference shielding. To determine the reference shielding we perform a linear regression against the experimental shifts, imposing a slope of unity.

Once we now have a tentative complete assignment, we are in a position to finalise the assignment to the crystal structure by comparing the measured chemical shifts with those obtained from calculation. Table A.2 contains the values of  $^1\text{H}$  and  $^{13}\text{C}$  chemical shifts from the results of the computation, from the solid-state NMR experiments, and (for comparison) from previous experiments carried out in liquid-state NMR.

Atom number	Computed $^{13}\text{C}$ shift	Experimental $^{13}\text{C}$ shift <sup>a</sup>	Computed $^1\text{H}$ shift	Experimental $^1\text{H}$ shift <sup>b</sup>	Liquid-state $^1\text{H}$ shift <sup>c</sup>
1'	137.9	136.4	-	-	-
2'	130.4	128.7	7.5	7.1 <sup>d</sup>	7.35
3'	129.6	128.7	7.5	7.1 <sup>d</sup>	7.35
4'	132.7	130.6	7.3	7.1 <sup>d</sup>	7.35
5'	130.2	128.7	7.0	7.1 <sup>d</sup>	7.35
6'	132.3	130.6	7.3	7.1 <sup>d</sup>	7.35
2	63.0	65.2	-	-	-
3	78.9	74.9	4.1	4.1	4.21
5	69.0	68.2	6.1	6.4	5.49
6	54.9	60.5	5.3	5.7	5.42
7	175.7	176.1	-	-	-
9	25.7	27.1	2.2	1.7	1.48
10	35.2	37.6	0.5	0.9	1.57
11	168.8	172.9	-	-	-
14	-	-	5.4	6.2	N/a
15	167.2	172.3	-	-	-
16a	38.9	43.3	4.6	4.7	3.68
16b	-	-	4.0	3.9	3.68

**Table A.2.** Comparison of calculated and experimental proton and carbon-13 chemical shifts for (2). All shifts are given in ppm and experimental shifts are referenced to TMS at 293 K. *a)* with an estimated error of  $\pm 0.1$  ppm, mostly due to referencing or slight possible temperature variations. *b)* with an estimated error of  $\pm 0.1$  ppm, the determination of the experimental decoupling scaling factor is an additional potential source of error, and was estimated from comparison with an undecoupled  $^1\text{H}$  30 kHz MAS spectrum. *c)* from Dobson et al.<sup>116</sup>. *d)* the five aromatic protons are not assigned. The error in the measurement here is  $\pm 0.5$  ppm

Figures A.12 and A.13 show the correlation between calculation for the crystal structure and experimentally determined shifts in the solid state for the  $^1\text{H}$  and  $^{13}\text{C}$  chemical shifts. The correlation is found to be remarkable, and confirms our assignment. Additionally, it allows us to assign the three carbonyl groups, since the calculated values are very well reproduced in only one of the six possible alternatives for the assignment, as shown in the figure A.12. The average pairwise rmsd between

the measured and calculated chemical shifts for the carbon-13 resonances is 2.5 ppm.

Figure A.13 shows the comparison between calculation and experiment in the solid state for the  $^1\text{H}$  chemical shifts determined here. Average values were taken for the calculated shifts of the three protons of each  $\text{CH}_3$  group, since at room temperature there will be rapid rotational motion around the  $\text{C}_3$  axes, but the calculation considers only a fully static sample. Again the results are shown to be in remarkable agreement. They clearly allow the confirmation of the assignment of the diastereotopic protons 16a and 16b, which was not entirely sure until this stage, and can clearly be appreciated from the figure where we test the reverse assignment. The calculations also clearly confirm the assignment of the two  $\text{CH}_3$  groups, since even if the exact numerical values are not reproduced correctly by the calculation for these mobile groups, the trend cannot be misinterpreted. The average pairwise rmsd between the measured and calculated chemical shifts for the proton resonances is 0.3 ppm. The difference observed for some protons like the one of the NH group may be explained by the rapid motion of this kind of proton.

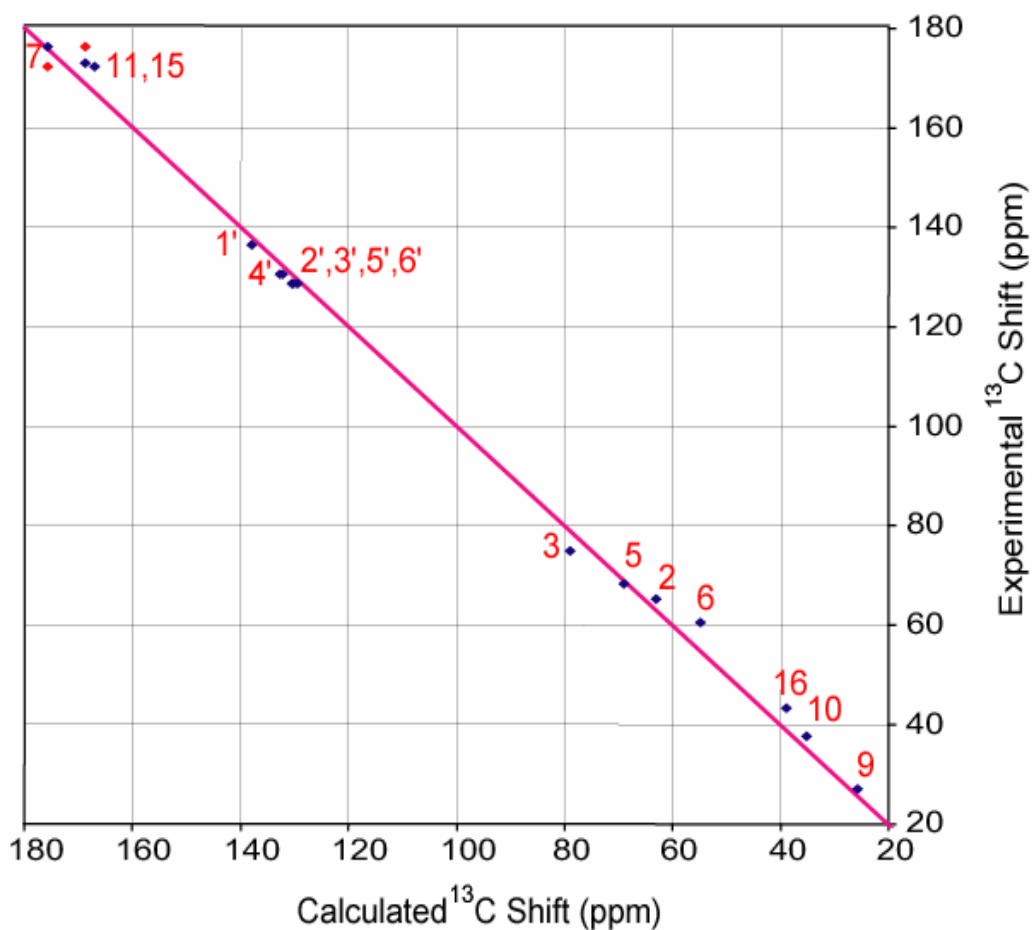


**Figure A.12.** Comparison of measured and calculated values of the chemical shifts of Carbon-13 for (2). proton. The points shown in red test possible alternative assignments for the carbonyl carbons.

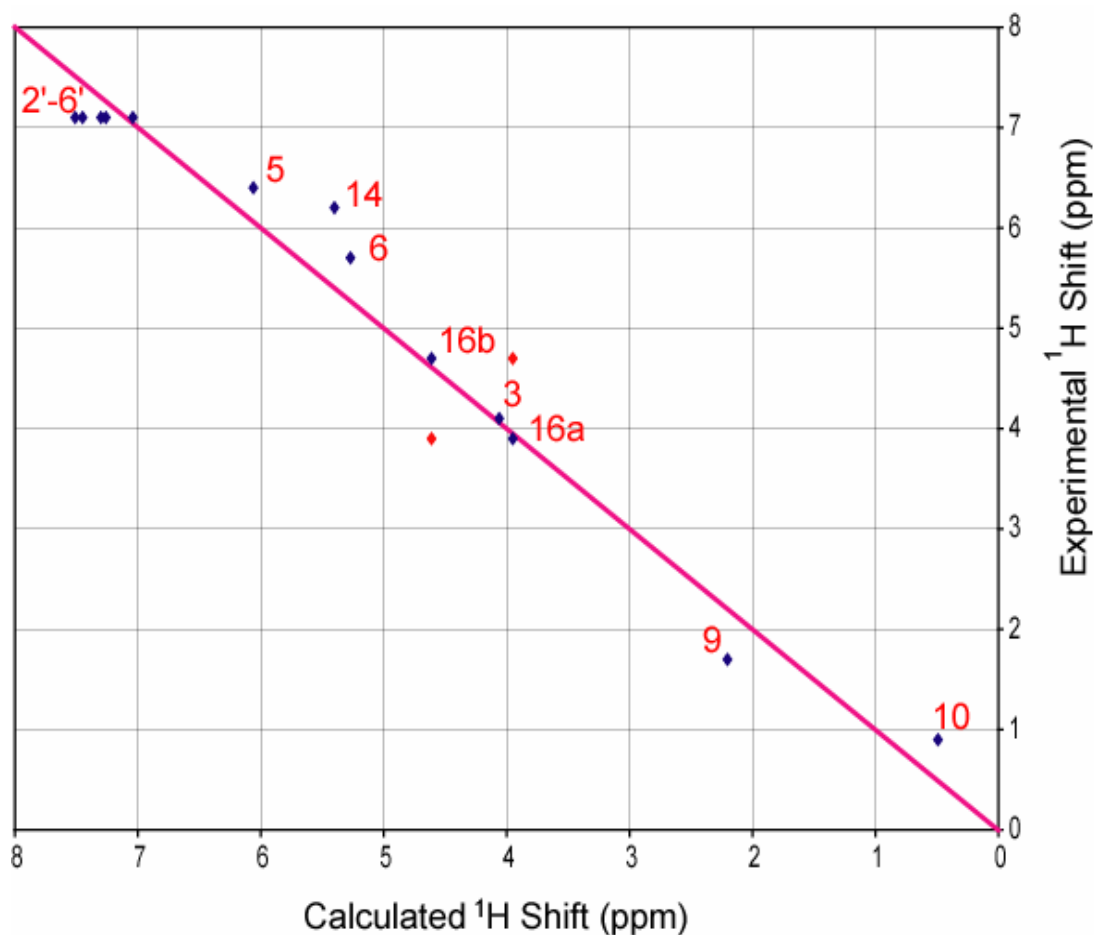


**Figure A.13.** Comparison of measured and calculated values of the chemical shifts of proton for (2). The points shown in red test possible alternative assignments for the  $\text{CH}_2$  protons.

Finally we note that, as mentioned above, the computations are carried out for essentially static atomic positions and therefore do not take account of molecular-level mobility except insofar as it determines the crystal structure. In this case this is particularly likely to induce errors of the calculation of the aromatic chemical shifts, since we can see from the broadening in the carbon-13 spectrum of the aromatic resonances at 130 ppm that the aromatic ring is certainly undergoing some kind of rotational motion. The aromatic proton resonances in this case seem to be systematically slightly overestimated in the calculation, though since they cannot be assigned in the proton spectrum, a more detailed evaluation is not possible.

## A.2.5. Conclusion

Proton chemical shifts have been much less used in computational approaches than carbon-13 (with some notable recent exceptions)<sup>74, 78, 111, 117-120</sup>. Firstly, because they have only very recently become available from experiments and secondly, since the range of chemical shifts is smaller (in ppm), the calculation methods need to be relatively more accurate to provide useful information. Indeed, most previous studies of proton chemical shifts have made use of highly shifted protons that were identifiable at the edges of relatively low resolution fast magic angle spinning spectra, often involved in specific hydrogen bonding configurations<sup>19</sup>.

Here we have shown that with high-resolution proton-proton correlation spectra proton chemical shifts can be assigned to crystal structures in the same way as carbon-13 shifts, for powdered solids at natural isotopic abundance, and that they can provide substantially more sensitive experimental protocols for this type of approach. The reproduction of the proton chemical shifts here has an rmsd of about 0.3 ppm, which is sufficient to confirm the assignment of the structure, in spite of the fact that the compound considered here, the K salt of penicillin G, contains 13 non-equivalent protons of which at least seven are non-aromatic and non-hydrogen bonded.

In conclusion, using a combination of <sup>1</sup>H DQ-CRAMPS NMR, two-dimensional <sup>1</sup>H-<sup>13</sup>C INEPT NMR and computational calculations, we have been able to assign all the <sup>1</sup>H and <sup>13</sup>C resonances of the K salt of penicillin G in powder at natural abundance to the crystal structure. This approach can be easily extended to other organic compounds.

We will see in the next section if it is possible to do directly molecular structure determination in powders using proton spectroscopy in solids.

## A.3. Molecular Structure Determination in Powders

### A.3.1. Introduction

Solid-state NMR has identified itself as a valuable probe of local molecular structure, in particular because of its ability to accurately determine distances or identify close proximities between specific nuclei. Most solid-state NMR techniques, which exploit dipolar couplings in this way probe rare spins such as  $^{13}\text{C}$  and  $^{15}\text{N}$ . However, the potential of techniques that directly probe  $^1\text{H}$ - $^1\text{H}$  dipolar couplings is being increasingly recognized<sup>19-26</sup>.

The improvements in spectral resolution mentioned in the previous section allow us to record multi-dimensional proton-proton correlation spectra<sup>21, 121</sup>, including spin diffusion correlation spectra of the type shown in figure A.14, where cross peaks between the two sites occur due to a dipolar driven spin exchange process, which takes place during the mixing time  $\tau_{\text{SD}}$ . Spin diffusion in the solid-state is largely the result of a coherent and reversible process due to dipolar couplings<sup>122, 123</sup>. Internuclear distances thus determine the kinetics of spin diffusion, but the poor resolution available from proton spectra has until now considerably limited the utilization of  $^1\text{H}$ - $^1\text{H}$  spin diffusion data at the molecular level.

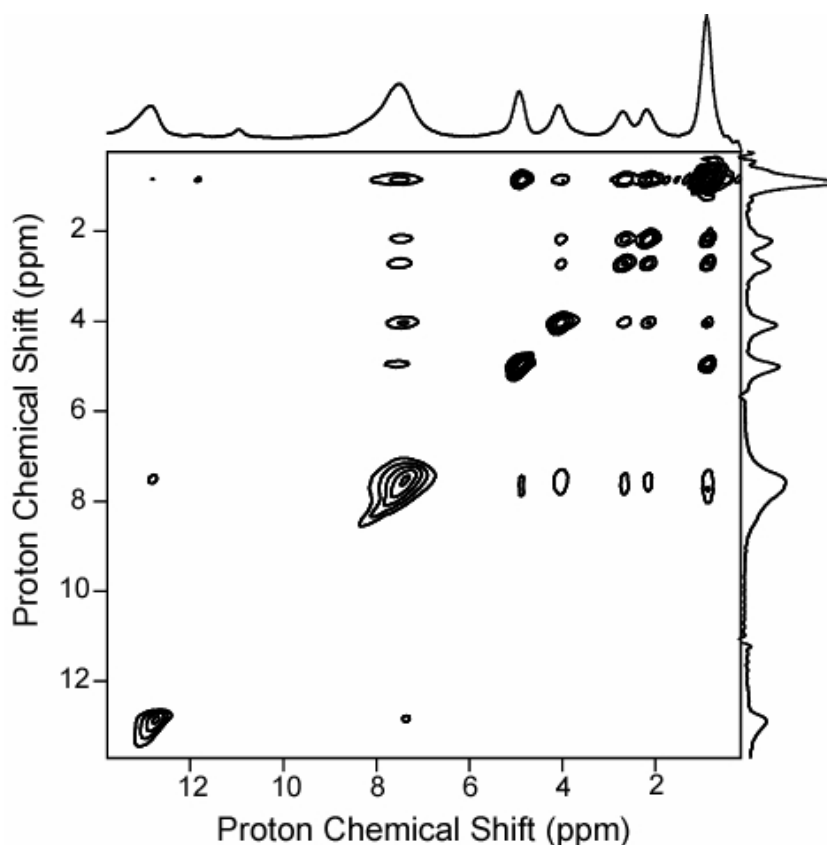


**Figure A.14.** 500 MHz 2D  $^1\text{H}$ - $^1\text{H}$  spin diffusion spectrum of (1) acquired with a MAS frequency of 22 kHz, a mixing time  $\tau_{\text{SD}}=220 \mu\text{s}$  and a radio-frequency field amplitude  $\nu_1 \approx 100\text{kHz}$ . 16 transients were added with a 2.5 s repetition delay for each of the 180 complex  $t_1$  points ( $96 \mu\text{s}$   $t_1$  increment), acquired using a States quadrature detection scheme on the second  $90^\circ$  pulse. The total experimental time was 2 hours. For proton homonuclear dipolar decoupling during  $t_1$  an intermediate version from the eDUMBO-1 decoupling schemes family defined by Fourier coefficients  $\{a_n=0$  for all  $n$ ;  $b_1=0.18$ ,  $b_2=0.21$ ,  $b_3=0.03$ ,  $b_4=0.12$ ,  $b_5=-0.08$ ,  $b_6=0.125\}$ , was implemented, and  $\theta_1=1.45$  ms. During  $t_2$ ,  $6.3 \mu\text{s}$  windows were inserted for detection of a point every 3 cycles of the original DUMBO-1 decoupling scheme, as well as short  $\theta_2$  pulses ( $0.5 \mu\text{s}$ ) to suppress quadrature images in  $F_2$ . The total dwell time was  $103.3 \mu\text{s}$ . In both dimensions, the decoupling cycles were defined with 64 phase steps of 500 ns each.

Our main interest here is to determine if we can correlate site resolved  $^1\text{H}$  spin-diffusion dynamics to the three dimensional molecular arrangement that comprises both the structure of an observed molecule itself as well as the full surrounding crystal packing.  $^1\text{H}$ - $^1\text{H}$  spin diffusion has been extensively exploited in the past for characterization of natural abundance materials at a macroscopic level<sup>124, 125</sup>, but very few attempts have been described for the interpretation of  $^1\text{H}$ - $^1\text{H}$  spin diffusion dynamics at a molecular scale. Diffusive models for spatial spin diffusion<sup>126</sup>, have recently been adapted by Brus et al. to the study initial spin diffusion exchange rates as probe of local molecular order<sup>127, 128</sup>. Baldus and coworkers have reported using  $^1\text{H}$ - $^1\text{H}$  contacts in combination with other data to constrain the conformation of solid L-tyrosine-ethylester, but they neglected the contribution of the crystalline environment, by using isotopic enrichment methods<sup>85</sup>.

Theoretical models for the mechanism of spin diffusion in the solid-state have been proposed widely in the past. Many of the early descriptions<sup>123, 129, 130</sup> were primarily aimed at so called “spatial” spin diffusion (when the proton spectrum is not resolved). In the cases we consider, the extensions of the description to so-called “spectral” spin diffusion (between resolved protons), provided either in the static case<sup>31, 131, 132</sup> or under magic-angle spinning conditions<sup>133</sup> are most relevant. Spectral spin diffusion arises from zero-quantum transitions that can occur when two single-quantum transitions overlap, as determined quantitatively by zero-quantum lineshape function  $g^{\text{ZQ}}(\omega)$ . According to Kubo and McDowell<sup>133</sup>, under MAS, an uniform spin diffusion time constant  $T_{\text{SD}}$  for the sample can be evaluated after integration over all crystallite orientations, for a pair of spins  $i$  and  $j$ :

$$\frac{1}{T_{SD}} \propto (\omega_D^{ij})^2 \left[ g^{ZQ}(\omega_R) + g^{ZQ}(-\omega_R) + \frac{1}{2} g^{ZQ}(2\omega_R) + \frac{1}{2} g^{ZQ}(-2\omega_R) \right]$$

where  $\omega_R$  is the sample rotation rate, and  $\omega_D^{ij}$  stands for the magnitude of the dipolar interaction between spins  $i$  and  $j$  separated by the distance  $r_{ij}$ :

$$\omega_D^{ij} = \frac{\mu_0 \gamma_H^2 \hbar}{4\pi r_{ij}^3}$$

The principal difficulty in analyzing spin diffusion in practice arises because  $g^{ZQ}$  is difficult to evaluate precisely. This is because we cannot simply isolate the effect of a single pair of spins, and thus any quantitative analysis of  $g^{ZQ}$  for spin diffusion exchange must take into account a large strongly coupled multi-spin system involving an ensemble of mixed distances. For example, recent studies have shown that the ZQ lineshape is affected by up to hundreds of neighboring spins in the lattice<sup>134-136</sup>. Additionally, an exact description of the zero-quantum lineshape function would also have to take into account the powder and MAS, which renders its estimation extremely complicated<sup>123, 133</sup>, requiring time-dependant methods.

The quantitative reproduction of spin-diffusion dynamics from first principles is thus a formidable challenge<sup>123, 134, 135</sup>, and currently does not provide a practical route for structure determination.

## A.3.2. Proton-Proton Spin Diffusion

### A.3.2.1. Introduction

Proton spin diffusion (PSD) is a ubiquitous process in solids<sup>123</sup>, whereby magnetization is exchanged between protons according to a process driven by the internuclear distance dependent dipolar coupling. It has long been recognized that this provides in principle a probe of internuclear distances and therefore structures. However, the rate of spin diffusion also depends on the orientation of the internuclear vector in the sample, the details of the anisotropic chemical shifts of the two coupled nuclei, the coupling to other protons, and on experimental factors such as the magic angle spinning rate<sup>123</sup>. In a powder, under MAS, it is not evident to calculate spin diffusion curves from trial structures to compare with experiment.

To circumvent this problem, we recently proposed to model spin diffusion with a phenomenological multi-spin kinetic rate matrix approach, summed over the structure<sup>137</sup>. We use a model analogous to treatments developed for multi-site chemical exchange<sup>138, 139</sup>, and widely used in liquid-state NMR, using the full relaxation matrix protocol introduced by Macura and Ernst<sup>140</sup>. The analysis will relate the 2D NMR peak intensities as observed after a spin diffusion mixing time  $\tau_{SD}$ , to the full three-dimensional structure of the crystalline system through phenomenological distance dependent rate constants.

In this model<sup>137</sup> the rate of exchange between two types of spin  $i$  and  $j$  is given by:

$$k_{ij} = \sum_{\lambda} \left( \frac{\mu_0 \gamma_H^2 \hbar}{4\pi} \right)^2 \frac{A}{(r_{ij}^n)_{\lambda}} \quad \text{for } i \neq j.$$

where  $\mu_0$ ,  $\gamma$  and  $\hbar$  are the physical constants, where  $r_{ij}$  is the internuclear distance between atoms  $i$  and  $j$  and where  $A$  is a phenomenological scaling factor. The exponent  $n$  can in principle be a variable, but here it will be set to  $n = 6$ . Importantly,  $\lambda$  indicates the sum over exchange between sites  $i$  and  $j$  in different molecules in the crystalline lattice. The peak intensities,  $P_{ij}$ , observed in a two dimensional exchange spectrum are then given by<sup>137, 138</sup>:

$$P_{ij}(\tau_{SD}) = \exp[-\mathbf{K} \cdot \tau_{SD}]_{ij} \cdot M_{zj}^0.$$

where  $\mathbf{K}$  is an  $N \times N$  matrix of the rates  $k_{ij}$  of exchange between the  $N$  different resonances in the spectrum, where  $\tau_{SD}$  is the spin diffusion mixing time, and where  $M_{zj}^0$  is the intensity of the  $j$ th peak at  $\tau_{SD} = 0$ .

Therefore, for a given a molecular structure, it is possible to calculate the corresponding spin-diffusion spectrum from the rate matrix  $\mathbf{K}$ , for each mixing time  $\tau_{SD}$ , and reproduce the experimental proton-proton spin-diffusion build-up curves.

This simplified model for spin diffusion, within its validity, provides a way of back calculating spectra from trial structures, *and therefore a way of determining structures by evaluating the best fit between the data and trial structures*. We previously showed that if we assume that the molecular conformation is known, then this does provide a way to determine the crystalline unit cell parameters<sup>137</sup>. However, the more important question, that we address here, is to determine if this model is

sufficiently robust and sensitive to determine the molecular conformation inside a given unit cell.

### A.3.2.2. Experimental

The investigation of  $^1\text{H}$ - $^1\text{H}$  spin diffusion build-up curves using a rate matrix analysis approach shows that high resolution magic-angle spinning NMR of protons, applied to powdered organic compounds, provides a method to probe crystalline arrangements. The comparison between experimental  $^1\text{H}$  data and simulation is shown to depend strongly on the parameters of the crystal structure, for example on the unit cell parameters or the orientation of the molecule in the unit cell, and those parameters are experimentally determined for a model organic compound.

The experiments were done on the powdered dipeptide  $\beta$ -L-Aspartyl-L-Alanine (**1**) used without further recrystallization. The data were acquired from high-resolution two-dimensional  $^1\text{H}$ - $^1\text{H}$  correlation spectra recorded at a Larmor frequency of 500 MHz using a single channel 2.5 mm MAS probe with about 10 mg of powdered sample, with homonuclear decoupling fields of  $\nu_1 = 100$  kHz and the magic angle spinning frequency  $\nu_r = 6.25$  kHz.

The general pulse scheme used for  $^1\text{H}$ - $^1\text{H}$  spin diffusion experiments is represented in figure A.15. Proton transverse magnetization is prepared by the initial  $90^\circ$  pulse, and  $^1\text{H}$  homonuclear dipolar decoupling is achieved during  $t_1$  using eDUMBO-1 decoupling scheme<sup>57</sup>. During  $t_1$ , precession occurs in a plane perpendicular to the proton decoupling effective field, and the magnetization is then brought back into the (xy) plane by a short  $\theta_1$  pulse. The following  $90^\circ$  pulse rotates

proton magnetization towards the z-axis in preparation for the mixing period  $\tau_{SD}$ . The final  $90^\circ$  pulse rotates the longitudinal magnetization after spin diffusion into the (xy) plane for direct proton detection using a windowed version of the original DUMBO-1 homonuclear decoupling sequence<sup>55, 56</sup>. The short  $\theta_2$  pre-pulses were added for complete removal of quadrature image artefacts.

The build-up curves used for the analysis here were obtained by integrating peak volumes in a series of 14 2D spectra recorded with spin diffusion mixing times  $\tau_{SD}$  distributed from 2  $\mu\text{s}$  to 1 ms.

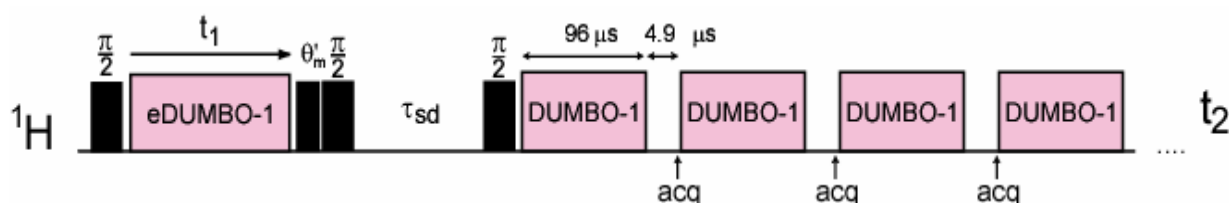


**Figure A.15.** Pulse sequence for the  $^1\text{H}$ - $^1\text{H}$  spin diffusion CRAMPS detected experiment.

Figure A.16 shows experimental spin diffusion data for (1) obtained under magic angle spinning at 6.25 kHz and using eDUMBO-1<sub>12.5</sub> homonuclear decoupling<sup>57</sup>, together with the best fit to the data obtained using the rate matrix analysis. The fit was performed using the known X-ray crystal structure for calculation of  $k_{ij}$  from internuclear distances. The least-squares function that characterizes the quality of the fit is:

$$\chi_{PSD}^2 = \sum_i \frac{(\text{calc}_i - \text{expt}_i)^2}{\sigma_i^2}$$

where  $\sigma_i$  is the estimated error on data point  $i$ .

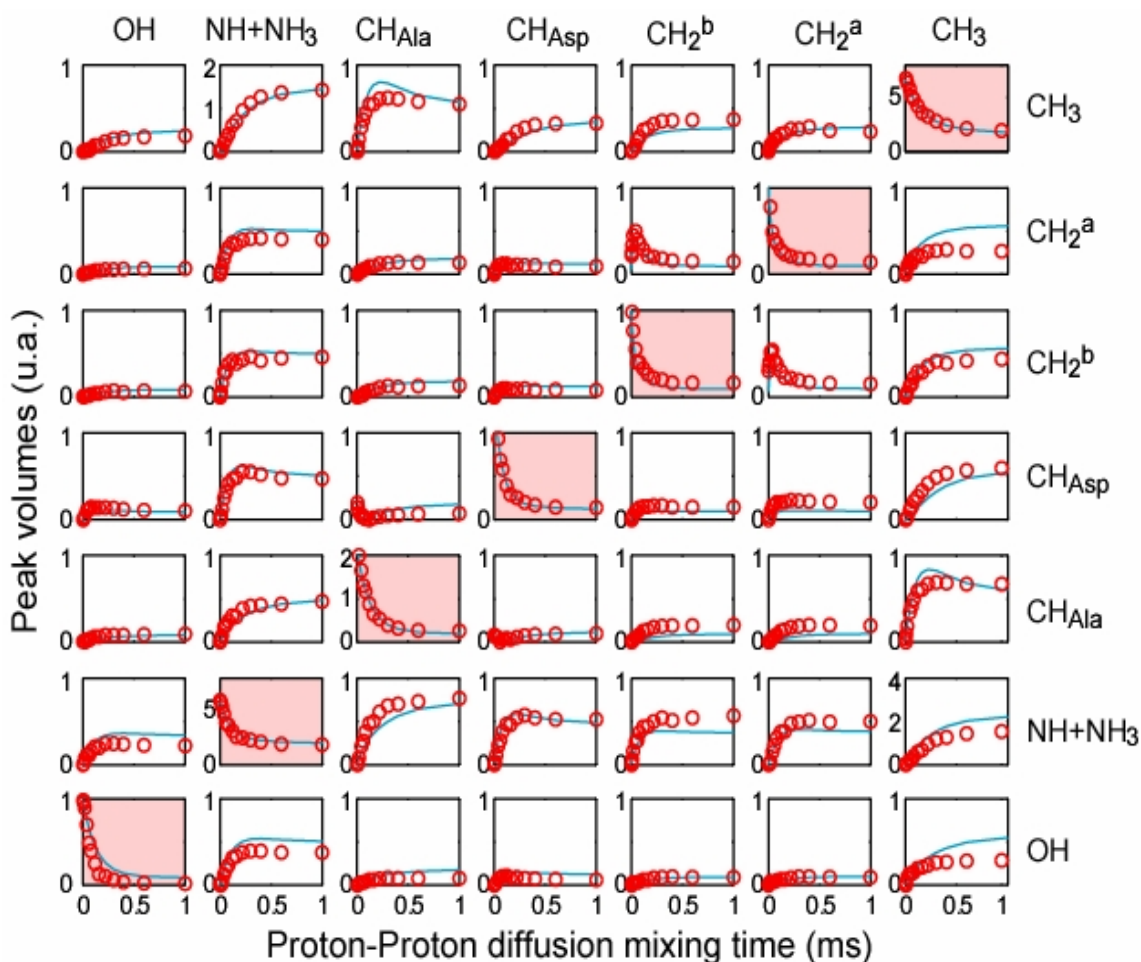


**Figure A.16.** Representative  $^1\text{H}$ - $^1\text{H}$  spin-diffusion build up curves for  $\beta$ -L-Aspartyl-L-Alanine (1). Experimental data (red o), recorded at a MAS frequency of 6.25 kHz, and best fits (blue curves) from the rate matrix analysis are compared.

More precisely, figure A.17a highlights the evolution as a function of the mixing time of nine of the 49 peaks in the spectrum. The experimental data is compared to the predicted curves for two different trial geometries, which differ from each other by a rmsd of  $0.12\text{\AA}$ . Clearly, we can evaluate that there are small but significant differences in the predicted spin diffusion behavior for these two structures, and that the structure corresponding to the green curves provides a better fit to experiment. More precisely figure A.17b shows the variation in the least squares deviation of the curves predicted for the known crystal structure<sup>141</sup> from the experimental data as we

introduce random variations into the data at the estimated level of the noise. In this case we see that the data is of sufficient quality to detect changes in the  $\chi^2_{PSD}$  of  $\sim 0.35$ . This means we can detect a significant difference between two structures that change the value of the  $\chi^2_{PSD}$  by that amount. It is important to note that this level of structural sensitivity is obtained through full back calculation of the complete PSD build up curves. Calculation of the initial rates is not sufficient to enable this analysis.

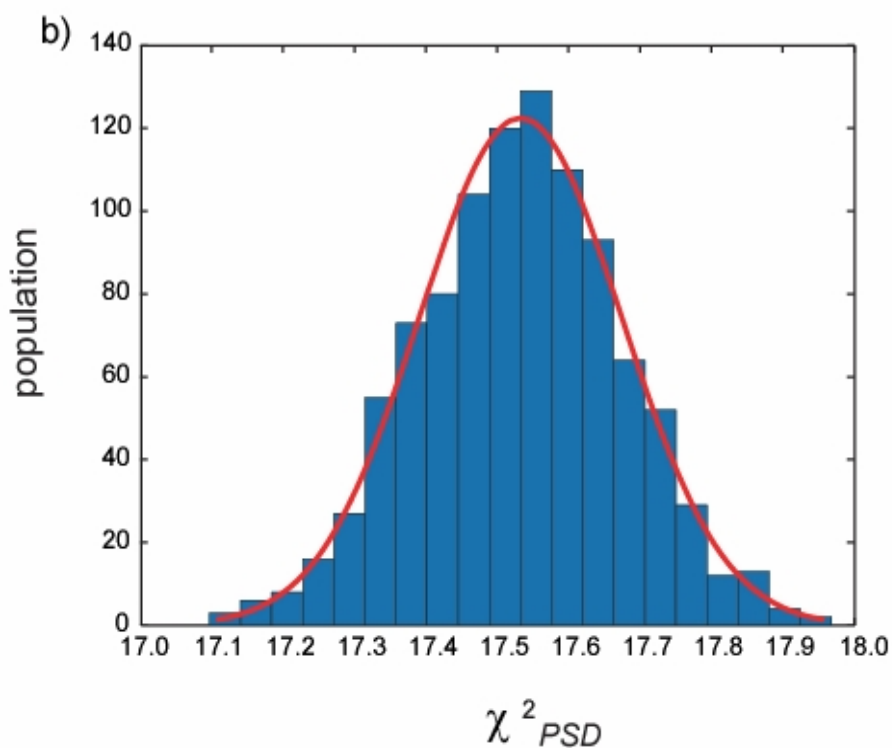
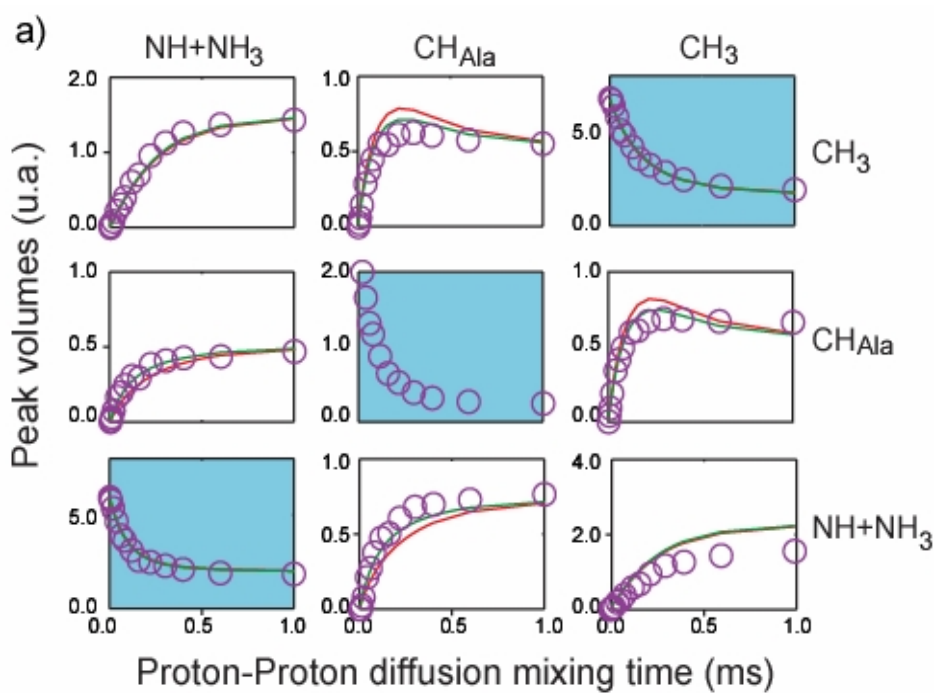


**Figure A.17.** (a) Measured peak volumes as a function of spin diffusion mixing time for nine of the 49 peaks observed in the 2D spin diffusion experiment for compound **1**. The measured values are compared to fits to the curves (in red and green) for two trial structures that differ from each other by an rmsd of 0.12 Å. (b) Measured distribution of the values of  $\chi^2_{PSD}$  for the

comparison between the data and the known crystal structure, as random changes in the data are introduced. 1000 artificial datasets were generated by adding noise to the experimental data from a Gaussian distribution with a standard deviation of 1% of the volume of the OH peak at  $\tau=0$ , which is the estimated value of the noise induced error in the measure of the cross peak volumes. The red curve is a Gaussian function with full width at half height of 0.35.

### A.3.3. Introduction to Xplor-NIH

Xplor<sup>142</sup>, which was initially derived from the generalized molecular dynamics and minimization program CHARMM<sup>143</sup>, can be used to determine and refine solution NMR structures<sup>144-149</sup> using interproton distances estimates and other NMR information such as coupling constants measurements and to refine X-ray structure<sup>150</sup>. Xplor became popular for biomolecular structure determination thanks to the development of the different packages like CNS<sup>151</sup> or NIH<sup>152, 153</sup>.

The most recent package is Xplor-NIH and is generalized in structure determination using minimization protocols based on molecular dynamics and simulated annealing. This is done by seeking the minimum energy of the function using different internal (Van der Waals, covalence,...) and external potential energy terms like NMR restraints.

The minimization procedures are achieved using molecular dynamics in Cartesian or in torsion angle space, Monte Carlo methods and conventional gradient-based minimization.

Concerning the NMR restraints, the most important is the NOE potential term and its multiple forms are supported including harmonic, biharmonic<sup>144</sup>, square-well<sup>148</sup> and a form containing an asymptotic cutoff for very large violations<sup>154</sup>. Complimentary to NOE restraints, there are residual dipolar couplings for fixed distance vectors<sup>155, 156</sup> and vectors of variable length such as proton-proton vectors<sup>157</sup>, chemical shift anisotropy<sup>158, 159</sup> and heteronuclear  $T_1/T_2$  ratios for molecules that tumble anisotropically<sup>160, 161</sup>.

For the covalent geometry, Xplor-NIH uses the usual idealized covalent energy terms that ensure that fixed bond lengths, bond angles, planar atom groups and chiral centers are correct.

For the non-bonded contacts, Xplor-NIH uses an attractive-repulsive quartic Van der Waals term<sup>154, 162, 163</sup> which prevents atoms from overlapping and that can be scaled down such that atoms may move through each other.

In addition to this potential term are conventional empirical terms like Lennard-Jones, electrostatic and dihedral angle potentials from the CHARMM empirical energy function. Finally, a radius of gyration potential<sup>164</sup> can be used to optimize internal packing.

### **A.3.4. Structure Determination**

#### **A.3.4.1. Combined PSD and Molecular Modeling**

We have integrated the full back-calculation of the spectrum from a trial structure, and the evaluation of the difference with respect to the experimental data,

as an external routine into the Xplor-NIH molecular modeling (MM) package<sup>151, 153</sup>. Within this framework, we can optimize trial geometries by combining the internal MM energy term, which maintains reasonable covalent geometry, and a standard Van der Waals potential, which maintains physically reasonable crystal structures, and the PSD pseudo energy (which is the measured  $\chi^2$  obtained by back calculation from the trial structure using the model of equations described previously).

Back calculation of the spectral intensities from trial coordinates, and comparison with the data, was achieved by a home written C++ routine. Comparison with the data to provide the value of  $\chi_{PSD}^2$  used a fitting routine that only adjusted the value of  $A$  in equation of the  $k_{ij}$  to provide the lowest possible value of  $\chi_{PSD}^2$  for each trial structure. The C++ program was then interfaced to the Python scripting language using the SWIG interpreter, and integrated into the Python scripting framework of Xplor-NIH as a new potential term, using the Xplor-NIH pyPot module<sup>142</sup>. In the structure calculations shown here a CHARMM19/22 empirical energy function was employed, with standard periodic Van der Waals and electrostatic terms. The crystalline environment and the periodic interactions are enabled in Xplor through the “xrefin” statement. Calculations were carried out using the following unit cell parameters, P2<sub>1</sub>2<sub>1</sub>2<sub>1</sub>,  $a = 4.845\text{\AA}$ ,  $b = 9.409\text{\AA}$ ,  $c = 19.170\text{\AA}$ ,  $\alpha = \beta = \gamma = 90^\circ$ <sup>33</sup>. There are four symmetry related (NMR equivalent) molecules in the unit cell as shown in figure A.18. The back calculation took account of all pairs of atoms within a radius of 10Å of the atoms in the central molecule.

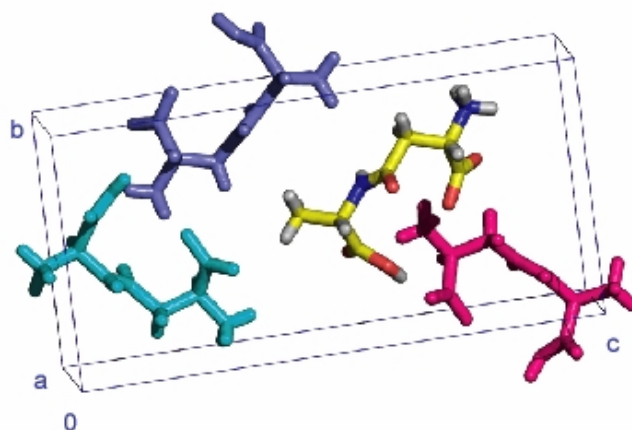


**Figure A.18.** X-Ray determinative single Crystal structure of  $\beta$ -L-Aspartyl-L-Alanine (**1**). The orthorhombic unit cell (space group  $P2_12_12_1$ ) contains 4 symmetry related NMR-equivalent molecules.

Then a standard molecular dynamics protocol was applied to "shuffle" the structure into an ensemble compatible with crystalline packing in three steps: (i) a high temperature (3000K) loop with covalent restraints but no Van der Waals repulsion term; (ii) a 100-step cycle with the inter- and intra-molecular Van der Waals radius and force constant being incrementally raised along with changes in the force constants for angles and improper dihedral angles; and (iii) a cooling loop, where all the weights were incrementally raised to their final values. 3000 structures out of a total of 45000 were then selected on the basis of their Van der Waals energy. The rmsd from the average for this group of 3000 random structures was 2.3Å). Each of the members of the starting ensemble of 3000 structures was generated by starting from a "template" coordinate set having an arbitrary extended conformation with ideal geometry, obtained from randomly generated coordinates, on which dynamics and minimization were run to anneal the structure to a reasonable covalency.

The structure refinement process was then carried out in 5 steps. First, an optimization of all 3000 structures was performed by systematically varying the CH<sub>3</sub>, NH<sub>3</sub> and OH dihedral angles and retaining the structure with the lowest value of  $E_{PSD}$ . Note that these structures, that are randomly generated, do not occupy space in a random fashion, but already limit the structure determination to more or less physically reasonable structures, thereby introducing a significant reduction in the structural space that needs to be explored using the experimental PSD constraints. Figure A.19a shows the result of refining these structures using an energy given by:

$$E_{tot} = E_{Xplor} + E_{PSD}$$

where  $E_{Xplor}$  is a standard MM force field including standard covalent terms, Van der Waals, and electrostatic terms, and where  $E_{PSD} = a_{PSD} \chi_{PSD}^2$  with  $a_{PSD}$  being the weight of the experimental constraints.  $E_{tot}$  is used as a cost function in a simplex minimization protocol of the Xplor-NIH package.

The back-calculated PSD energy,  $E_{PSD}$ , was evaluated for all 3000 members of the ensemble and the 200 structures which had the lowest values were then refined using the simplex procedure against  $E_{tot}$ . The 200 structures with the lowest  $E_{PSD}$  in the resulting ensemble were then optimized using  $E_{tot}$  in an all atom simplex minimization of up to 3000 steps. The value of  $a_{PSD}$  was 35 and only inter-molecular Van der Waals terms were used (with no electrostatics).

The ensemble of 200 structures was then regularized by a Powell type minimization using only  $E_{Xplor}$  with the same parameters. The ensemble was then re-optimized by a second simplex minimization using  $E_{tot}$  with Van der Waals and electrostatics forces including both inter- and intra-molecular terms, and finally the CH<sub>3</sub>, NH<sub>3</sub> and OH dihedral angles were re-optimized against  $E_{PSD}$  alone.

The 16 structures with the lowest  $E_{PSD}$  values were used in the ensemble shown in figure A.19b and they vary in  $\chi_{PSD}^2$  from 15.9 to 16.2. Figure A.19b shows the 16 structures with the lowest values of  $E_{PSD}$  after the refinement procedure and the exclusion of structures with unreasonably large intra-molecular Van der Waals energies. These structures deviate from each other by an ensemble rmsd for all atoms of only 0.09Å (excluding the protons on the CH<sub>3</sub> and NH<sub>3</sub> groups), and deviate from the known crystal structure by an all atom rmsd of only 0.33Å.

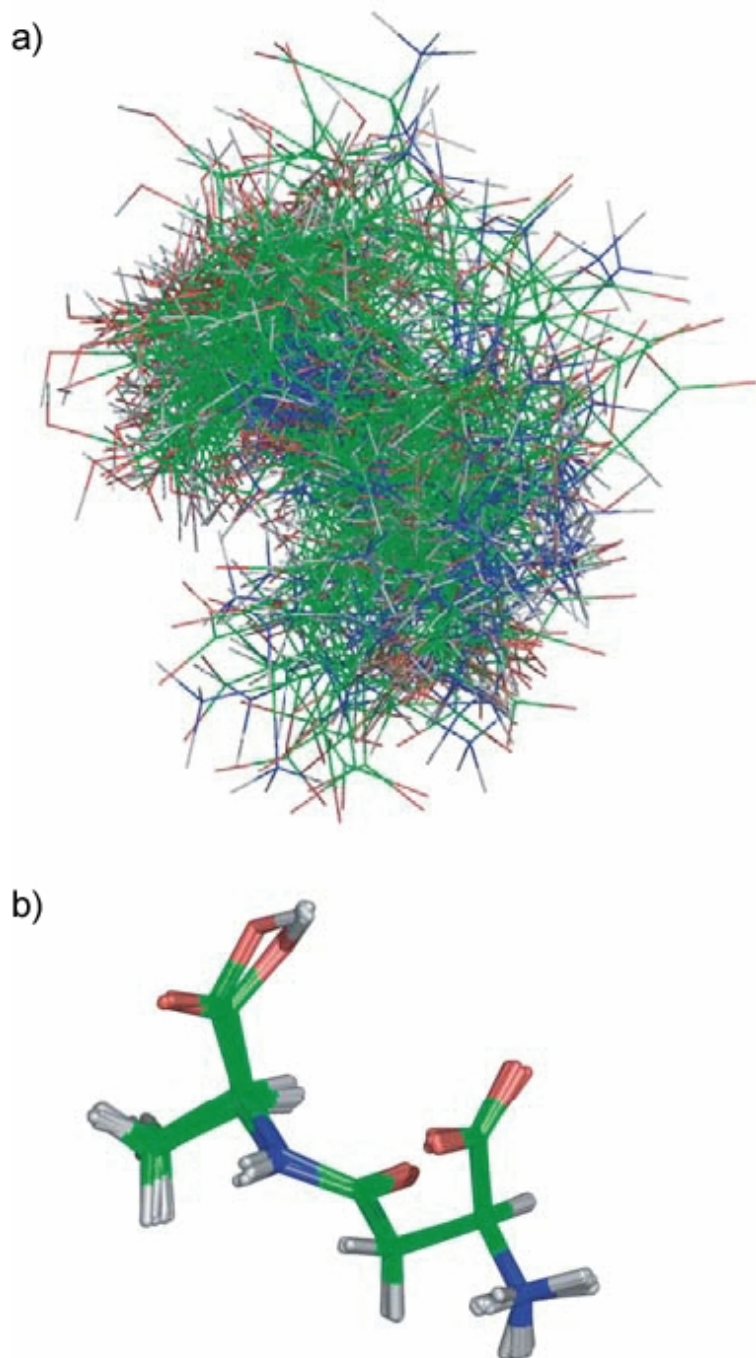


**Figure A.19.** (a) A set of 200 structures from the ensemble of 3000 random structures used as the starting point for the structure refinement. (b) The 16 structures determined with the lowest  $E_{PSD}$  values after the optimization procedure described below represented in the orthorhombic unit cell (space group  $P2_12_12_1$ ).

### A.3.4.2. Results and Discussion

Figure A.20 illustrates the crystal structure and packing determined here as represented by the average coordinates of the 16 lowest  $E_{PSD}$  structures. Figure A.20a shows the deviation of the average structure found here from the known crystal structure (in orange). This clearly illustrates that, at least in favorable conditions, and if the experimental data is of sufficient quality, PSD data can be used to determine crystal structures in powdered samples at natural abundance.

Furthermore, a particularly interesting factor is that this structure determination protocol uses proton positions as the basis for the determination. In that sense it is highly complimentary to X-ray diffraction studies, which are guided primarily by heavy atoms, and where proton positions are the hardest to determine. Notably, when we visualize the whole crystal lattice as determined here, in Figure A.20b, we can see that the OH and NH protons are positioned in reasonable intermolecular hydrogen bonding configurations. This is determined directly in the procedure, and does not rely on positioning the protons once the heavy atoms have been determined (rather the inverse). We also remark that diffraction and NMR data are further complimentary in that where diffraction is by nature a global effect, and probes the whole lattice directly, into which one has to position the individual nuclei, NMR in contrast provides a local, atomic level, probe, with interactions that “reach out” to determine the lattice.

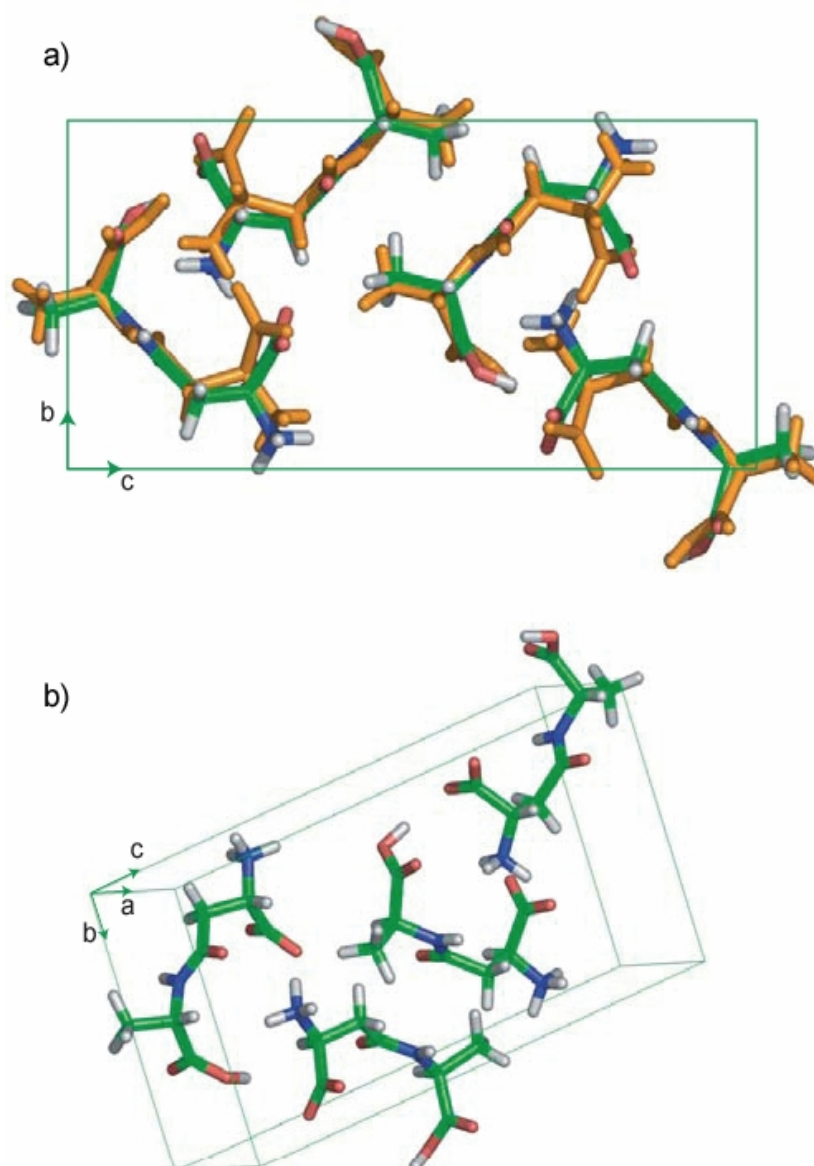


**Figure A.20.** (a) Comparison between the known crystal structure of (**1**) in orange, and the structure obtained from the average coordinates of the 16 structures determined here with the lowest  $E_{PSD}$  values as described in the text. The view is taken along the a axis of the unit cell. (b) A second view of the average structure determined here, illustrating the packing arrangement from another angle.

The structure we determine here appears to have a systematic deviation from the X-ray determined structure. We can imagine several sources of this error, most of which could be improved in the future. The most obvious are that the spin diffusion

data, which are the fruit of currently state of the art NMR experiments, may contain artifacts in the intensity of certain peaks. Indeed, other data sets we have recorded, where we are conscious of problems in the spectra, lead to varying degrees of success in the convergence of the refinement, indicating that high-quality data are essential to obtain good structures. Structural deviations may also be induced because the model we use to fit the data is not correct.

Apart from the validity of the single exponential approximation, the geometrical model may itself be wrong, as we have approximated the motion of the protons of the CH<sub>3</sub> and NH<sub>3</sub> groups (which from the NMR spectrum are clearly undergoing rapid motion) by a simple fast three site jump model (which is achieved by simply setting the exchange rate constants for magnetization transfer between these protons to be two orders of magnitude faster than the other, dipolar driven, exchange rates). This three-site jump model (slightly) improves the fit quality with respect to a single configuration. However, it is quite probable that these protons are undergoing continuous motion around the C<sub>3</sub> axis, and that a model reproducing this type of dynamics would provide even better structures. Indeed, we can observe in figure A.21 that protons of the CH<sub>3</sub> and NH<sub>3</sub> groups can have preferential orientation which can influence the calculation of the  $E_{PSD}$  value.

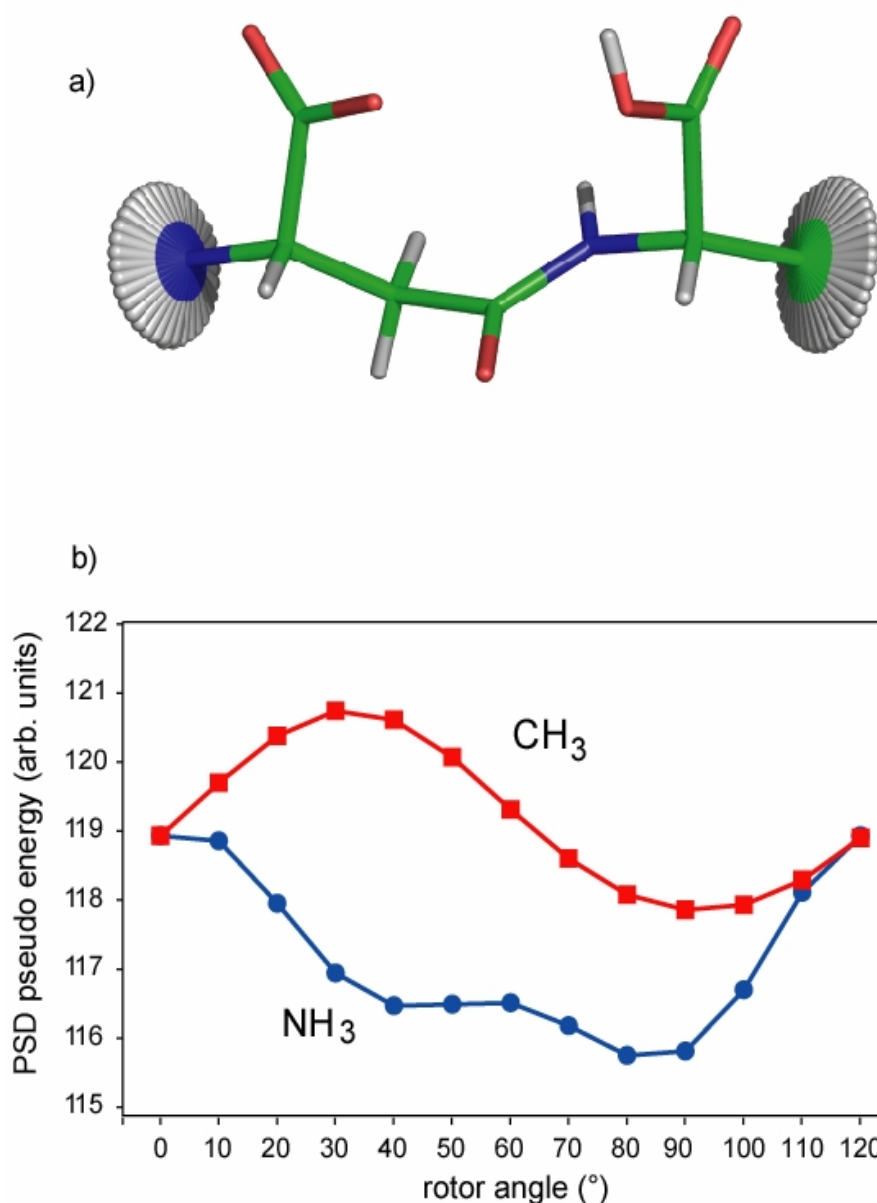


**Figure A.21.** (a) Schematic representation. (b)  $E_{PSD}$  value for the protons of CH<sub>3</sub> and NH<sub>3</sub> group respectively in function of their relative position in the three-site jump model.

In the same way, we remark that we have consciously made very little attempt to optimize the MM force field parameters, which could also lead to induction of unfavorable structures. This is particularly the case for the orientation and position of the two carboxylic acid groups present in this molecule. Indeed, as shown in figure A.22, the  $E_{PSD}$  value seems to strongly depend on the proton position of the carboxyl

group. The  $E_{PSD}$  value strongly varies when rotating the OH vector and on which the proton is associated with the carboxyl group. So, it appears that there is a preferential position of the proton. Thus, given the heavy atoms positions, we can locate the most probable position and orientation of the proton in the carboxylic acid group.

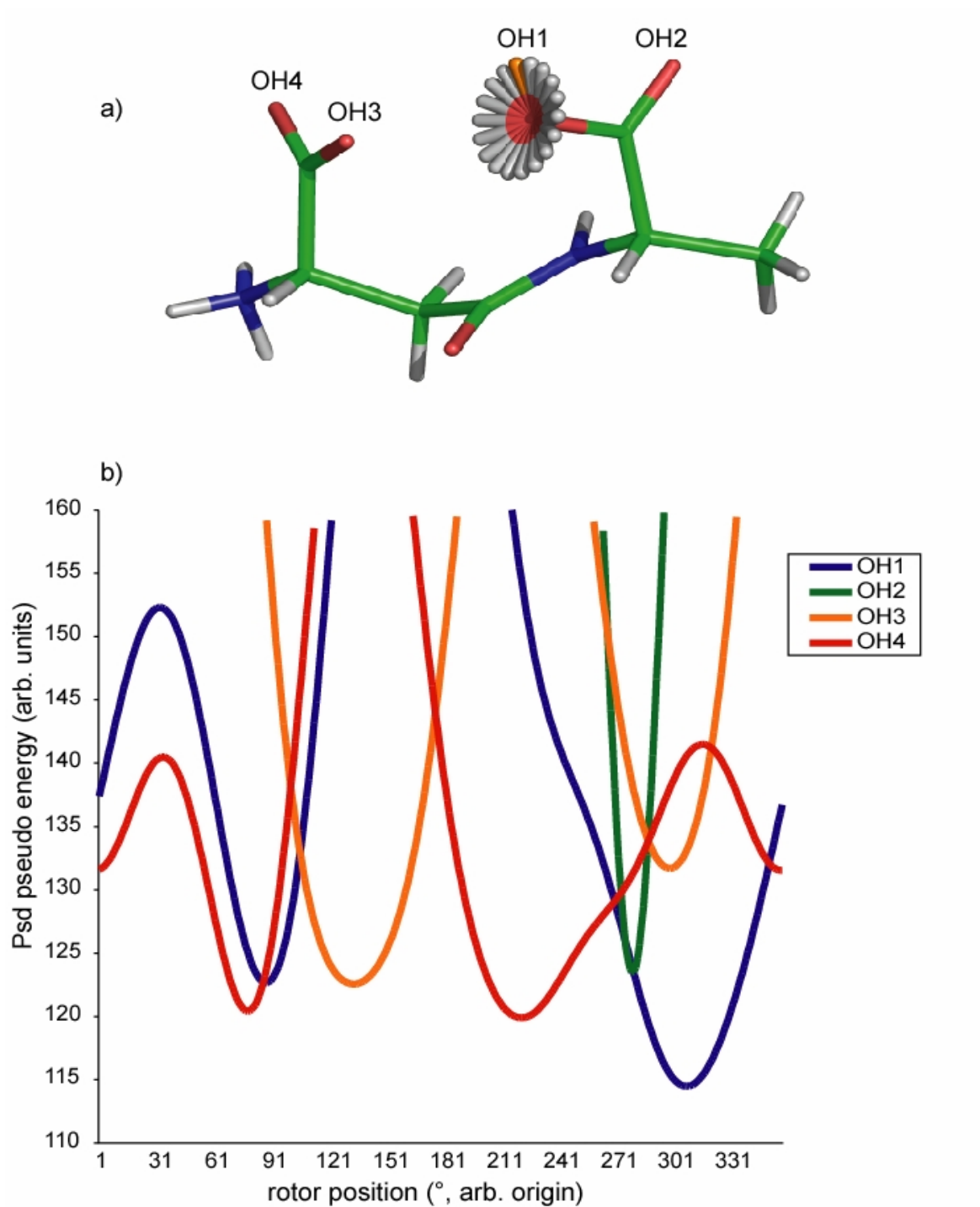


**Figure A.22.** (a) Schematic representation. (b)  $E_{PSD}$  value for the proton of each carboxyl group in function of the OH angle.

The orientation of the carboxyl group depends only little on the proton positions, and so is largely determined by the force field we use here. Position of the

hydrogen of the acid carboxyl group also seems to be dependent of the NH<sub>3</sub> group. Indeed, it seems that there is a preferential orientation of the proton of the carboxyl group towards the protons of the NH<sub>3</sub> groups which minimize the  $E_{PSD}$  value and support an hydrogen bond (figure A.23) as shown by Gorbitz with X-Ray crystallography<sup>141</sup>. This highlights again how this NMR based structure is defined by the proton positions, which are themselves found to be in remarkably good agreement with the known structure.

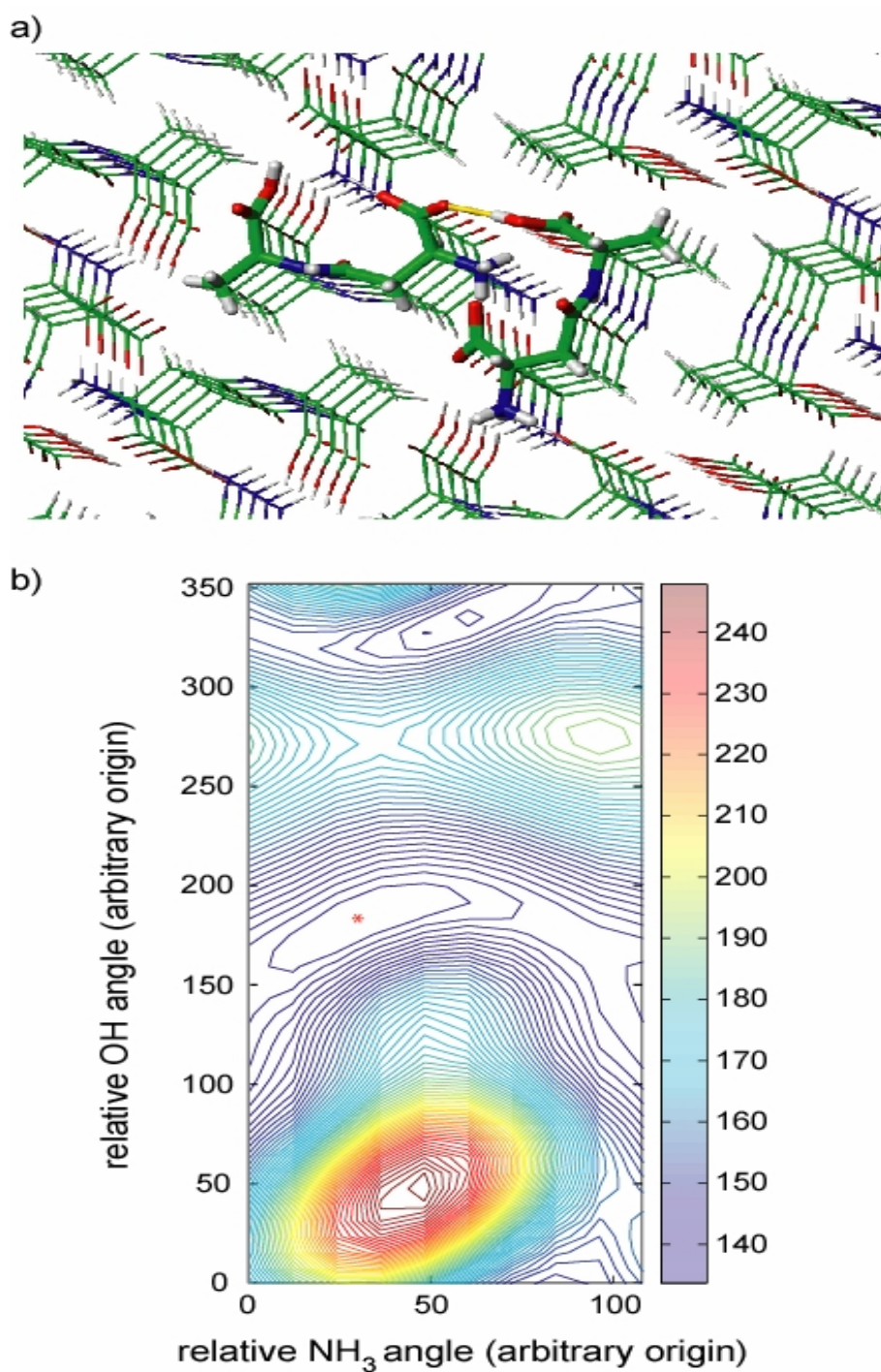


**Figure A.23.** (a) Hydrogen bond favored in yellow. (b)  $E_{PSD}$  value in function of the relative OH angle and of the angle of the NH bond in the  $\text{NH}_3$  group in the three-site jump model.

### A.3.5. Perspectives

We have shown that directly detected  $^1\text{H}$ - $^1\text{H}$  spin diffusion CRAMPS experiments can be used for the refining determination of the structure of an ordinary powdered micro-crystalline organic compound at natural isotopic abundance using a phenomenological rate matrix analysis approach. The remarkable agreement between the data and the model appear to validate the assumptions about spin diffusion dynamics. Dipolar coupling networks extend over relatively large distances and thus require the molecule in its full crystal environment to obtain good agreement with experiment.

We have introduced a combined MM / NMR-PSD approach, using a model for the back calculation of the full PSD build-up curves, which enables us to determine the molecular structure of (**1**) *at natural abundance and in powdered form*, from a randomly generated starting ensemble to obtain a group of structures with a 0.09Å rmsd, and which deviate on average from the known structure by only 0.33Å.

All the sources of error discussed above can be improved by further developing the model for PSD and the experimental methods used to acquire the spectra. The comparison between experimental data and simulations was shown to depend strongly on the parameters of the crystal structure, in particular on the unit cell parameters or on the orientation of the molecule in the unit cell.

## A.4. Conclusion

The development of technical hardware and solid NMR methodology have allowed considerable advances in high-resolution solid-state Nuclear Magnetic Resonance of protons made in the past few years. Thus, the spatial part of the interaction Hamiltonian is averaged by the rotation of the sample at the magic-angle and the residual dipolar interaction is averaged by coherent averaging methods. This method is well-known as CRAMPS acquisition, and many features regarding implementation and various applications of this technique have been discussed in the present part.

Moreover, the enhanced performance of proton homonuclear dipolar averaging schemes discloses additional perspectives in the area of heteronuclear correlation spectroscopy, in particular for the development of selective through-bond correlation techniques via J couplings. Advances in the efficiency of selective polarization transfer techniques are of major interest towards the development of multi-dimensional heteronuclear correlation techniques in solids, and the applicability of inversely (proton) detected methods. Thus, combining CRAMPS and INEPT methods, it is possible to assign powders of organic compounds at natural abundance to crystal structures.

Finally, proton-proton multidimensional correlation spectroscopy in powdered solids constantly benefits from the continuous progress in proton resolution. Besides the design of new high-resolution proton techniques, the gain in proton resolution is such that one can attempt quantitative interpretation of the various possible

correlation experiments in particular for polarization transfer through  $^1\text{H}$ - $^1\text{H}$  spin diffusion, driven by direct proton-proton dipolar couplings. We investigated more precisely the proton-proton spin diffusion case, and proposed a phenomenological approach, based on standard complete relaxation matrix analysis and a molecular dynamics program, for simulation and structural interpretation of the proton spin-diffusion build-up curves. Within this framework, it should be possible to determine the molecular structure of small organic powders at natural abundance. Thus this approach provides us with very encouraging basis for the development of more advanced methodology, towards powder crystallography by proton high-resolution NMR spectroscopy<sup>164</sup>.

## A.5. References

1. Edman, K.; Nollert, P.; Royant, A.; Belrhali, H.; Pebay-Peyroula, E.; Hajdu, J.; Neutze, R.; Landau, E.M., High-resolution X-ray structure of an early intermediate in the bacteriorhodopsin photocycle. *Nature*. 1999, 401, 822-826.
2. Palczewski, K.; Kumasaka, T.; Hori, T.; Behnke, C.A.; Motoshima, H.; Fox, B.A.; Le Trong, I.; Teller, D.C.; Okada, T.; Stenkamp, R.E.; Yamamoto, M.; Miyano, M., Crystal structure of rhodopsin: A G protein-coupled receptor. *Science*. 2000, 289, 739-745.
3. Abrescia, N.G.A.; Cockburn, J.J.B.; Grimes, J.M.; Sutton, G.C.; Diprose, J.M.; Butcher, S.J.; Fuller, S.D.; Martin, C.S.; Burnett, R.M.; Stuart, D.I.; Bamford, D.H.; Bamford, J.K.H., Insights into assembly from structural analysis of bacteriophage PRD1. *Nature*. 2004, 432, 68-74.
4. Trikalitis, P.N.; Rangan, K.K.; Bakas, T.; Kanatzidis, M.G., Varied pore organization in mesostructured semiconductors based on the  $[\text{SnSe}_4]^{4-}$  anion. *Nature*. 2001, 410, 671-675.
5. Chichak, K.S.; Cantrill, S.J.; Pease, A.R.; Chiu, S.H.; Cave, G.W.V.; Atwood, J.L.; Stoddart, J.F., Molecular Borromean rings. *Science*. 2004, 304, 1308-1312.

6. Bretonniere, Y.; Mazzanti, M.; Pecaut, J.; Olmstead, M.M., Cation-controlled self-assembly of a hexameric europium wheel. *J. Am. Chem. Soc.* 2002, 124, 9012-9013.
7. Schotte, F.; Lim, M.H.; Jackson, T.A.; Smirnov, A.V.; Soman, J.; Olson, J.S.; Phillips, G.N.; Wulff, M.; Anfinrud, P.A., Watching a protein as it functions with 150-ps time-resolved X-ray crystallography. *Science*. 2003, 300, 1944-1947.
8. Ihee, H.; Lorenc, M.; Kim, T.K.; Kong, Q.Y.; Cammarata, M.; Lee, J.H.; Bratos, S.; Wulff, M., Ultrafast x-ray diffraction of transient molecular structures in solution. *Science*. 2005, 309, 1223-1227.
9. Harris, K.D.M.; Cheung, E.Y., How to determine structures when single crystals cannot be grown: opportunities for structure determination of molecular materials using powder diffraction data. *Chem. Soc. Rev.* 2004, 33, 526-538.
10. Laws, D.D.; Bitter, H.M.L.; Jerschow, A., Solid-state NMR spectroscopic methods in chemistry. *Angew. Chem.-Int. Edit.* 2002, 41, 3096-3129.
11. Castellani, F.; Van Rossum, B.; Diehl, A.; Schubert, M.; Rehbein, K.; Oschkinat, H., Structure of a protein determined by solid-state magic-angle-spinning NMR spectroscopy. *Nature*. 2002, 420, 98-102.
12. Petkova, A.T.; Ishii, Y.; Balbach, J.J.; Antzutkin, O.N.; Leapman, R.D.; Delaglio, F.; Tycko, R., A structural model for Alzheimer's beta-amyloid fibrils based on experimental constraints from solid state NMR. *Proc. Natl. Acad. Sci. U. S. A.* 2002, 99, 16742-16747.
13. Tycko, R., Progress towards a molecular-level structural understanding of amyloid fibrils. *Curr. Opin. Struct. Biol.* 2004, 14, 96-103.
14. Jaroniec, C.P.; MacPhee, C.E.; Bajaj, V.S.; McMahon, M.T.; Dobson, C.M.; Griffin, R.G., High-resolution molecular structure of a peptide in an amyloid fibril determined by magic angle spinning NMR spectroscopy. *Proc. Natl. Acad. Sci. U. S. A.* 2004, 101, 711-716.
15. Brouwer, D.H.; Darton, R.J.; Morris, R.E.; Levitt, M.H., A solid-state NMR method for solution of zeolite crystal structures. *J. Am. Chem. Soc.* 2005, 127, 10365-10370.
16. Fyfe, C.A.; Diaz, A.C.; Grondey, H.; Lewis, A.R.; Forster, H., Solid state NMR method for the determination of 3D zeolite framework/sorbate structures: H-1/Si-29 CP MAS NMR study of the high-loaded form of p-xylene in ZSM-5 and determination of the unknown structure of the low-loaded form. *J. Am. Chem. Soc.* 2005, 127, 7543-7558.
17. Brouwer, D.H.; Kristiansen, P.E.; Fyfe, C.A.; Levitt, M.H., Symmetry-based Si-29 dipolar recoupling magic angle spinning NMR spectroscopy: A new method for investigating three-dimensional structures of zeolite frameworks. *J. Am. Chem. Soc.* 2005, 127, 542-543.

18. Beitone, L.; Huguenard, C.; Gansmuller, A.; Henry, M.; Taulelle, F.; Loiseau, T.; Ferey, G., Order-disorder in the super-sodalite  $Zn_3Al_6(PO_4)(12)$ , 4tren, 17H(2)O (MIL-74): A combined XRD-NMR assessment. *J. Am. Chem. Soc.* 2003, 125, 9102-9110.
19. Brown, S.P.; Spiess, H.W., Advanced solid-state NMR methods for the elucidation of structure and dynamics of molecular, macromolecular, and supramolecular systems. *Chem. Rev.* 2001, 101 (12), 4125-4155.
20. Reif, B.; Jaroniec, C.P.; Rienstra, C.M.; Hohwy, M.; Griffin, R.G., H-1-H-1 mas correlation spectroscopy and distance measurements in a deuterated peptide. *J. Magn. Reson.* 2001, 151 (2), 320-327.
21. Sakellariou, D.; Lesage, A.; Emsley, L., Proton-proton constraints in powdered solids from H-1-H-1-H-1 and H-1-H-1-C-13 three-dimensional NMR chemical shift correlation spectroscopy. *J. Am. Chem. Soc.* 2001, 123 (23), 5604-5605.
22. Lange, A.; Seidel, K.; Verdier, L.; Luca, S.; Baldus, M., Analysis of proton-proton transfer dynamics in rotating solids and their use for 3D structure determination. *J. Am. Chem. Soc.* 2003, 125 (41), 12640-12648.
23. Reif, B.; van Rossum, B.J.; Castellani, F.; Rehbein, K.; Diehl, A.; Oschkinat, H., Characterization of H-1-H-1 distances in a uniformly H-2,N-15-labeled SH3 domain by MAS solid-state NMR spectroscopy. *J. Am. Chem. Soc.* 2003, 125 (6), 1488-1489.
24. Paulson, E.K.; Morcombe, C.R.; Gaponenko, V.; Danchek, B.; Byrd, R.A.; Zilm, K.W., High-sensitivity observation of dipolar exchange and NOEs between exchangeable protons in proteins by 3D solid-state NMR spectroscopy. *J. Am. Chem. Soc.* 2003, 125 (47), 14222-14223.
25. Matsuki, Y.; Akutsu, H.; Fujiwara, T., Precision H-1-H-1 distance measurement via C-13 NMR signals: Utilization of H-1-H-1 double-quantum dipolar interactions recoupled under magic angle spinning conditions. *Magn. Reson. Chem.* 2004, 42 (2), 291-300.
26. Vinogradov, E.; Madhu, P.K.; Vega, S., Proton spectroscopy in solid state nuclear magnetic resonance with windowed phase modulated lee-goldburg decoupling sequences. *Chem. Phys. Lett.* 2002, 354 (3-4), 193-202.
27. Waugh, J.S.; Huber, L.M.; Haeberlen, U., Approach to high-resolution NMR in solids. *Phys. Rev. Lett.* 1968, 20 (5), 180-182.
28. Haeberlen, U.; Waugh, J.S., Coherent averaging effects in magnetic resonance. *Phys. Rev.* 1968, 175 (2), 453-467.
29. Mehring, M.; Waugh, J.S., Magic-angle NMR experiments in solids. *Phys. Rev. B* 1972, 5 (9), 3459-3471.
30. Suter, D.; Ernst, R.R., Spectral spin diffusion in the presence of an extraneous dipolar reservoir. *Phys. Rev. B* 1982, 25 (9), 6038-6041.

31. Suter, D.; Ernst, R.R., Spin diffusion in resolved solid-state NMR-spectra. *Phys. Rev. B* 1985, 32 (9), 5608-5627.
32. Ernst, R.R.; Bodenhausen, G.; Wokaun, A., Principles of nuclear magnetic resonance in one and two dimensions. Clarendon Press: Oxford, 1987.
33. Mehring, M., Principles of high resolution NMR in solids. Springer: Berlin, 1983.
34. Andrew, E.R.; Bradbury, A.; Eades, R.G., Removal of dipolar broadening of nuclear magnetic resonance spectra of solids by specimen rotation. *Nature* 1959, 183 (4678), 1802-1803.
35. Lowe, I.J., Free induction decays of rotating solids. *Phys. Rev. Lett.* 1959, 2 (7), 285- 287.
36. Samoson, A.; Tuhem, T.; Past, J.; Reinhold, A.; Anupold, T.; Heinmaa, I., New horizons for magic-angle spinning NMR. 246 ed.; 2005; p 15-31.
37. Emsley, L.; Laws, D.D.; Pines, A., Lectures on pulsed NMR (3rd edition). In Proceedings of the international school of physics, enrico fermi, course cxxxix, Maraviglia, B., Ed. 1998.
38. Maricq, M.M.; Waugh, J.S., NMR in rotating solids. *J. Chem. Phys.* 1979, 70 (7), 3300-3316.
39. Haeberlen, U., High resolution NMR in solids: Selective averaging. In Advances in magnetic resonance , Waugh, J. S., Ed. Academic Press: New York, 1976; Vol. Supplement 1.
40. Gerstein, B.C.; Pembleton, R.G.; Wilson, R.C.; Ryan, L.M., High resolution NMR in randomly oriented solids with homonuclear dipolar broadening: Combined multiple pulse NMR and magic angle spinning. *J. Chem. Phys.* 1977, 66 (1), 361-362.
41. Gerstein, B.C., Cramps. In Encyclopedia of nuclear magnetic resonance , Grant, D.M.; Harris, R.K., Eds. Wiley: Chichester, 1996; pp 1501-1509.
42. Lee, M.; Goldburg, W.I., Nuclear-magnetic-resonance line narrowing by a rotating rf field. *Phys. Rev.* 1965, 140 (4A), 1261-1271.
43. Mansfield, P.; Orchard, M.J.; Stalker, D.C.; Richards, K.H., Symmetrized multipulse nuclear-magnetic-resonance experiments in solids - measurement of chemical-shift shielding tensor in some compounds. *Phys. Rev. B* 1973, 7 (1), 90-105.
44. Rhim, W.K.; Elleman, D.D.; Vaughan, R.W., Analysis of multiple pulse NMR in solids. *J. Chem. Phys.* 1973, 59 (7), 3740-3749.
45. Burum, D.P.; Linder, M.; Ernst, R.R., Low-power multipulse line narrowing in solid- state NMR. *J. Magn. Reson.* 1981, 44 (1), 173-188.

46. Bielecki, A.; Kolbert, A.C.; Levitt, M.H., Frequency-switched pulse sequences - homonuclear decoupling and dilute spin NMR in solids. *Chem. Phys. Lett.* 1989, 155 (4-5), 341-346.
47. Bielecki, A.; Kolbert, A.C.; de Groot, H.J.M.; Griffin, R.G.; Levitt, M.H., Frequency-switched lee-goldburg sequences in solids. *Adv. Magn. Reson.* 1990, 14, 111.
48. Cory, D.G., A new multiple-pulse cycle for homonuclear dipolar decoupling. *J. Magn. Reson.* 1991, 94 (3), 526-534.
49. Levitt, M.H.; Kolbert, A.C.; Bielecki, A.; Ruben, D.J., High-resolution H-1-NMR in solids with frequency-switched multiple-pulse sequences. *Solid State Nuclear Magnetic Resonance* 1993, 2 (4), 151-163.
50. Hafner, S.; Spiess, H.W., Multiple-pulse line narrowing under fast magic-angle spinning. *J. Magn. Reson. A* 1996, 121 (2), 160-166.
51. Hohwy, M.; Nielsen, N.C., Elimination of high order terms in multiple pulse nuclear magnetic resonance spectroscopy: Application to homonuclear decoupling in solids. *J. Chem. Phys.* 1997, 106 (18), 7571-7586.
52. Vinogradov, E.; Madhu, P.K.; Vega, S., High-resolution proton solid-state NMR spectroscopy by phase-modulated lee-goldburg experiment. *Chem. Phys. Lett.* 1999, 314 (5-6), 443-450.
53. Madhu, P.K.; Zhao, X.; Levitt, M.H., High-resolution H-1 NMR in the solid state using symmetry-based pulse sequences. *Chem. Phys. Lett.* 2001, 346 (1-2), 142-148.
54. Vinogradov, E.; Madhu, P.K.; Vega, S., Phase modulated Lee-Goldburg magic angle spinning proton nuclear magnetic resonance experiments in the solid state: A bimodal floquet theoretical treatment. *J. Chem. Phys.* 2001, 115 (19), 8983-9000.
55. Sakellariou, D.; Lesage, A.; Hodgkinson, P.; Emsley, L., Homonuclear dipolar decoupling in solid-state NMR using continuous phase modulation. *Chem. Phys. Lett.* 2000, 319 (3-4), 253-260.
56. Lesage, A.; Sakellariou, D.; Hediger, S.; Elena, B.; Charmont, P.; Steuernagel, S.; Emsley, L., Experimental aspects of proton NMR spectroscopy in solids using phase- modulated homonuclear dipolar decoupling. *J. Magn. Reson.* 2003, 163 (1), 105-113.
57. Elena, B.; De Paepe, G.; Emsley, L., Direct spectral optimisation of proton-proton homonuclear dipolar decoupling in solid-state NMR. *Chem. Phys. Lett.* 2004, 398 (4-6), 532-538.
58. Lesage, A.; Duma, L.; Sakellariou, D.; Emsley L., Improved resolution in proton NMR spectroscopy of powdered solids. *J. Am. Chem. Soc.* 2001, 123, 5747-5752.

59. Vinogradov E.; Madhu, P.K.; Vega, S., Strategies for high-resolution proton spectroscopy in solid-state NMR. *Top. Curr. Chem.* 2005, 246, 33-90.
60. Madhu, P.K.; Vinogradov E.; Vega, S., Multiple-pulse and magic-angle spinning aided double-quantum proton solid-state NMR spectroscopy. *Chem. Phys. Lett.* 2004, 394, 423-428.
61. Brown, S.P.; Lesage, A.; Elena, B.; Emsley, L., Probing proton-proton proximities in the solid state: High-resolution two-dimensional H-1-H-1 double-quantum CRAMPS NMR spectroscopy. *J. Am. Chem. Soc.*, 2004, 126, 13230-13231.
62. Elena, B.; Lesage, A.; Steuernagel, S.; Bockmann, A.; Emsley, L., Proton to carbon-13 INEPT in solid-state NMR spectroscopy. *J. Am. Chem. Soc.*, 2005, 127, 17296-17302.
63. Tishmack, P.A.; Bugay, D.E.; Byrn, S.R., Solid-state nuclear magnetic resonance spectroscopy - Pharmaceutical applications. *J. Pharm. Sci.* 2003, 92, 441-474.
64. Harris, R.K.; Hodgkinson, P.; Larsson, T.; Muruganantham, A. Quantification of bambuterol hydrochloride in a formulated product using solid-state NMR. *J. Pharm. Biomed. Anal.* 2005, 38, 858-864.
65. Offerdahl, T.J.; Salsbury, J.S.; Dong, Z.D.; Grant, D.J.W.; Schroder, S.A.; Prakash, I.; Gorman, E.M.; Barich, D.H.; Munson, E.J., Quantitation of crystalline and amorphous forms of anhydrous neotame using C-13 CPMAS NMR spectroscopy. *J. Pharm. Sci.* 2005, 94, 2591-2605.
66. Portieri, A.; Harris, R.K.; Fletton, R.A.; Lancaster, R.W.; Threlfall, T.L., Effects of polymorphic differences for sulfanilamide, as seen through C-13 and N-15 solid-state NMR, together with shielding calculations. *Magn. Reson. Chem.* 2004, 42, 313-320.
67. Pawley, G.S., Unit-cell refinement from powder diffraction scans. *J. Appl. Cryst.* 1981, 14, 357-361.
68. Jansen, I.; Peschar, R.; Schenk, H., On the determination of accurate intensities from powder diffraction data. *J. Appl. Cryst.* 1992, 25, 231-243.
69. Sheldrick, G.M., Phase annealing in SHELX-90- direct methods for larger structures. *Acta Cryst.* 1990, 46, 467-473.
70. Tremayne, M.; Karinki, B.M.; Hanis, K.D.M., The development of Monte Carlo methods for crystal structure solution from powder diffraction data: Simultaneous translation and rotation of a structural fragment within the unit cell. *J. Appl. Cryst.* 1996, 29, 211-214.
71. Solans, X., The limits to the determination of crystal structure from powder X-ray diffraction data. *Mat. Sci. Forum* 2001, 378-381, 80-85.
72. Harris, R.K., NMR crystallography: the use of chemical shifts. *Solid State Sci.* 2004, 6, 1025-1037.

73. Harris, R.K.; Joyce, S.A.; Pickard, C.J.; Cadars, S.; Emsley, L. NMR crystallography of oxybuprocaine hydrochloride, Modification II degrees. *Phys. Chem. Chem. Phys.* 2006, 8, 137-143.
74. Yates, J.R.; Dobbins, S.E.; Pickard, C.J.; Mauri, F.; Ghi, P.Y.; Harris, R.K., A combined first principles computational and solid-state NMR study of a molecular crystal: flurbiprofen *Phys. Chem. Chem. Phys.* 2005, 7, 1402-1407.
75. Gobetto, R.; Nervi, C.; Chierotti, M.R.; Braga, D.; Maini, L.; Grepioni, F.; Harris, R.K.; Hodgkinson, P., Hydrogen bonding and dynamic behaviour in crystals and polymorphs of dicarboxylic-diamine adducts: A comparison between NMR parameters and X-ray diffraction studies. *Chem. Eur. J.* 2005, 11, 7461-7471.
76. Harris, R.K.; Ghi, P.Y.; Hammond, R.B.; Ma, C.Y.; Roberts, K.J.; Yates, J.R.; Pickard, C.J., Solid-state NMR and computational studies of 4-methyl-2-nitroacetanilide. *Magn. Reson. Chem.* 2006, 44, 325-333.
77. Gervais, C.; Dupree, R.; Pike, K.J.; Bonhomme, C.; Profeta, M.; Pickard, C.J.; Mauri, F., Combined first-principles computational and experimental multinuclear solid-state NMR investigation of amino acids. *J. Phys. Chem. A.* 2005, 109, 6960-6969.
78. Gervais, C.; Profeta, M.; Lafond, V.; Bonhomme, C.; Azais, T.; Mutin, H.; Pickard, C.J.; Mauri, F.; Babonneau, F. Combined ab initio computational and experimental multinuclear solid-state magnetic resonance study of phenylphosphonic acid. *Magn. Reson. Chem.* 2004, 42, 445-452.
79. Hughes, C.E.; Olejniczak, S.; Helinski, J.; Ciesielski, W.; Repisky, M.; Andronesi, O.C.; Potrzebowski, M.J.; Baldus, M., Probing structure in the polymorphic domain of the L-enantiomer of N-benzoyl-phenylalanine by means of 2D solid-state NMR spectroscopy and DFT calculations. *J. Phys. Chem. B.* 2005, 109, 23175-23182.
80. Olsen, R.A.; Struppe, J.; Elliott, D.W.; Thomas, R.J.; Mueller, L.J., Through-bond C-13-C-13 correlation at the natural abundance level: Refining dynamic regions in the crystal structure of vitamin-D-3 with solid-state NMR. *J. Am. Chem. Soc.* 2003, 125, 11784-11785.
81. De Paepe, G.; Lesage, A.; Steuernagel, S.; Emsley, L., Transverse dephasing optimised NMR spectroscopy in solids: Natural-abundance C-13 correlation spectra. *ChemPhysChem.* 2004, 5, 869-875.
82. Brus, J.; Jegorov, A., Through-bonds and through-space solid-state NMR correlations at natural isotopic abundance: Signal assignment and structural study of simvastatin. *J. Phys. Chem. A.* 2004, 108, 3055-3964.
83. Twyman, J.M.; Fattah, J.; Dobson, C.M., Observation of discrete thiazolidine ring conformations in frozen aqueous solutions of penicillins by C-13 CP-MAS NMR-spectroscopy. *Chem. Commun.* 1991, 9, 647-649.

84. Gehman, J.D.; Paulson, E.K.; Zilm, K.W., The influence of internuclear spatial distribution and instrument noise on the precision of distances determined by solid state NMR of isotopically enriched proteins. *J. Biomol. NMR.* 2003, 27 (3), 235-259.
85. Seidel, K.; Etkorn, M.; Sonnenberg, L.; Griesinger, C.; Sebald, A.; Baldus, M., Studying molecular 3D structure and dynamics by high-resolution solid-state NMR: Application to l-tyrosine-ethylester. *J. Phys. Chem. A.* 2005, 109, 2436-2442.
86. Brown, S.P.; Schnell, I.; Brand, J.D.; Mullen, K.; Spiess, H.W., An investigation of pi-pi packing in a columnar hexabenzocoronene by fast magic-angle spinning and double-quantum H-1 solid-state NMR spectroscopy. *J. Am. Chem. Soc.* 1999, 121 (28), 6712-6718.
87. Brown, S.P.; Zhu, X.X.; Saalwachter, K.; Spiess, H.W., An investigation of the hydrogen-bonding structure in bilirubin by H-1 double-quantum magic-angle spinning solid-state NMR spectroscopy. *J. Am. Chem. Soc.* 2001, 123 (18), 4275-4285.
88. Bosman, L.; Madhu, P.K.; Vega, S.; Vinogradov, E., Improvement of homonuclear dipolar decoupling sequences in solid-state nuclear magnetic resonance utilising radiofrequency imperfections. *J. Magn. Reson.* 2004, 169 (1), 39-48.
89. Schnell, I.; Lupulescu, A.; Hafner, S.; Demco, D.E.; Spiess, H.W., Resolution enhancement in multiple-quantum MAS NMR spectroscopy. *J. Magn. Reson.* 1998, 133 (1), 61-69.
90. Hohwy, M.; Jakobsen, H.J.; Eden, M.; Levitt, M.H.; Nielsen, N.C., Broadband dipolar recoupling in the nuclear magnetic resonance of rotating solids: A compensated C7 pulse sequence. *J. Chem. Phys.* 1998, 108 (7), 2686-2694.
91. Geen, H.; Titman, J.J.; Gottwald, J.; Spiess, H.W., Spinning side-band in the fast-MAS multiple-quantum spectra of protons in solids. *J. Magn. Reson. A* 1995, 114 (2), 264- 267.
92. Sommer, W.; Gottwald, J.; Demco, D.E.; Spiess, H.W., Dipolar heteronuclear multiple-quantum NMR-spectroscopy in rotating solids. *J. Magn. Reson. A* 1995, 113 (1), 131-134.
93. Friedrich, U.; Schnell, I.; Brown, S.P.; Lupulescu, A.; Demco, D.E.; Spiess, H.W., Spinning-sideband patterns in multiple-quantum magic-angle spinning NMR spectroscopy. *Mol Phys* 1998, 95 (6), 1209-1227.
94. Schnell, I.; Spiess, H.W., High-resolution H-1 NMR spectroscopy in the solid state: Very fast sample rotation and multiple-quantum coherences. *J. Magn. Reson.* 2001, 151 (2), 153-227.
95. Mifsud, N.; Elena, B.; Pickard, C.J.; Lesage, A.; Emsley, L., Assigning powders to crystal structures by high-resolution  $^1\text{H}$ - $^1\text{H}$  double quantum and  $^1\text{H}$ - $^{13}\text{C}$  J-INEPT solid-state NMR spectroscopy and first principles computation. A case study of

penicillin G Direct spectral optimisation of proton-proton. *Phys. Chem. Chem. Phys.* 2006, 8 (29), 3418-3422.

96. Lesage, A.; Steuernagel, S.; Emsley, L., Carbon-13 spectral editing in solid-state NMR using heteronuclear scalar couplings. *J. Am. Chem. Soc.* 1998, 120 (28), 7095-7100.

97. Sakellariou, D.; Lesage, A.; Emsley, L., Spectral editing in solid-state NMR using scalar multiple quantum filters. *J. Magn. Reson.* 2001, 151 (1), 40-47.

98. Lesage, A.; Sakellariou, D.; Steuernagel, S.; Emsley, L., Carbon-proton chemical shift correlation in solid-state NMR by through-bond multiple-quantum spectroscopy. *J. Am. Chem. Soc.* 1998, 120 (50), 13194-13201.

99. Burum, D.P.; Ernst, R.R., Net polarization transfer via a J-ordered state for signal enhancement of low-sensitivity nuclei. *J. Magn. Reson.* 1980, 39 (1), 163-168.

100. Morris, G.A.; Freeman, R., Enhancement of nuclear magnetic-resonance signals by polarization transfer. *J. Am. Chem. Soc.* 1979, 101 (3), 760-762.

101. Sorensen, O.W.; Ernst, R.R., Elimination of spectral distortion in polarization transfer experiments - improvements and comparison of techniques. *J. Magn. Reson.* 1983, 51 (3), 477-489.

102. Gross J.D.; Costa P.R.; Dubacq J.P.; Warschawski D.E.; Lirsac P.N.; Devaux P.F.; Griffin R.G., Multidimensional NMR in lipid systems. Coherence transfer through J couplings under MAS. *Journal of Magnetic Resonance, Series B* 1995, 106 (2), 187- 190.

103. Soubias, O.; Reat, V.; Saurel, O.; Milon, A., High resolution 2D H-1-C-13 correlation of cholesterol in model membrane. *J. Magn. Reson.* 2002, 158 (1-2), 143-148.

104. Soubias, O.; Jolibois, F.; Reat, V.; Milon, A., Understanding sterol-membrane interactions, part ii: Complete H-1 and C-13 assignments by solid-state NMR spectroscopy and determination of the hydrogen-bonding partners of cholesterol in a lipid bilayer. *Chem.-Eur. J.* 2004, 10 (23), 6005-6014.

105. Alonso, B.; Massiot, D., Multi-scale NMR characterisation of mesostructured material using 1H->13C through-bond polarisation transfer, fast MAS, and 1H spin diffusion. *J. Magn. Reson.* 2003, 163 (2), 347-352.

106. Ashbrook, S.E.; Le Polles, L.; Pickard, C.J.; Berry, A.J.; Wimperis, S.; Farnan, I., First-principles calculations of solid-state O-17 and Si-29 NMR spectra of Mg<sub>2</sub>SiO<sub>4</sub> polymorphs. *Phys. Chem. Chem. Phys.* 2007, 9 (13), 1587-1598.

107. Mauri, F.; Pfrommer, B.G.; Louie, S.G., Ab initio theory of NMR chemical shifts in solids and liquids. *Phys. Rev. Lett.* 1996, 77 (26), 5300-5303.

108. Pickard, C.J.; Mauri, F., All-electron magnetic response with pseudopotentials: NMR chemical shifts. *Physical Review B*. 2001, 63, 6324.
109. Segall, M.D.; Lindan, P.J.D.; Probert, M.J.; Pickard, C.J.; Hasnip, P.J.; Clark, S.J.; Payne, M.C.J., First-principles simulation: ideas, illustrations and the CASTEP code. *Phys.-Condes. Matter*. 2002, 14 (11), 2717-2744.
110. Yates, J.R.; Pickard, C.J.; Payne, M.C.; Dupree, R.; Profeta, M.; Mauri, F.J., Theoretical investigation of oxygen-17 NMR shielding and electric field gradients in glutamic acid polymorphs. *Phys. Chem. A*. 2004, 108, (28), 6032-6037.
111. Yates, J.R.; Pham, T.N.; Pickard, C.J.; Mauri, F.; Amado, A.M.; Gil, A.M.; Brown, S.P., An investigation of weak CH center dot center dot center dot O hydrogen bonds in maltose anomers by a combination of calculation and experimental solid-state NMR spectroscopy. *J. Am. Chem. Soc.* 2005, 127 (29), 10216-10220.
112. Perdew, J.P.; Burke, K.; Ernzerhof, M., Generalized gradient approximation made simple. *Phys. Rev. Lett.* 1997, 78, 1396.
113. Vanderbilt, D., Soft self-consistent pseudopotentials in a generalized eigenvalue formalism. *Phys. Rev. B*. 1990, 41, 7892-7895.
114. Monkhorst, H.J.; Pack, J.D., Special points for brillouin-zone integrations. *Phys. Rev. B*. 1976, 13, 5188, 5192.
115. Yates, J.R., First principles calculation of nuclear magnetic resonance parameters. PhD Thesis at Cambridge University. 2003.
116. Dobson, C.M.; Ford, L.O.; Summers, S.E.; Williams, R.J.P., Nuclear magnetic resonance study of conformations of penicillins in solution using lanthanide ion probes. *J. Chem. Soc. Farad. Trans.* 1975, 71, 1145-1153.
117. Harris, R.K.; Ghi, P.Y.; Hammond, R.B.; MA, C.Y.; Roberts, K.J., Refinement of hydrogen atomic position in a hydrogen bond using a combination of solid-state NMR and computation. *Chem. Commun.* 2003, 22, 2834-2835.
118. Ochsenfeld, C.; Brown, S.P.; Schnell, I.; Gauss, J.; Spiess, H.W., Structure assignment in the solid state by the coupling of quantum chemical-calculations with NMR experiments: A columnar hexabenzocoronene derivative. *J. Am. Chem. Soc.* 2001, 123, 2597-2606.
119. Ochsenfeld, C.; Koziol, F.; Brown, S.P.; Schaller, T.; Seelbach, U.P.; Klarner, F.G., A study of a molecular tweezer host-guest system by a combination of quantum-chemical calculations and solid-state NMR experiments. *Solid State NMR*. 2002, 22, 128-153.
120. Brown, S.P.; Schaller, T.; Seelbach, U.P.; Koziol, F.; Ochsenfeld, C.; Klarner, F.G.; Spiess, H.W., Structure and dynamics of the host-guest complex of a molecular

tweezer: Coupling synthesis, solid-state NMR, and quantum-chemical calculations. *Angew. Chem.* 2001, 40, 717-720.

121. Caravatti, P.; Neuenschwander, P.; Ernst, R.R., Characterization of heterogeneous polymer blends by 2-dimensional proton spin diffusion spectroscopy. *Macromolecules* 1985, 18 (1), 119-122.

122. Zhang, S.; Meier, B.H.; Ernst, R.R., Polarization echoes in NMR. *Phys. Rev. Lett.* 1992, 69 (14), 2149-2151.

123. Meier, B.H., Polarization transfer and spin diffusion in solid-state NMR. *Adv. Magn. Opt. Reson.* 1994, 18, 1-116.

124. Demco, D.E.; Johansson, A.; Tegenfeldt, J., Proton spin-diffusion for spatial heterogeneity and morphology investigations of polymers. *Solid State Nuclear Magnetic Resonance* 1995, 4 (1), 13-38.

125. Schmidt-Rohr, K.; Spiess, H.W., *Multidimensional solid state NMR and polymers.* Academic Press: New York, 1994.

126. Campbell, G.C.; VanderHart, D.L., Optimization of chemical-shift-based polarization gradients in  $^1\text{H}$  NMR spin-diffusion experiments on polymer blends with chemically similar constituents. *J. Magn. Reson.* 1992, 96 (1), 69-93.

127. Brus, J.; Petrickova, H.; Dybal, J., Influence of local molecular motions on the determination of  $^1\text{H}$ - $^1\text{H}$  internuclear distances measured by 2D  $^1\text{H}$  spin-exchange experiments. *Solid State Nuclear Magnetic Resonance* 2003, 23 (4), 183-197.

128. Brus, J.; Petrickova, H.; Dybal, J., Potential and limitations of 2D H-1-H-1 spin-exchange CRAMPS experiments to characterize structures of organic solids. *Mon. Chem.* 2002, 133, (12), 1587-1612.

129. Abragam, A., *Principles of nuclear magnetism.* Oxford University Press: London, 1961.

130. Bloembergen, N., On the interaction of nuclear spins in a crystalline lattice. *Physica* 1949, 15 (3-4), 386-426.

131. Henrichs, P.M.; Linder, M.; Hewitt, J.M., Dynamics of the C-13 spin-exchange process in solids - a theoretical and experimental-study. *J. Chem. Phys.* 1986, 85 (12), 7077- 7086.

132. Kubo, A.; McDowell, C.A., P-31 spectral spin diffusion in crystalline solids. *J. Chem. Phys.* 1988, 89 (1), 63-70.

133. Kubo, A.; Mcdowell, C.A., Spectral spin diffusion in polycrystalline solids under magic-angle spinning. *J Chem Soc Farad T 1* 1988, 84, 3713-3730.

134. Sakellariou, D.; Hodgkinson, P.; Hediger, S.; Emsley, L., Experimental observation of periodic quasi-equilibria in solid-state NMR. *Chem. Phys. Lett.* 1999, 308 (5-6), 381- 389.
135. Hodgkinson, P.; Sakellariou, D.; Emsley, L., Simulation of extended periodic systems of nuclear spins. *Chem. Phys. Lett.* 2000, 326 (5-6), 515-522.
136. Zorin, V.E.; Brown, S.P.; Hodgkinson, P., Origins of linewidth in H-1 magic-angle spinning NMR. *J. Chem. Phys.* 2006, 125 (14), 144508.
137. Elena, B.; Emsley, L., Powder crystallography by proton solid-state NMR spectroscopy. *J. Am. Chem. Soc.* 2005, 127 (25), 9140-9146.
138. Abel, E.W.; Coston, T.P.J.; Orrell, K.G.; Sik, V.; Stephenson, D., Two-dimensional NMR exchange spectroscopy. Quantitative treatment of multisite exchanging systems. *J. Magn. Reson.* 1986, 70 (1), 34-53.
139. Perrin, C.L.; Dwyer, T.J., Application of 2-dimensional NMR to kinetics of chemical-exchange. *Chem. Rev.* 1990, 90 (6), 935-967.
140. Macura, S.; Ernst, R.R., Elucidation of cross relaxation in liquids by two-dimensional NMR-spectroscopy. *Mol Phys* 1980, 41 (1), 95-117.
141. Gorbitz, C.H., Crystal and molecular structures of the isomeric dipeptides alpha-l-aspartyl-l-alanine and beta-l-aspartyl-l-alanine. *Acta Chem Scand B.* 1987, 41 (9), 679-685.
142. Brünger, A.T; XPLOR Manual Version 3.1, Yale University Press, New Haven, 1993.
143. Brooks, B.R.; Brucoleri, R.E.; Olafson, B.D.; States, D.J.; Swaminathan, S.; Karplus, M., CHARMM- a program for macromolecular energy, minimization, and dynamics calculations. *J. Comput. Chem.* 1983, 4, 187-217.
144. Clore, G.M.; Gronenborn, A.M.; Brünger, A.T.; Karplus, M., The solution conformation of a heptadecapeptide comprising the DNA binding helix F of the cyclic AMP receptor protein of *Escherichia coli*: combined use of <sup>1</sup>H-nuclear magnetic resonance and restrained molecular dynamics. *J. Mol. Biol.* 1985, 186, 435-455.
145. Nilsson, L.; Clore, G.M.; Gronenborn, A.M.; Brünger, A.T.; Karplus, M., Structure refinement of oligonucleotides by molecular dynamics with NOE interproton distance restraints: application to 5'd(CGTACG)<sub>2</sub>. *J. Mol. Biol.* 1986, 188, 455-475.
146. Brünger, A.T.; Clore, G.M.; Gronenborn, A.M.; Karplus, M., Three-dimensional structures of proteins determined by molecular dynamics with interproton distance restraints; application to crambin. *Proc. Natl. Acad. Sci. USA.* 1986, 83, 3801-3805.
147. Clore, G.M.; Brünger, A.T.; Karplus, M.; Gronenborn, A.M., Application of molecular dynamics with interproton distance restraints to three-dimensional protein structure determination: a model study of crambin. *J. Mol. Biol.* 1986, 191, 523-551.

148. Clore, G.M.; Nilges, M.; Sukumaran, D.K.; Brünger, A.T.; Karplus, M.; Gronenborn, A.M., The three-dimensional structure of  $\alpha$ 1-purothionin in solution: combined use of nuclear magnetic resonance, distance geometry and restrained molecular dynamics. *EMBO J.* 1986, 5, 2729-2735.
149. Clore, G.M.; Sukumaran, D.K.; Nilges, M.; Gronenborn, A.M., The three-dimensional structure of phoratoxin in solution: combined use of nuclear magnetic resonance, distance geometry, and restrained molecular dynamics. *Biochemistry.* 1987, 26, 1732-1745.
150. Brünger, A.T.; Kuriyan, J.; Karplus, M., Crystallographic R-factor refinement by molecular dynamics. *Science.* 1987, 235, 458-460.
151. Brünger, A.T.; Adams, P.D.; Glore, G.M.; De Lano, W.L.; Gros, P.; Grosse-Kunstleve, R.W.; Jiang, J.S.; Kuszewski, J.; Nilges, M.; Pannu, N.S.; Read, R.J.; Rice, L.M.; Simonson, T.; Warren, G.L., Crystallography and NMR system: A new software suite for macromolecular structure determination. *Acta Cryst. Series D.* 1998, 54, 901-921.
152. Schwieters, C.D.; Clore, G.M., The VMD-XPLOR visualization package for NMR structure refinement. *J. Magn. Reson.* 2001, 149, 239-244.
153. Schwieters, C.D.; Kuszewski, J.J.; Tjandra, N.; Clore, G.M., The Xplor-NIH NMR molecular structure determination package. *J. Magn. Reson.* 2003, 160, 65-73.
154. Nilges, M.; Gronenborn, A.M.; Brünger, A.T.; Clore, G.M., Determination of three-dimensional structures of proteins by simulated annealing with interproton distance restraints; application to crambin, potato carboxypeptidase inhibitor, and barley serine proteinase inhibitor 2. *Protein Eng.* 1988, 2, 27-38.
155. Tjandra, N.; Omichinski, J.G.; Gronenborn, A.M.; Clore, G.M.; Bax, A., Use of dipolar  $^{15}\text{N}$ - $^1\text{H}$  and  $^{13}\text{C}$ - $^1\text{H}$  couplings in the structure determination of magnetically oriented macromolecules in solution. *Nat. Struct. Biol.* 1997, 4, 732-738.
156. Clore, G.M.; Gronenborn, A.M.; Tjandra, N., Direct refinement against residual dipolar couplings in the presence of rhombicity of unknown magnitude. *J. Magn. Reson.* 1998, 131, 159-162.
157. Tjandra, N.; Marquardt, J.; Clora, G.M., Direct refinement against proton-proton dipolar couplings in NMR structure determination of macromolecules. *J. Magn. Reson.* 2000, 142, 393-396.
158. Wu, Z.R.; Tjandra, N.; Bax, A.,  $^{31}\text{P}$  chemical shift anisotropy as an aid in determining nucleic acid structure in liquid crystals. *J. Am. Chem. Soc.* 2001, 123, 3617-3618.
159. Lipsitz, R.S.; Tjandra, N., Carbonyl CSA restraints from solution NMR for protein refinement. *J. Am. Chem. Soc.* 2001, 123, 11065-11066.

160. Tjandra, N.; Garrett, D.S.; Gronenborn, A.M.; Bax, A.; Clore, G.M., Defining long range order in NMR structure determination from the dependence of heteronuclear relaxation times on rotational diffusion anisotropy. *Nat. Struct. Biol.* 1997, 4, 443-449.
161. Clore, G.M.; Gronenborn, A.M.; Szabo, A.; Tjandra, N., Determining the magnitude of the fully asymmetric diffusion tensor from heteronuclear relaxation data in the absence of structural information. *J. Am. Chem. Soc.* 1998, 120, 4889-4890.
162. Nilges, M.; Clora, G.M.; Gronenborn, A.M., Determination of three-dimensional structures of proteins from interproton distance data by hybrid distance geometry-dynamical simulated annealing calculations. *FEBS Lett.* 1988, 229, 317-324.
163. Kuszewski, J.; Gronenborn, A.M.; Clore, G.M., Improving the quality of NMR and crystallographic protein structures by means of a conformational database potential derived from structure databases. *Protein Sci.* 1996, 5, 1067-1080.
164. Kuszewski, J.; Gronenborn, A.M.; Clore, G.M., Improving the packing and accuracy of NMR structures with a pseudopotential for the radius of gyration. *J. Am. Chem. Soc.* 1999, 121, 2337-2338.
165. Elena, B.; Pintacuda, G.; Mifsud, N.; Emsley, L., Molecular structure determination in powders by NMR crystallography from proton spin diffusion. *J. Am. Chem. Soc.* 2006, 128 (29), 9555-9560.

# Part B. Silicate Framework Materials

## B.1. Generalities on Disordered Solids

### B.1.1. Introduction

Order and disorder can be seen as an exchange process controlled by entropic energy. Indeed, all things in the world are either ordered or disordered. In solid-state chemistry, systems that have some extent of order often have well defined macroscopic and/or microscopic properties in particular. However, a wide range of solid systems are generally considered as disordered, meaning in this case free of any order, from the molecular to the micrometric length scale. Such systems include in particular glasses, which have (among others) specific temperature-dependent behavior at different length and time scales, and are extensively studied for applications in materials science<sup>1</sup>, but also in geology. Ceramics, also of crucial importance for material science, are used in particular for their highly stable macroscopic behavior with respect to extreme conditions of temperature and pressure, and to particular electronic and conduction properties, and are therefore represent high performance constituents in the area of advanced technologies<sup>2</sup>. Ceramics generally present a certain degree of molecular level order, and their properties strongly depend on order/disorder at this length scale.

In the same way, polymers exhibit a wide range of mechanical properties in particular, since they include soft materials such as elastomers, or more rigid plastics for example<sup>3, 4</sup>. Such systems are often made up of completely amorphous and more ordered domains referred to as lamellae, where the chains adopt parallel arrangements. However, contrarily to ceramics, these materials have macroscopic properties that are extremely dependent on temperature, owing to important molecular-scale dynamics, which include chain reptation and/or conformational changes<sup>5</sup>. Moreover, polymers play crucial roles in biology as they form cellular membranes, and constitute a large part of the architecture of bones, for instance. Other biological macromolecules, such as proteins, generally contain unfolded, and thus disordered, highly mobile domains involved in molecular recognition, ligand binding and translocation, and therefore play a crucial role in the activity of these systems.

As seen in these few examples, it is clear that order and disorder are often found together, and their respective weight at different length scales often determines the macroscopic properties of a solid. However, it is not always easy to distinguish between order and disorder, and the point of view of specialists of different measurement methods is often different. For diffusion/diffraction methods, the distinction between order and disorder first lies in the existence of a spatial periodicity, resulting in peaks in a diffusion or diffraction diagram. Thus, in the diffraction diagram, longer spatial range of this periodical order corresponds to narrower peaks. This periodicity may be of several origins, ranging from the hexagonal arrangement of the several-nanometer-diameter cylindrical holes in mesoporous materials (showing no order at the molecular scale), to the well defined atomic positions (within fractions of Angstroms) in pure molecular crystals. However,

we shall see in the following that solid-state nuclear magnetic resonance (NMR) is able to show the existence of a certain degree of order that cannot be seen from diffusion or diffraction, either because the spatial range of this order is too short or because it is not a three-dimensional order. As a consequence, the notion of order is not restricted to what is visible or not in X-ray studies. However, perfect order does not exist, and even highly crystalline species have internal degrees of freedom that allow thermal fluctuations (vibrations in particular), but also static distortions such as the presence of local defaults in the crystal, which are stabilized by the interaction with the environment.

Another important question, which is also related to the coexistence of order and disorder, and which already appeared in the general considerations above is the determination of the spatial range of a certain order. For example a given nucleus in a glass can be found in a local environment, corresponding to its first or second coordination sphere, which has a quite well defined geometry, but whose orientation with respect to the local environment of the nearest atom of the same type may differ significantly. As a result, it is important to probe the existence of a certain correlation between the environments of two nuclei that are at a given distance from each other.

## **B.1.2. Order / Disorder in NMR**

### **B.1.2.1. Review**

In the case of disordered solids, the situation described above is ever more complicated to study by solid-state NMR because in such systems, a given atom in a

molecule will find itself in slightly different structural environments in going from one molecule (or subunit) to another. This leads to a corresponding variation in isotropic chemical shift from one molecule to another, resulting in an inhomogeneous broadening of the NMR resonance. A similar broadening can arise from differences in magnetic susceptibility in different parts of the sample. Indeed, even under fast MAS and strong heteronuclear decoupling conditions, disordered solids often yield  $^{13}\text{C}$  linewidths of several ppm. However, this broadening is not always a disadvantage, as many authors have shown in the past that the chemical shift distribution can in favorable cases be interpreted in terms of structure.

In the early nineties, Schmidt-Rohr and Spiess have made particular advances in multi-dimensional NMR of disordered solids focusing more specifically on polymers<sup>6</sup>. They have demonstrated that solid-state NMR was able to provide crucial information on structure and dynamics of such systems, by means of sophisticated pulsed NMR techniques. The characterization of dynamics in a wide range of biological or synthesis polymers through solid-state NMR exchange techniques in particular, is still an active field of research nowadays<sup>7</sup>. Similarly in glasses, dynamics is very important and have also been extensively studied by NMR. In such systems, the presence of quadrupolar nuclei has been used to establish structural features in these challenging solids, which are barely accessible to any other experimental technique. Important advances in this field have been reported by Stebbins *et al.*<sup>8</sup>, Grandinetti *et al.*<sup>9, 10</sup>, in particular, which have notably involved the use of angular dependences of the quadrupolar interaction, the identification of different coordinating species, and the quantification of the level of disorder. Finally, the use of  $J$  couplings has also recently become of importance in solid-state NMR of glasses, as they enable to establish non-ambiguous connectivities in these materials<sup>11, 12</sup>.

Interestingly, it has been shown that such through-bond connectivities can involve quadrupolar nuclei of spin  $(2n+1)/2$ , such as  $^{27}\text{Al}$ , which opens new possibilities in the identification of the coordination spheres of different nuclei in this class of materials<sup>13</sup>.

Here, we focus more specifically on high resolution NMR of nuclear spins 1/2, and in particular  $^{29}\text{Si}$ . The consequence of spectral broadening is indeed that resonances corresponding to different chemical sites are often overlapped, preventing characterization. However, it has been shown that this limitation can be overcome by recording pair-wise correlation spectra<sup>14</sup>. Indeed, since the chemical shift variations induced by disorder are often correlated between neighboring sites, 2D correlation spectra may yield peaks that can have a much higher resolution than the 1D spectrum. This correlation effect is widespread, and is likely to be observed in some glassy<sup>15</sup>, polymer<sup>16</sup>, or layered silicate samples for example<sup>17</sup>. As a result, the techniques developed for high resolution NMR of polycrystalline samples may be of crucial importance in multi-dimensional NMR of disordered solids.

An excellent illustration of this idea is given in figure B.1 by the comparison of two 2D spectra reported in the literature from the same sample of 11%  $^{13}\text{C}$ -enriched cellulose extracted from wood, one in 1999<sup>18</sup> (figure B.1a) and the second in 2003<sup>14</sup> (figure B.1b).

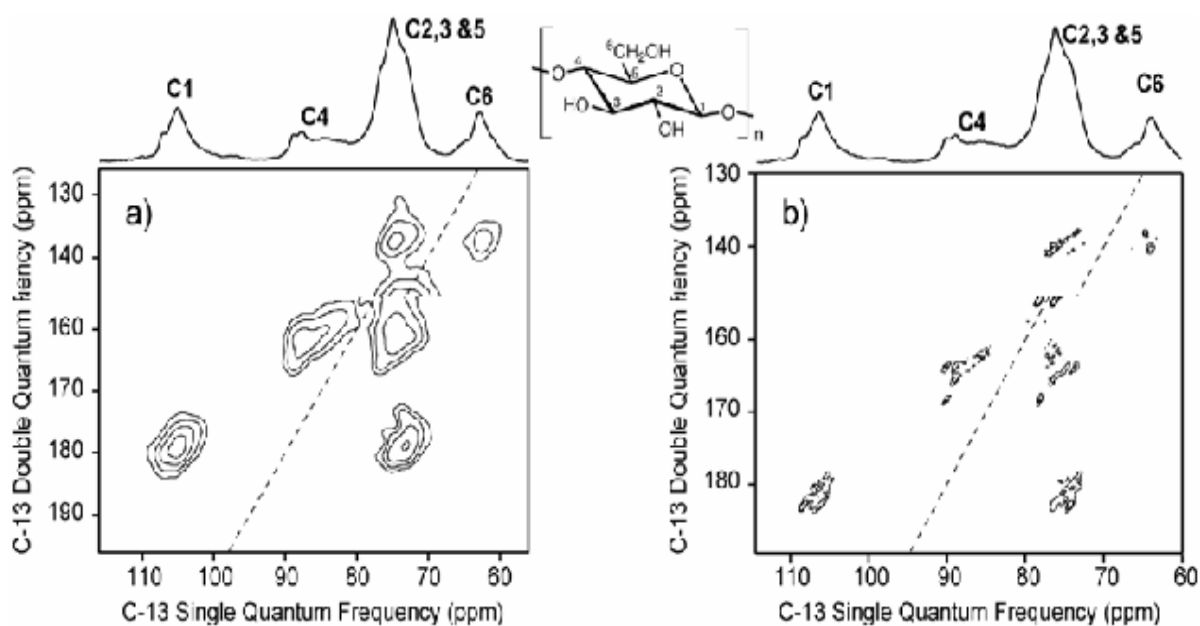


**Figure B.1.** Comparison of two refocused INADEQUATE<sup>18</sup> spectra obtained on the same sample, using the same experimental technique, and published in an interval of four years. (a) Spectrum reported in reference 18 (1999), acquired on a 7 mm probehead at 6 kHz MAS using CW decoupling at the proton nutation frequency of 100 kHz. (b) Spectrum reported in reference 14 (2003), obtained on a 4 mm probe at the spinning frequency of 10 kHz, under TPPM decoupling at the rf irradiation power of 100 kHz. The differences essentially arise from heteronuclear decoupling and MAS conditions, and illustrate the importance of high resolution techniques in disordered solids. See references 14 and 18 for further experimental details.

As solid-state NMR is sometimes not only sufficient to characterize this kind of solids, there are complementary techniques that can be used.

First of all, X-ray and neutron diffraction analysis often provide well defined atomic positions (sometimes to fractions of Angstroms), and unit cell parameters ( $a$ ,  $b$ ,  $c$  dimensions and  $\alpha$ ,  $\beta$ ,  $\gamma$  angles) are generally easily obtained with great precision through these techniques. The range of samples that can be characterized is relatively broad, though single crystals are by far the most appropriate samples for a

fine and accurate characterization. However, it has been shown that X-ray or neutron diffraction can provide deep insights on more complicated systems such as cellulose microfibrils for example<sup>19</sup>. In most cases, diffraction results are used in combination with molecular modeling, which integrates the diffraction data as targets for the structural determination in particular for the characterization of crystallized proteins in structural biology. NMR on the other hand gives in most cases only indirect information on the crystallographic arrangement of the molecules in a unit cell (although important articles have recently shown that crystallographic positions can in some cases be fully determined by solid-state NMR<sup>20-22</sup>). Therefore, diffusion and diffraction results often provide extremely useful reference structures that can be used for the fine interpretation of the NMR results. In the characterization of disordered solids, although structural disorder is by definition not accessible to diffusion or diffraction, meaningful average and/or potentially stable structures can be obtained from X-ray diffraction studies on model crystalline systems, which may be of great importance for studying the slight structural deviations that are in many cases responsible for the structural disorder.

Similarly, a powerful method for the characterization of these solids is scanning electron microscopy (SEM). Indeed, nowadays, this technique is able to provide wonderful images with a resolution down to a few nanometers, and is extremely widespread in materials science in particular. Moreover, SEM does not need any order and the structural information obtained is independent of the chemical composition of the sample. With the introduction of environmental scanning electron microscopy, the constraints imposed by the need for the sample to be observed in vacuum progressively vanish, and the potential of this technique is in clear progress. SEM is of crucial importance in particular to understand the

mesoscopic organization of a solid from the nanometric to the micrometric length scale. Such information may be determinant for the interpretation of the NMR data in terms of ordered and disordered domains, for example, as this technique can reveal the presence of mesoscopic defects that can result in molecular-level disorder.

Finally, most NMR spectroscopy today uses computational approaches to predict the NMR results on the basis of model numerical systems. These approaches first include numerical simulations of spin dynamics, which enable to predict the behavior of given spin system during the pulse sequence, and thus to probe for example the robustness of new experimental approaches with respect different phenomena<sup>23-25</sup>. In addition, computational approaches play key roles in structural determination from NMR. Indeed, NMR data (such as space proximities or chemical shifts) can be integrated in molecular modeling codes as constraints for the structural determination of soluble proteins. Finally, the prediction of NMR parameters, such as chemical shifts or *J*-couplings, from a given structure has played an increasingly important role in the past fifteen years, with the fast developments of semi-empirical, *ab initio* and first principles methods (DFT) and computational resources as seen in part A.

### **B.1.2.2. Order / Disorder in surfactant-templated layered silicates**

In this chapter, we will contribute to this area through study the order and disorder of surfactant-templated layered silicates. Indeed, mesostructured and mesoporous inorganic solids have specific properties that make them particularly attractive for a wide range of potential applications in catalysis or opto-electronics. These solids have fundamental dependencies on local order or disorder, often

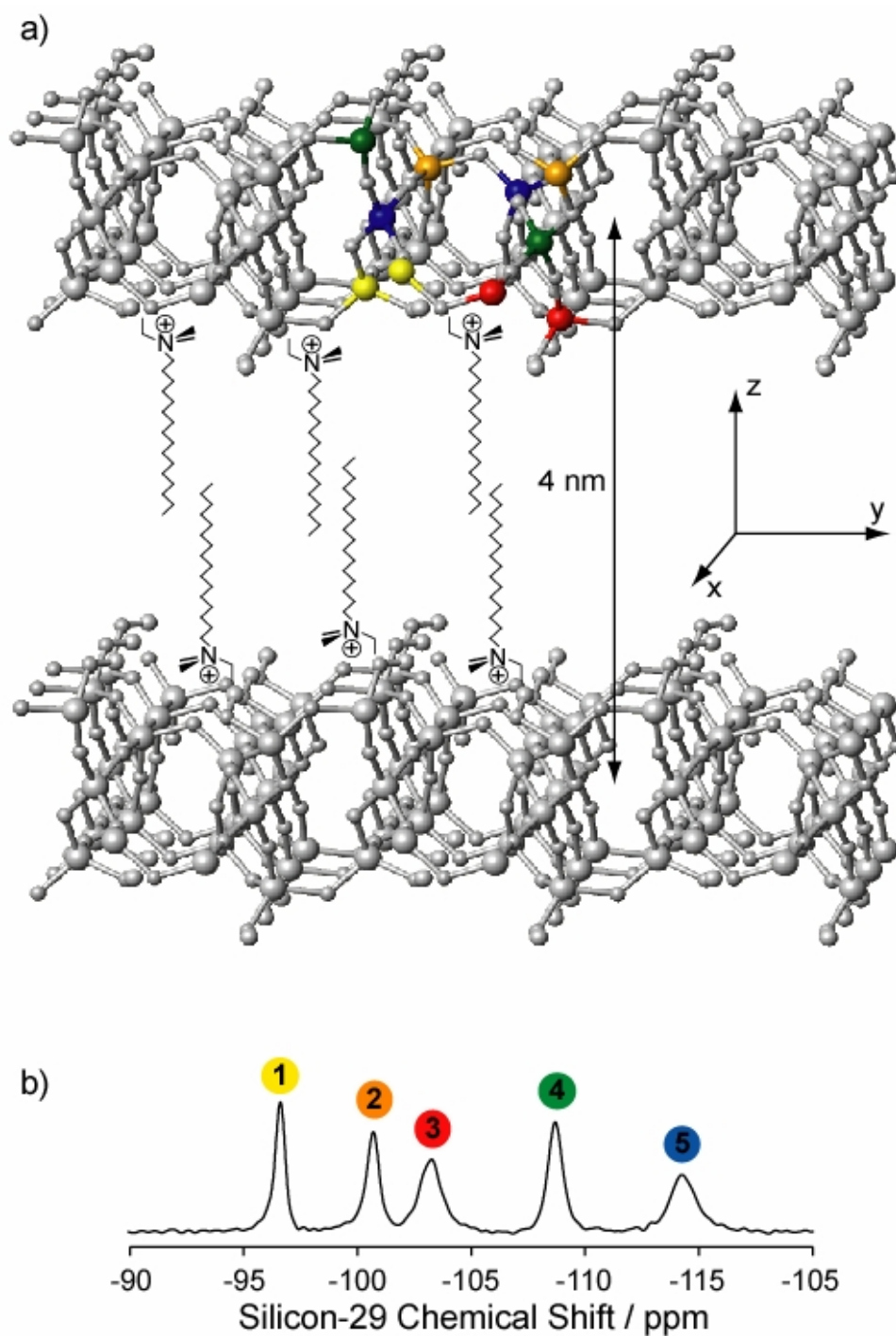
combined with strong variations in composition, structure, and dynamics across different length scales, which often tune their chemical and physical properties, as well as their macroscopic process or device performance. And solid-state NMR plays a crucial role in the characterization of these materials at the molecular scale, complementing other methods, such as X-ray diffraction, electron microscopy, and bulk methods<sup>26</sup>.

Recently, surfactant-templated layered silicates with a high degree of short-range order have been synthesized and characterized<sup>17, 27</sup>. However, despite the molecular-level order, two-dimensional (2D) <sup>29</sup>Si NMR experiments<sup>17</sup> carried out on such layered materials have revealed that their resonances are inhomogeneously broadened due to the presence of a slight structural disorder.

High-resolution transmission electron micrographs show the lamellar arrangement of the material, with 1 nm thick layers spaced by 3 to 4 nanometers. This mesoscopic order is in agreement with X-ray diffraction diagrams<sup>27</sup> providing a quantitative measurement of the distance between two layers.

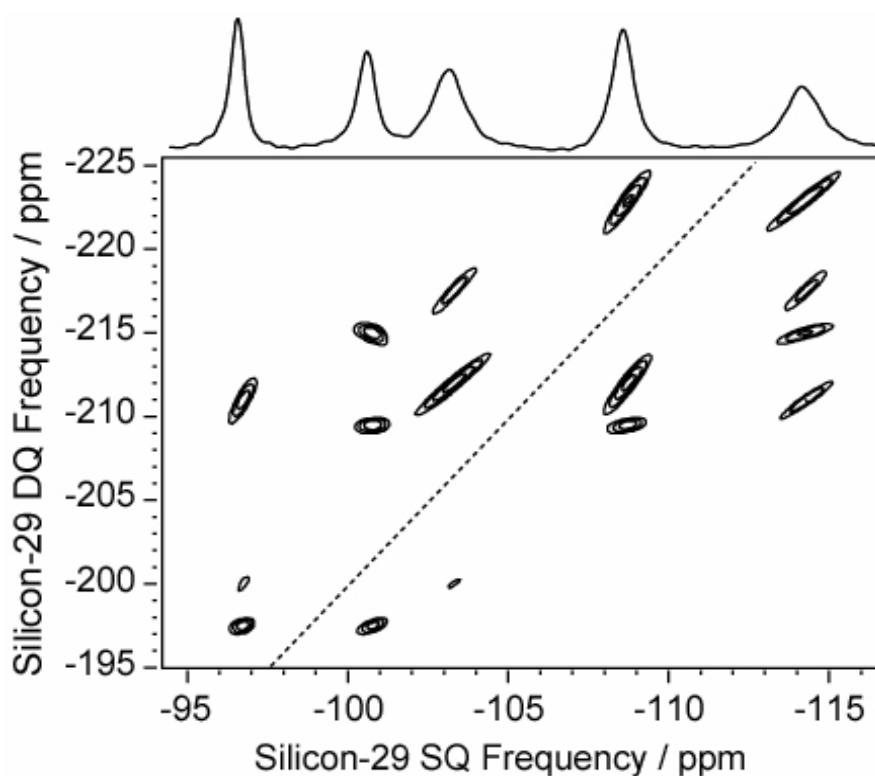
However, TEM images show a curvature of the layers on the length scale of tens of nanometers, which is in part responsible for the lack of long-range crystallinity. Second, on a molecular level, the material considered here is ordered, as revealed by XRD patterns<sup>17, 27</sup>. This molecular-level structure has been determined by combined solid-state NMR, X-ray diffraction and quantum mechanics studies<sup>17</sup>.

Figure B.2a shows a representation of the silicate layers, with the five crystallographically distinct tetrahedrally coordinated silicon atoms indicated as colored spheres, whose corresponding resonances are well-resolved in the <sup>29</sup>Si CP-MAS NMR spectrum shown in figure B.2b, confirming the molecular-level order.



**Figure B.2.** (a) Illustration of the silicate layers and templating  $\text{CH}_3(\text{CH}_2)_{15}\text{-NMe}_2\text{Et}^+$  surfactant molecules. The structure of the silicate layers and color code for labeling different  $^{29}\text{Si}$  sites is as proposed in reference 17. (b)  $^{29}\text{Si}$  CPMAS spectrum of the surfactant-templated silicate layers recorded at 298 K, which shows the five equally populated crystallographically distinct sites.

Two-dimensional  $^{29}\text{Si}$  double quantum (DQ) NMR spectrum of these materials<sup>17</sup> (figure B.3) shows a wide range of elongated 2D lineshapes that are characteristic of inhomogeneous distributions of isotropic chemical shifts arising from correlated disorder. This disorder can have different origins, including dispersion in the arrangement of the surfactant headgroups with respect to the silicate layers or slight deviations of the atomic positions in the silicate layers around the average geometry. One of the purposes of the next sections is to discriminate between the potential sources of inhomogeneous broadening.



**Figure B.3.** Refocused INADEQUATE spectrum recorded at a temperature of 298 K, spinning the sample at 10 kHz.

## B.1.3. Through Bond Spectroscopy – INADEQUATE

### B.1.3.1. Introduction

Through-bond connectivities, in particular in disordered solids, are of even further interest compared to liquid-state NMR, since in addition to the ambiguities arising from intra-molecular spatial proximities, the absence of Brownian molecular motion results in non-averaged inter-molecular interactions. Such inter-molecular proximities may lead to difficulties in the assignment, which is the prerequisite step in any deeper structural NMR analysis. On the other hand, in solid-state NMR, through-space methods using the often large dipolar interactions that are generally present in solids under magic angle spinning (MAS) have been much more widespread than through-bond methods. Indeed,  $J$  couplings are often not resolved in solid-state NMR, and have thus not immediately appeared as an attractive way to achieve magnetization transfer in solids.

Pioneering implementations of liquid-state methods providing  $J$ -mediated transfer have nevertheless been reported since the early 1980's in mobile solids, such as plastic crystals<sup>28-31</sup>, having sufficiently narrow lines for the  $J$  couplings to be resolved. Then, in the late 80's, a few groups have demonstrated that COSY and INADEQUATE (Incredible Natural Abundance Double QUAntum Transfer Experiment)-type experiments, combined with cross polarization (CP)<sup>32</sup>, could be used in rigid inorganic solids, first on model systems<sup>33</sup>, and then on <sup>29</sup>Si-enriched and natural abundance zeolites<sup>34-36</sup> and silicate glasses<sup>37</sup>. Complete connectivity patterns between the different sites were thus obtained, which in the case of zeolites enabled

the identification among the possible 3D structures. Only in the late 90's robust homonuclear through-bond correlation techniques have been started to develop for organic solids as well. A quite recent review of through-bond methods, which essentially focuses on organic solids, is available in the literature<sup>38</sup>.

As mentioned above, through-bond homonuclear correlation techniques have undergone fast methodological development for about a decade, making them suitable for measuring  $J$ -mediated correlations in an extremely wide range of solids, and MAS conditions. In this subsection we will focus specially on the INADEQUATE technique which is now routinely used in the solid-state NMR community. The major disadvantages and advantages of this sequence towards other techniques are pointed out.

The INADEQUATE experiment<sup>39</sup> was successfully applied to rigid organic solids under MAS by Lesage and co-workers<sup>40</sup>. It enabled to observe carbon-carbon through-bond correlations in powdered samples of fully  $^{13}\text{C}$ -enriched and *natural abundance* amino-acids. Contrarily to the TOBSY-like sequences, the INADEQUATE experiment only yields correlation peaks between  $J$ -coupled sites, thus enabling sequential assignment, which is of particular interest in molecules having large spin-systems. The principle of this very simple experiment is to create anti-phase coherences on  $^{13}\text{C}$  nuclei through evolution under the  $J$  couplings during a coherence-transfer echo<sup>41</sup> subsequent to the CP, and then to convert these coherences to double quantum (DQ) coherences between  $J$ -coupled spins by applying a  $90^\circ$  pulse. DQ coherences then evolve during the indirect evolution period, and are converted back to anti-phase coherences for detection under heteronuclear decoupling. As mentioned by the authors, potential improved sensitivity was

expected from improved MAS and heteronuclear decoupling conditions. However, this experiment is not well adapted for the case of disordered solids because of the cancellation of the two transitions of the  $J$  doublet that would occur for line widths strongly exceeding the magnitude  $J$  coupling.

In 1999, Verel and co-workers<sup>42</sup> adapted the INADEQUATE-CR (Composite Refocusing) experiment<sup>43</sup> to powdered solids under MAS, thus benefiting from improved resolution in the case of isolated spin-pairs from the concentration of the intensity in only one transition of the  $J$ -split doublet (in the direct dimension). This experiment enabled in particular to observe through-bond correlations between  $^{13}\text{CH}_2$  and  $^{13}\text{CO}$  nuclei of fully  $^{13}\text{C}$ -enriched glycine inserted in a heterogeneous material with inhomogeneous broad lines (arising in that particular case essentially from bulk magnetic susceptibility). However, this sequence has not been implemented as a 2D experiment (to our knowledge), essentially because the simpler and yet efficient refocused INADEQUATE experiment was introduced the same year<sup>18</sup>, and its robustness when applied to disordered solids simultaneously demonstrated. Indeed, the gain in resolution provided by the INADEQUATE-CR through the removal of the  $J$  splitting has so far not been an issue in the broad spectra of disordered solids. In addition the two spin-echoes  $\tau$ - $\pi$ - $\tau$  (of duration  $2\tau = 1/(2J)$ ) of the refocused INADEQUATE sequence lead to reduced signal loss by transverse dephasing compared to the INADEQUATE-CR, made up of three spin-echoes.

In 2002, Mueller *et al.* introduced another method for detecting homonuclear through-bond correlations on the basis of coherence transfer echoes: the uniform sign double-quantum filtered COSY (UC2QF COSY) experiment<sup>44</sup> which yields in-phase cross peaks, and is thus suitable for the case of disordered solids. The advantage of this method compared to the refocused INADEQUATE experiment was,

according to the authors, the simpler SQ-SQ spectrum obtained (though in fact DQ-SQ spectra can be easily transformed into SQ-SQ spectra free of any diagonal peaks, as has since been demonstrated in the literature<sup>45, 46</sup>), and we additionally note that they used a z-filter without heteronuclear decoupling before detection, in order to “guarantee in-phase absorptive lines for multi-spin systems”. The UC2QF COSY experiment was successfully applied to a challenging system of 10% <sup>13</sup>C-enriched HC<sub>60</sub><sup>+</sup>, in which the existence of a covalent bond between the protonated sp<sup>3</sup> and the sp<sup>2</sup> hybridized cationic sites was demonstrated. Interestingly, a natural abundance <sup>13</sup>C-<sup>13</sup>C spectrum of micro-crystalline vitamin D<sub>3</sub> was obtained with this experiment<sup>47</sup> from which the 54 peaks in the spectrum were assigned, thus extending the feasibility of through-bond experiments in natural abundance to medium-sized systems. This experiment turns out to be very similar in potential applications and performance to the refocused INADEQUATE experiment. An important advantage of both experiments of the DQ-filtered COSY and INADEQUATE families is their *extreme simplicity compared to symmetry-based methods*.

Finally, Fayon *et al.* have very recently proposed a *J*-mediated triple-quantum (TQ) experiment<sup>48</sup> which provides connectivities between spin triplets, and thus increasing the level of information obtained from *J*-mediated experiments in enriched solids (or abundant spins, such as <sup>31</sup>P). Though experimental efficiency is still far below the theoretical limit, the method was applied to phosphate glasses, where the obtained TQ-SQ correlation spectra provide an improved description of the glass network connectivities and of the chain length distribution in the disordered network. Moreover, Duma *et al.*<sup>49</sup> have recently introduced homonuclear spin-state-selective spin-diffusion spectra by adapting the in-phase-anti-phase (IPAP) experiment to solids under MAS. Though not providing through-bond correlation spectra, this

experiment uses  $J$ -coupling evolutions to achieve spin-state selection. The IPAP experiment significantly improves the resolution in 2D spectra of fully isotopically-enriched solids, by selectively detecting a given transition among the generally unresolved fine structure of the 2D-cross peaks. After its successful application to micro-crystalline proteins<sup>50</sup>, this experiment was implemented in liquid-state NMR<sup>51</sup>.

The refocused INADEQUATE experiment was rapidly applied with success to a wide range of isotopically enriched<sup>14, 17, 52-56</sup> and natural abundance samples<sup>12, 46, 57-59</sup>. It was applied to <sup>13</sup>C-enriched microcrystalline proteins<sup>54</sup> or natural abundance crystalline solids, from which <sup>13</sup>C refocused INADEQUATE spectra were obtained within a few days<sup>57-59</sup>.

### **B.1.3.2. The refocused INADEQUATE experiment**

The pulse sequence of the refocused INADEQUATE experiment is shown in figure B.4a, together with the corresponding coherence transfer pathway<sup>60</sup> (selected through phase cycling). After cross polarization (CP) from protons to the  $X$  spins, a first spin-echo generates anti-phase coherences through  $J$ -coupling evolution, with best theoretical efficiency for a spin-echo delay  $\tau=1/(4J)$ . These anti-phase coherences are then converted to double-quantum (DQ) coherences between  $J$ -coupled nuclei by the  $90^\circ$  pulse. These DQ coherences evolve during the indirect evolution period, and are then converted back to anti-phase coherences, which are finally transformed to in-phase coherence by the second spin echo for detection. Zero-quantum (ZQ) coherences in  $t_1$  are removed by appropriate phase cycling of the first  $90^\circ$  pulse (and the first  $180^\circ$  pulse), which yields a loss in efficiency of 50%.

When applied to an isolated  $J$ -coupled spin pair, the refocused INADEQUATE experiment yields a pair of correlation peaks at the same DQ frequency in the indirect dimension, being the sum of their individual frequencies.

Figure B.4b shows the expected positions of the correlation peaks for a system made up of a weakly coupled linear spin system  $A$ - $B$ - $C$ , where  $J_{AB} \neq 0$  Hz,  $J_{BC} \neq 0$  Hz, and  $J_{AC} = 0$  Hz, with the enrichment level being low enough for three-spin effects to be negligible (the ca. 4% natural abundance of  $^{29}\text{Si}$  is a good example). The pulse sequence strictly restricts coherence transfer to between  $J$ -coupled spins, and no diagonal peak is in principle expected in such experiment (equivalent nuclei having in principle a zero  $J$  coupling).

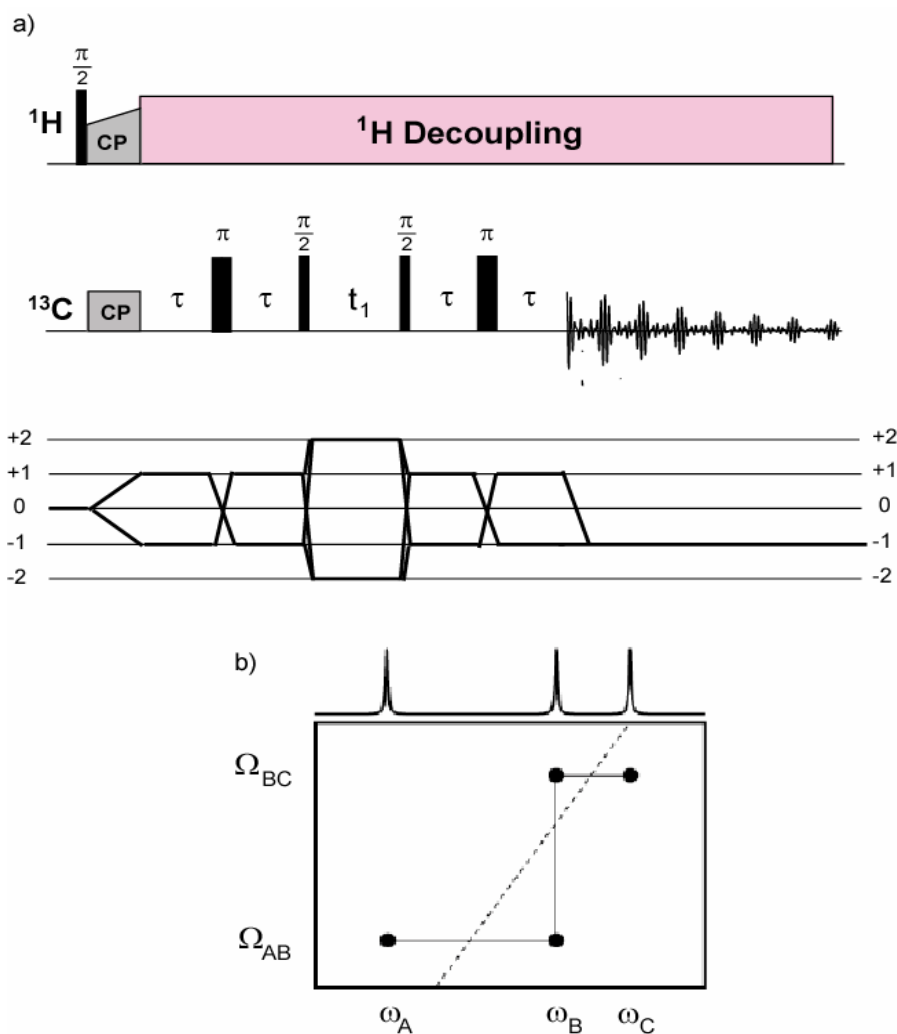


**Figure B.4.** (a) Pulse sequence and coherence-transfer pathway<sup>60</sup> of the refocused INADEQUATE experiment, which provides homonuclear through-bond correlation spectra in solids, as proposed by Lesage and co-workers<sup>13</sup>. (b) Expected positions of the correlation peaks for a linear (weakly coupled) spin system A-B-C. The enrichment level is supposed low enough for 3-spin effects to be negligible.

In this part, we will focus on two distinct samples which have been synthesized in the group of Prof. Chmelka (Santa Barbara) and which differ in composition by the nature of the surfactant headgroup. A picture of the silicate layers, is shown in figure B.5a, together with a (z-filtered) refocused INADEQUATE spectrum (figure B.5b) of

the silicate layers templated by  $\text{CH}_3(\text{CH}_2)_{15}\text{-NMe}_2\text{Et}^+$ , on which we will specially focus. Such materials (of high technological interest) have been studied as probes of organic-inorganic interactions at the molecular level that play a crucial role in the self-assembling process. Since they lack long-range 3D crystallinity, full characterization of the locally ordered silicate structure is only possible on the basis of solid-state NMR. The identification of the connectivity patterns using the refocused INADEQUATE experiment has been determinant to that end.

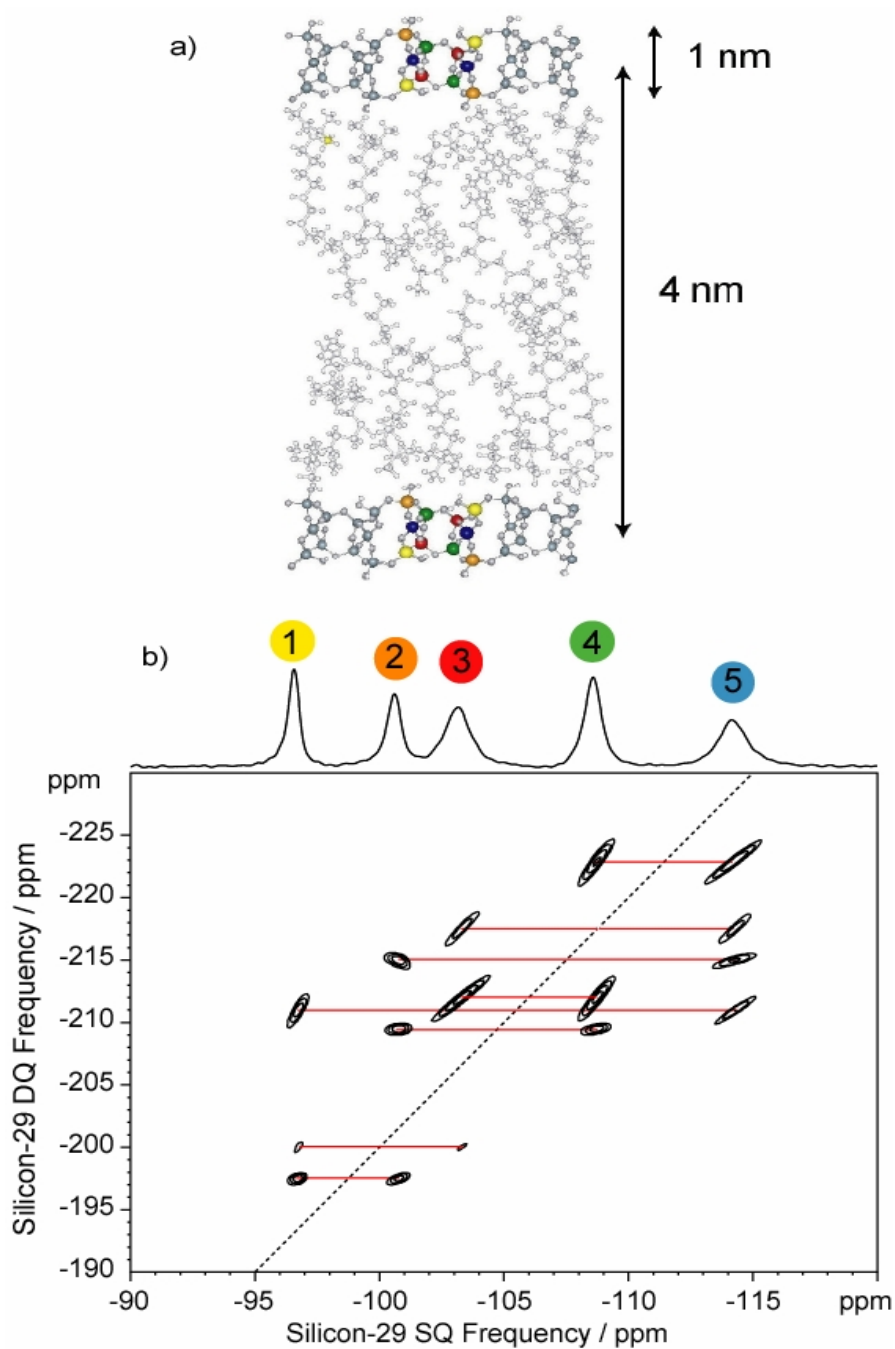


**Figure B.5.** (a) Schematic structure of two silicate layers templated by a  $\text{CH}_3(\text{CH}_2)_{15}\text{-NMe}_2\text{Et}^+$ -surfactant, and viewed parallel to the layers, which are separated by the alkyl chains of the cationic surfactant species. (Adapted from Hedin *et al.*<sup>17</sup>) We used the same  $^{29}\text{Si}$  site color code to describe the structure of the surfactant templated silicate sample under investigation in this part. (b) Silicon-29  $z$ -filtered refocused INADEQUATE spectrum of the  $\text{CH}_3(\text{CH}_2)_{15}\text{-NMe}_2\text{Et}^+$ -templated silicate layers at 298 K.

The other sample is the silicate layers templated by  $\text{CH}_3(\text{CH}_2)_{15}\text{-NMeEt}_2^+$ . The  $z$ -filtered  $^{29}\text{Si}$  refocused INADEQUATE spectrum of this second material is shown in figure B.6. A close examination of the lineshapes obtained in this spectrum and in the INADEQUATE spectrum of figure B.5b (or from DQ through-space experiments in references 17 and 27) clearly show a wide range of inhomogeneously elongated lineshapes that are characteristic of some extent of short-range subtle disorder in the silicate layers. The nature of this disorder is being investigated, and the results would be reported in the next sections.

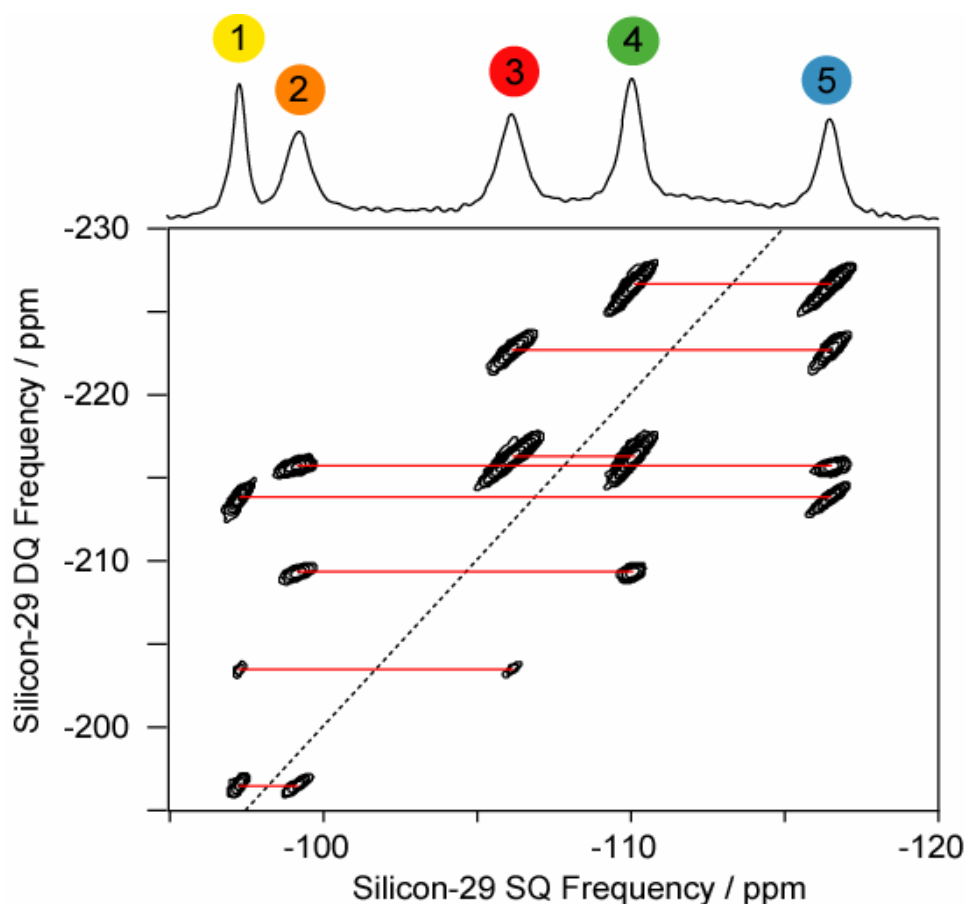


**Figure B.6.** Silicon-29  $z$ -filtered refocused INADEQUATE spectrum of the  $\text{CH}_3(\text{CH}_2)_{15}\text{-NMeEt}_2^+$ -templated silicate layers at 298 K.

In such systems, measurement of the  ${}^2J({}^{29}\text{Si}-\text{O}-{}^{29}\text{Si})$  couplings is of particular interest, since they are directly related to the geometry of the siloxane linkages. The five well-resolved resonances observed in the  ${}^{29}\text{Si}$  CP-MAS spectrum (1D spectrum on top of the INADEQUATE experiment in figure B.6) are consistent with the five distinct, equally populated  ${}^{29}\text{Si}$  sites in these materials<sup>27</sup>. The peaks at -97.3 and -99.3 ppm, labeled sites 1 and 2, respectively, correspond to  $Q^3$   ${}^{29}\text{Si}$  sites, whereas the peaks at -106.1, -110.0, and -116.5 ppm (sites 3, 4, and 5, respectively) correspond to fully condensed tetrahedrally coordinated  $Q^4$   ${}^{29}\text{Si}$  sites (where  $Q^N$  refers to a Si atom linked to  $N$  other Si atoms through siloxane bridges.) The z-filtered refocused  ${}^{29}\text{Si}$  INADEQUATE spectrum (figure B.6) of the material under consideration establishes that the interconnectivities among the five distinct  ${}^{29}\text{Si}$  sites are the same as reported for the  $\text{C}_{16}\text{Me}_2\text{EtN}^+$ -surfactant-templated material described in reference 17: site 1 is linked to sites 2, 3 and 5; site 2 is linked to sites 1, 4 and 5; site 3 to two different site-4 nuclei, and once each to sites 1 and 5; site 4 is linked to two different site-3 nuclei and once each to sites 2 and 5, and finally, site 5 is connected to sites 1, 2, 3 and 4.

All of these tetrahedral  ${}^{29}\text{Si}$  site connectivities are summarized schematically in figure B.8a, where the grey lines correspond to siloxane bridges (and to silanol groups for the  $Q^3$  moieties). The structural analyses of such complicated hierarchically ordered solids have relied on small-angle X-ray scattering to establish the ca. 4-nm spacing between adjacent silicate sheets and a combination of 2D double-quantum  ${}^{29}\text{Si}$  MAS NMR, wide-angle X-ray scattering, and quantum chemistry calculations to establish local atomic ordering of the two-dimensional silicate frameworks<sup>17</sup>. In the absence of long-range 3D molecular order, NMR is the most informative means of obtaining detailed insights on the local structures of these and similar complex solid

materials. As a consequence, every additional constraint that NMR may provide can potentially increase the reliability of the NMR-based structural determination of such solids lacking long-range crystallinity. To that end, the use of the combined double-quantum and z-filtered IPAP experiment to measure  ${}^2J({}^{29}\text{Si-O-}{}^{29}\text{Si})$  couplings are expected to provide strong constraints in the analyses of complicated solid structures, including the surfactant-templated silicates.

By selectively exciting a given resonance and then applying a double-quantum filter before detection, it is possible to distinguish the spins that are coupled to the excited nuclei. For example, figure B.8c shows a double-quantum-filtered  ${}^{29}\text{Si}$  CP-MAS spectrum obtained using a selective through-bond DQ filter (with no z-filtered IPAP sequence included), where site 4 has been selectively excited. This method is based on the refocused INADEQUATE experiment, where a z-filter is inserted after CP to enable the selective excitation of only the desired resonance by using a selective  $90^\circ$  excitation pulse (figure B.7). Only the sites that are  $J$ -coupled to the excited  $S$  spins will yield a signal at the end of this experiment. It can be seen from this DQ-filtered MAS spectrum that the excited site 4 yields the most intense resonance, and that magnetization is transferred to sites 2, 3, and 5, but not to site 1. This is consistent with the connectivities shown in figure B.8a, where  ${}^{29}\text{Si}$  site 4 is linked via siloxane bridges to sites 2, 3 (twice), and site 5, but not site 1.

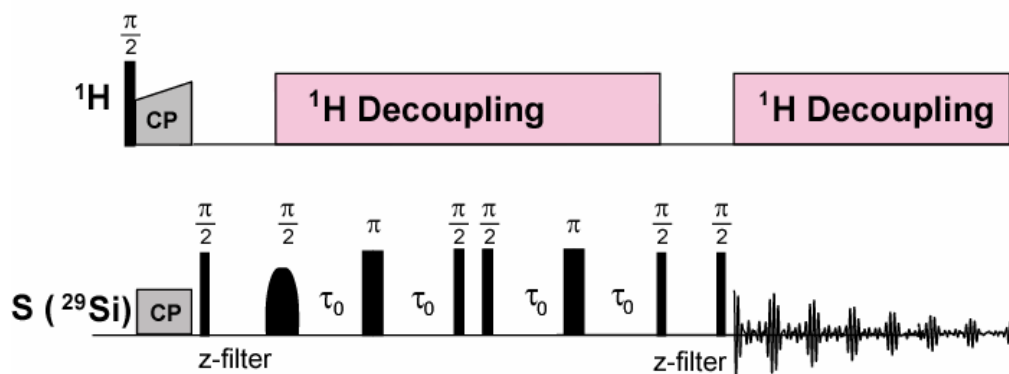


**Figure B.7.** Pulse sequence of the selective through-bond double quantum filter. After CP, the magnetization is directed back along the  $z$ -axis for the desired resonance to be selectively excited. The magnetization of the selectively excited spin is then transferred through homonuclear  $J$  couplings to bonded neighbors via a refocused INADEQUATE block. The length of the  $\tau_0$  delay is experimentally determined for optimized through-bond transfer.

Comparison of the conventional CP-MAS and DQ-filtered  $^{29}\text{Si}$  spectra in figures B.8b and B.8c for the 50%  $^{29}\text{Si}$ -enriched layered silicate-surfactant material shows significant differences in the intensities of the  $^{29}\text{Si}$  signals observed. This is due to several factors, including most importantly that only  $^{29}\text{Si}$ -O- $^{29}\text{Si}$  pairs involving site 4 have been selectively excited and detected. In addition, there is an overall sensitivity loss of about 1/2 due to the elimination of zero-quantum coherences by the DQ filter, with a portion of the magnetization also lost through transverse dephasing  $T_2'$  during the long spin echoes required due to the weak  $^{29}\text{Si}$ -O- $^{29}\text{Si}$   $J$  couplings. As expected, in figure B.8c,  $^{29}\text{Si}$  site 3 yields a signal with significantly greater integrated intensity than sites 2 and 5, consistent with each site 3 being linked to two sites 4 and vice-versa. The difference in the  $^{29}\text{Si}$  signal intensities associated with sites 2 and 5 could be due (i) to differences in CP efficiency from one site to another, (ii) to differences in the  $J$  couplings between pairs 2-4, 3-4, and 4-5, since the intensity

build up is proportional to  $\sin^2(2\pi J_{IS}\tau_0)$ , and/or (iii) to differences in the  $T_2'$  relaxation time from one site to another.

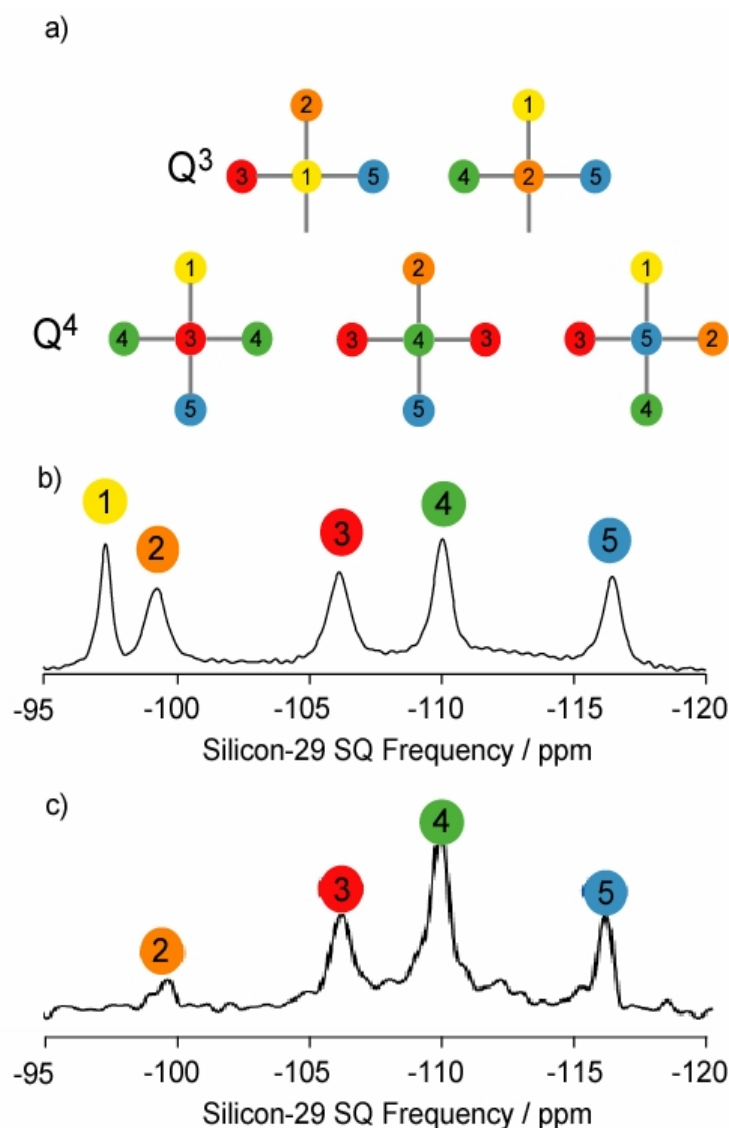


**Figure B.8.** (a) Schematic diagram illustrating  $^{29}\text{Si}$ -O- $^{29}\text{Si}$  connectivities among tetrahedrally coordinated Si sites in a surfactant ( $\text{CH}_3(\text{CH}_2)_{15}\text{-NMeEt}_2^+$  head group)-templated silicate with five molecularly ordered and equally populated Si sites enriched to 50% in  $^{29}\text{Si}$ . (b)  $^{29}\text{Si}$  CP-MAS spectrum (at 298 K) of the  $\text{CH}_3(\text{CH}_2)_{15}\text{-NMeEt}_2^+$ -surfactant-templated silicate layers, acquired within 8 transients, with a recycle delay of 3 s, and a contact time of 9 ms. (c) DQ-filtered  $^{29}\text{Si}$  MAS spectrum (at 298 K) of the surfactant-templated silicate material recorded using the pulse sequence of figure B.7. An E-BURP<sup>61</sup> soft pulse of 9.1 ms was applied to selectively excite the silicon-29 resonance of site 4. A total of 128 transients were accumulated with a recycle delay of 5 s. The length of the  $z$ -filters was set to 15  $\mu\text{s}$ , and the  $\tau_0$  delay was 9 ms.

## B.2. Analysis of NMR Lineshapes

### B.2.1. Primary results – Temperature dependence

First of all, to analyze NMR lineshapes of the silicate layers templated by  $\text{CH}_3(\text{CH}_2)_{15}\text{-NMe}_2\text{Et}^+$ ,  $^{29}\text{Si}$  CPMAS experiments have been realised as a function of the temperature. It seems that, in addition to the slight static disorder yielding chemical shift dispersion at ambient temperature, a reversible ordering/disordering process can be observed as a function of temperature.

Indeed, figures B.9a shows a series of  $^{29}\text{Si}$  CP MAS spectra acquired at temperatures ranging from 205 to 328 K. The resonances broaden dramatically and shift during sample cooling. (The  $^{29}\text{Si}$  sites 2 and 3 overlap and are thus not studied in detail here). In figure B.9b, the full width at half height (FWHH)  $\Delta^*$  of  $^{29}\text{Si}$  sites 1, 4 and 5 are plotted and a critical regime is identified between 270 and 300 K, in which the FWHH decrease dramatically on increasing the temperature. In the following sections, we will investigate the nature and origin of the disordering process that results in this temperature-dependent reversible variation of the  $^{29}\text{Si}$  NMR linewidths.

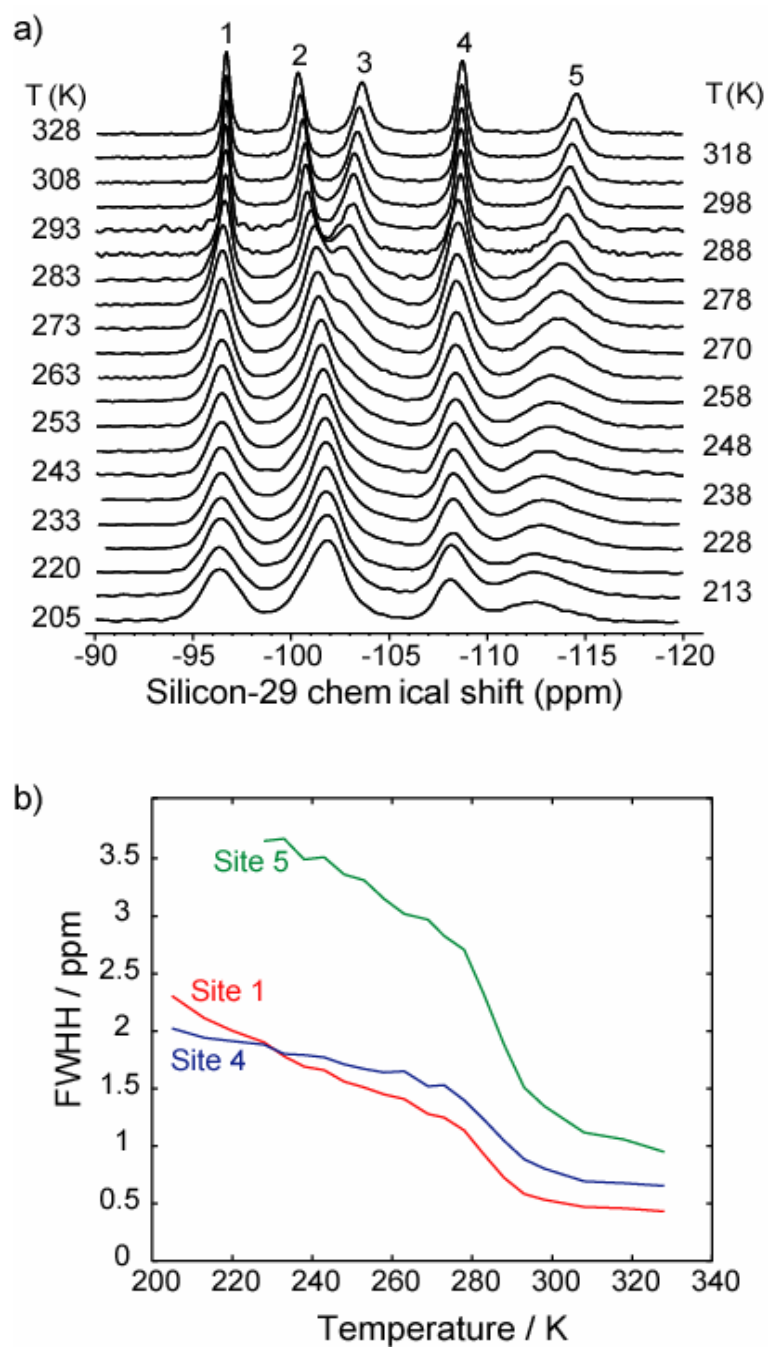


**Figure B.9.** (a) Temperature-dependent  $^{29}\text{Si}$  CP MAS NMR spectra of the surfactant-templated 50%  $^{29}\text{Si}$ -enriched silicate layers. Both broadening and shift in the peak positions can be observed when cooling down the samples. (b) Plot of the full width at half height (FWHH) as a function of temperature for the three  $^{29}\text{Si}$  sites that remain isolated in the whole temperature range considered here. The red, blue, and green curves correspond to sites 1, 2 and 5 respectively.

## B.2.2. Homogeneous and inhomogeneous broadening via the INADEQUATE experiment

We will see in this part that INADEQUATE experiments are more accurate to determine the homogeneous and inhomogeneous contributors to broadening. The robustness of the refocused INADEQUATE experiment when applied to disordered solids was demonstrated above and in the literature<sup>18</sup>. Here, we summarize the observations made in this part, and therefore show some similar figures. First, the nature of the broad lines observed in disordered solids is discussed, and opposed to the origin of the magnetization loss observed when applying the refocused INADEQUATE experiment to disordered solids. This naturally leads to the crucial concept of Transverse Dephasing Optimization (TDOP), introduced recently by De Paëpe and co-workers<sup>54, 58</sup>, and which has been of great importance in high resolution NMR of disordered solids in general.

The refocused INADEQUATE experiment is built from coherence transfer echoes<sup>41</sup>, during which the net evolution of the chemical shift interaction is refocused. As a consequence, only the homogeneous part of the lines is associated with dephasing that cannot be refocused by the spin-echo, and leads to the solid-state dephasing time  $T_2'$ . This transverse dephasing time  $T_2'$  is essentially dominated by residual anisotropic interactions, and in particular the dipolar couplings to the often abundant and strongly coupled protons. Indeed, the large magnitude of the magnetogyric ratio of the protons, and their abundance in most solids make a complete averaging by MAS impossible, thus rendering the use of heteronuclear

decoupling crucial in solids. The transverse dephasing time  $T_2'$  in solids is therefore different from the relaxation time  $T_2^{\text{liquid}}$  in liquid-state NMR, which arises from incoherent (relaxation) mechanisms. In solids the relaxation time  $T_2^{\text{solid}}$  represents a theoretical limit for the  $T_2'$  in the (hypothetical) case of perfect averaging of the dipolar interactions. This intrinsic incoherent relaxation time  $T_2^{\text{solid}}$  is expected to be generally longer than  $T_2^{\text{liquid}}$ , since the stochastic motions responsible for this relaxation are much weaker in solids. On the contrary, the transverse dephasing time  $T_2'$  strongly depends on MAS and heteronuclear decoupling conditions, and this has been exploited by De Paepe and co-workers to probe the efficiency of heteronuclear decoupling sequences in an extremely sensitive way<sup>54, 58</sup>. Indeed, using state-of-the-art heteronuclear decoupling techniques (such as TPPM<sup>62, 63</sup> SPINAL64<sup>64, 65</sup>) under fast MAS, the apparent  $^{13}\text{C}$  linewidths are generally dominated by the inhomogeneous broadening, even in highly crystalline compounds, thus making the comparison of the observable linewidths uninformative. On the other hand, by comparing the signal intensities obtained after a sufficiently long spin-echo, strong differences are observed, since the intensities are in this case directly proportional to  $\exp(-2\tau/T_2')$  and thus extremely sensitive to the dominant residual heteronuclear dipolar couplings. In disordered solids, this distinction between apparent and refocused linewidths is of particular importance, as illustrated in the following example.

In figure B.10a we show in green a CPMAS spectrum obtained from a sample of 11%  $^{13}\text{C}$ -enriched cellulose extracted from wood. The broad lines observed (from 250 to 600 Hz) arise from variations in the local environment having several origins. First, the sample is made of an ensemble of known polymorphs of cellulose (cellulose

$I_{\parallel}$ ,  $I_{\alpha}$ , and  $I_{\beta}$ , see reference 46), which have been identified by comparison with the NMR analysis of crystalline samples of celluloses from various origins, and to some disordered domains. The allomorphs identified differ essentially by a set of dihedral angles  $\varphi$ ,  $\psi$ , and  $\chi$  that define the geometry of the glycosidic linkage and the orientation of the hydroxyl-methyl group, and by their hydrogen-bonding patterns<sup>19, 66, 67</sup>. Second, since cellulose is known to organize in microfibrils, external fragments may have a different environment compared to fragments that are inside the microfibril, and finally, local defaults in the micro-fibrils might also result in distributed local fields for a given site. These two points are at least partially responsible for the disordered domains observed<sup>46</sup>. Superimposed on the CPMAS spectrum, we show in red a fictitious spectrum made of the Lorentzian peaks of full-width at half height (FWHH)  $\Delta' = 1/(\pi T_2')$ , measured for the resolved sites in the spectrum using the pulse sequence shown in figure B.10b. These refocused linewidths were obtained using the cosine-modulated (CM) scheme for heteronuclear decoupling<sup>65</sup>, with phase excursion and period of the phase modulation being optimized through the TDOP approach. (For this particular compound, in the MAS and radio-frequency irradiation conditions used here, the CM heteronuclear decoupling sequence turned out to provide significantly improved  $T_2'$  compared to the SPINAL64 scheme<sup>64</sup>, whose pulse length parameter was also optimized using TDOP.) The refocused linewidths of figure B.10a were obtained by means a special treatment, discussed in reference 68 to extract only the transverse dephasing time of the nuclei that were not  $J$ -coupled to other  $^{13}\text{C}$  nuclei. The difference between the apparent ( $\Delta^*$ ) and the refocused linewidth is remarkable. As a result, the broad inhomogeneous lines observed in disordered solids can be roughly considered as

distributions of individual (Lorentzian) lines having an homogeneous linewidth being the refocused linewidth  $\Delta'^{14}$ , as illustrated in figure B.10c.

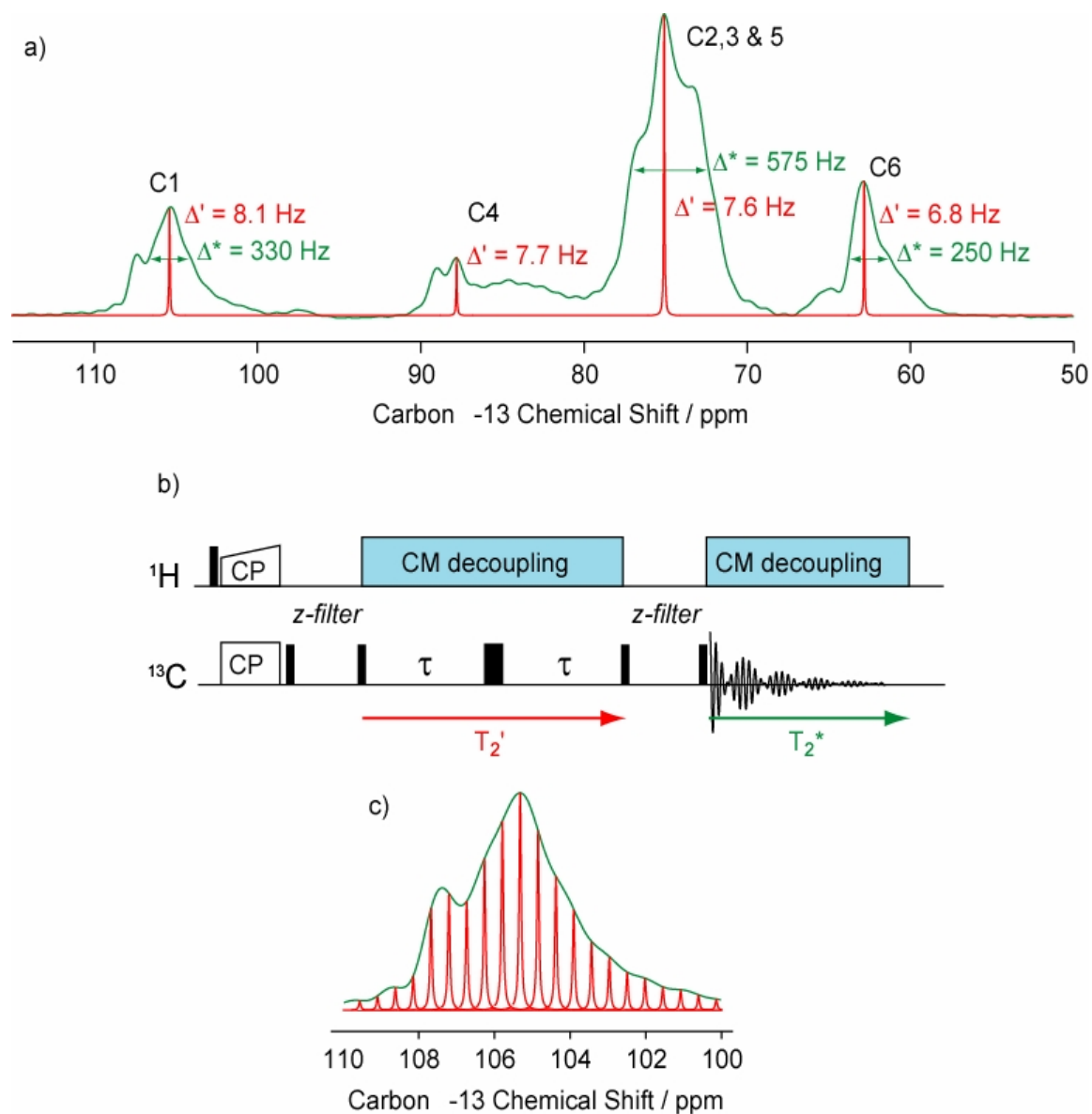


**Figure B.10.** (a) Superposition of the CP-MAS spectrum of 11%  $^{13}\text{C}$ -enriched cellulose extracted from wood (in green) and a fictitious spectrum (in red) showing the refocused linewidth measured for each resolved site in the spectrum in optimized transverse dephasing conditions (25 kHz MAS, cosine-modulated CM heteronuclear decoupling at a nutation frequency of 140 kHz). The magnetization loss during the spin-echoes in the refocused INADEQUATE sequence is governed by the (red) refocused line widths rather than the (green) apparent line width, thus illustrating the robustness of the refocused INADEQUATE

experiment for disordered solids<sup>1</sup>. (b) Pulse sequence of the z-filtered spin-echo experiment used to measure the refocused line widths in cellulose. (c) Inhomogeneous peak corresponding to site C<sub>1</sub> of cellulose, described as a superposition of individual Lorentzian lines of full-width at half height  $\Delta'$ , as proposed by Sakellariou *et al.*<sup>14</sup>.

As a consequence of the discussion above, the magnetization loss during a spin-echo, which is the major potential source of sensitivity loss in the refocused INADEQUATE experiment, may be extremely small in disordered solids despite broad apparent lines. As a result, this technique is very sensitive for disordered solids, especially when combined with the TDOP approach. In addition, these considerations also have a major impact on the resolution in the 2D lineshapes.

### B.2.3. Results

INADEQUATE experiments have then been done at different temperatures on the Si. Figure B.11a shows the superimposition of two z-filtered refocused (zfr-) <sup>29</sup>Si{<sup>29</sup>Si} INADEQUATE spectra acquired at 298 K (in black) and 278 K (in red), using the pulse sequence shown in figure B.11b. Both spectra show a wide range of two-dimensional lineshapes arising from slight structural disorder. The 2D NMR line shapes are more elongated at low temperature, corresponding to an increased dispersion in the isotropic frequencies associated with a given site, which results from a disordering process confirming that the broadening observed in the 1D spectra is due to increasing shift distributions.

Furthermore, we note a more detailed comparison of the lineshapes shows a slight broadening in a direction *orthogonal* to the main axis of the ellipsoidal peaks (the lowest contour level corresponding to 15% of the maximum intensity of each spectrum) (figure B.11a). This latter broadening is potentially of a different nature compared to the elongation of the peaks parallel to the main axis and could correspond to a *homogeneous* broadening which varies with temperature.

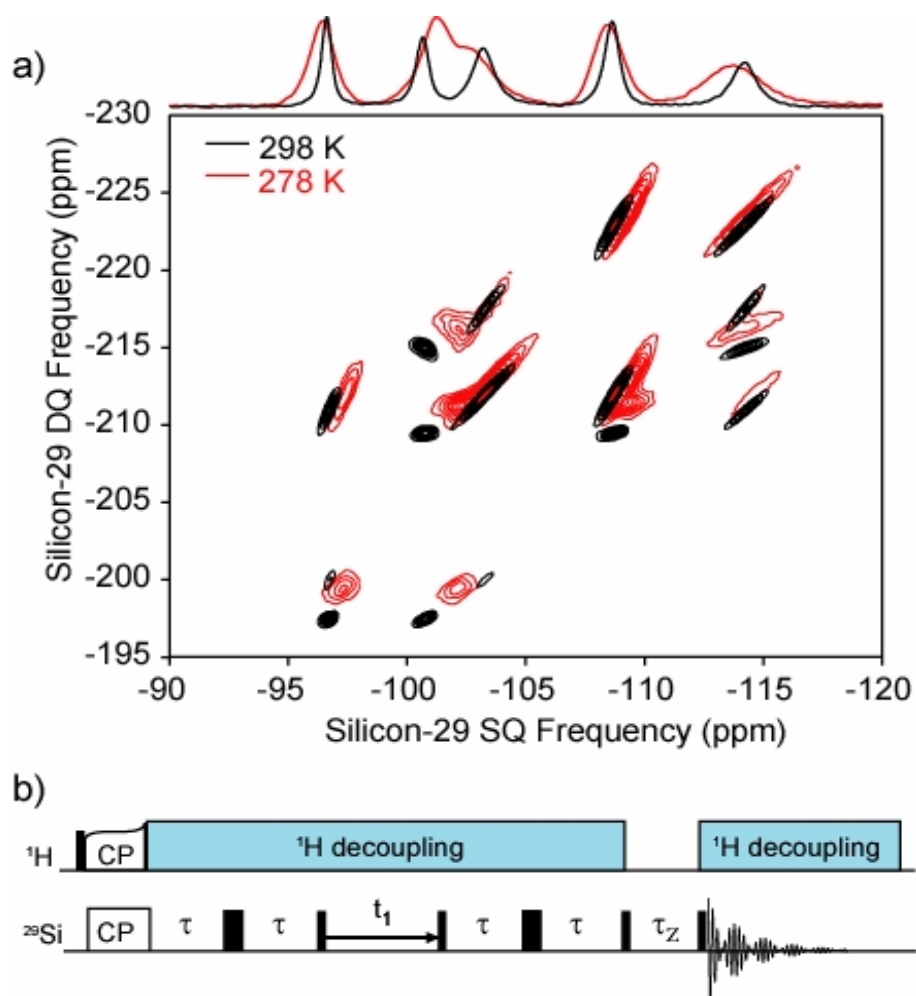


**Figure B.11.** (a) Superposition of two  $^{29}\text{Si}$  z-filtered refocused (zfr) INADEQUATE spectra acquired recorded at 278 K (red contours) and 298 K (black contours) in otherwise similar conditions. The particular shape and temperature-dependence of the correlation peaks reveal the presence of a disordering process. In each spectrum, the contour levels correspond to 15, 25, 35, 45, 55, 65, 75, 85, and 95 % of the maximum intensity. (b) Pulse sequence used to record the zfr-INADEQUATE spectra shown in (a). The z-filter allows elimination of undesired dispersive anti-phase contributions due to multiple couplings.

## B.3. Characterizing Chemical Exchange in Disordered Solids

### B.3.1. Experimental

It has recently been shown<sup>18, 46, 65</sup> that the limiting resolution (or pixel size) in 2D lineshapes of solids having some extent of disorder is strongly related to the refocused linewidth  $\Delta'$  of an observed site. This purely homogeneous refocused linewidth  $\Delta'$  (and not the observed 1D linewidth  $\Delta^*$ ) is associated with the transverse dephasing time  $T_2'$  during a spin-echo, and that the refocused linewidth is usually much less than the apparent linewidth in the 1D spectrum ( $\Delta' \ll \Delta^*$ ). In protonated solids,  $\Delta'$  is generally dominated by the residual heteronuclear dipolar couplings to the protons<sup>54, 58</sup>. In particular, this linewidth can crudely be considered in disordered solids as the limiting linewidth associated with a spin in a given local environment<sup>14, 46</sup>. So far, measurement of  $T_2'$  has not been related to structural or dynamics parameters (since it is often dominated by residual coherent dipolar couplings).

In order to evaluate the contribution of this homogeneous broadening to the two-dimensional lineshapes of the zfr-INADEQUATE spectra shown in figure B.11a, systematic spin-echo measurements of transverse dephasing time  $T_2'$  as a function of temperature have been carried out for <sup>29</sup>Si sites 1, 4 and 5 in our sample, using the pulse sequence shown in figure B.12a.

Because of the partial enrichment (ca. 50%) of the silicate layers in  $^{29}\text{Si}$ , the  $^2J_{\text{Si-Si}}$  couplings between the observed site and the neighboring  $^{29}\text{Si}$  atoms across the siloxane bonds were refocused by replacing the  $\pi$  pulse of the standard spin-echo experiment by a semi-selective  $\pi$  pulse on the observed site. In figure B.12b measured  $T_2'$  are plotted for sites 1, 4, and 5 in red, blue and green respectively. A critical temperature regime is identified around 275 K, in which increased transverse dephasing is observed, corresponding to a broadening of the associated  $\Delta'$ , that could potentially affect the two-dimensional lineshapes. The decoupling scheme and proton nutation frequency being kept identical at every temperature, it seems that a dynamical process is the dominant contribution to the homogeneous broadening in this regime.

Figure B.12c shows expansions of the 4-5 correlation peak at the frequency of  $^{29}\text{Si}$  site 5 extracted from the two zrf-INADEQUATE spectra shown in figure B.11a. Figure B.12c, left shows the 4-5 correlation at 278 K, with the projection of the selected region on top, and figure B.12c, right shows the same cross peak from the spectrum acquired at 298 K. In each plot, the lowest contour level corresponds to 15% of the intensity of the selected region. Lorentzian peaks have been displayed on top of the 2D plots whose FWHH  $\Delta' = 1/(\pi T_2')$  is obtained from the  $T_2'$  measured for site 5 at the corresponding temperature. Superimposed are circles whose diameter corresponds to the width (in dimension F2) at 15% of the maximum intensity of the Lorentzian. (Note that these should be ellipsoids, and not circles, as the intrinsic width in the DQ dimension is not known). This allows a qualitative estimation of the contribution of the homogeneous broadening to the two-dimensional peaks.

Thus, figure B.12c clearly shows that the much shorter  $T_2'$  measured for site 5 at 278 K ( $21.6 \pm 1.4$  ms) than at 298 K ( $54 \pm 11$  ms) is responsible for the broadening observed perpendicular to the principal axis of the ellipsoidal cross peaks. We will investigate in the next section the physical origin of the low  $T_2'$  values measured for all the sites in the critical temperature regime around 280 K.

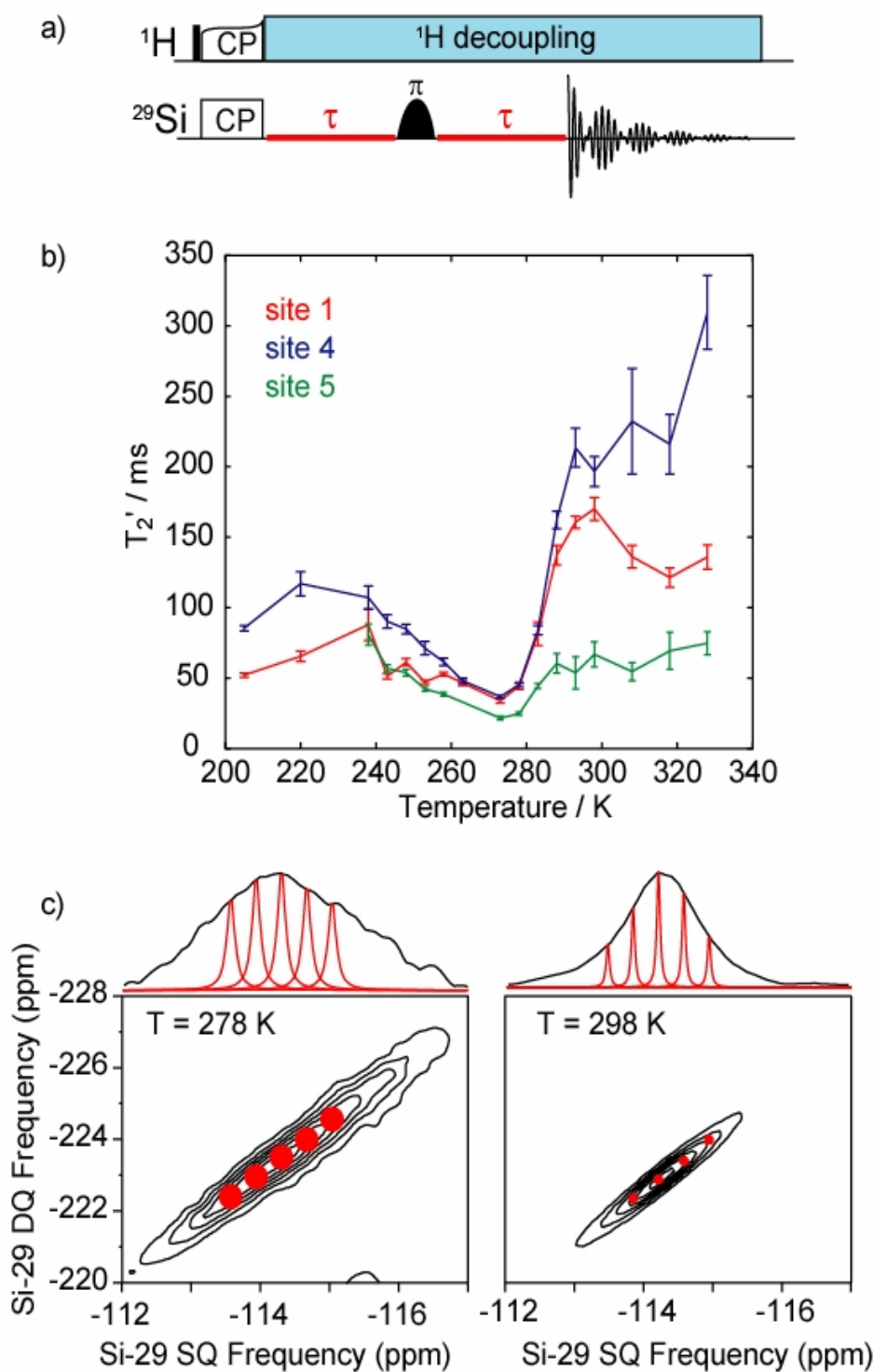


**Figure B.12.** (a) Selective spin-echo pulse sequence for measuring transverse dephasing times  $T_2'$  in enriched species. The use of a semi-selective refocusing pulse allows for J-coupling modulation removal. (b) Plot of the measured  $T_2'$  as a function of temperature for all of the  $^{29}\text{Si}$  sites that remain isolated in the whole temperature range considered. A critical temperature regime is observed around 275 K, where the  $T_2'$  falls down for every  $^{29}\text{Si}$  site.

(c) In black, enlarged region of the two zfr-INADEQUATE spectra shown in figure B.11a, recorded at 278 K (left) and 293 K (right) corresponding to one of the 4-5  $^{29}\text{Si}$ - $^{29}\text{Si}$  correlation. Contour levels correspond to 15, 30, 45, 60, 75, and 90 % of the maximum intensity of the selected region. Above are shown in black the projections of the selected region (1D chemical shift distributions of  $^{29}\text{Si}$  site 5). Superimposed, in red, are series of Lorentzian lines of FWHH  $1/(\pi T_2')$ , where  $T_2'$  is the value measured for site 5 at the corresponding temperature. The red circles on the 2D plots below have a diameter that corresponds to the width of these Lorentzian lines at 15% of their maximum intensity, in order to allow visual comparison with the lowest contour level of the experimental spectra (in black).

### B.3.2. Review of Chemical Exchange

We recall that in liquid-state NMR, it is well known that the transverse relaxation time  $T_2$  can be used to obtain detailed information on dynamics, through the dephasing induced by changes in the isotropic frequency of a given nucleus due to chemical exchange on a timescale around the chemical shift difference. For the simplest case of a two-site exchange between equally populated forms:



analytical formulas have been proposed that predict the transverse dephasing rate  $R_2=1/T_2$  in the so-called intermediate exchange regime in liquids<sup>69-71</sup>.

$$R_2 = R_2^{liquid} + R_2^{exch}$$

with

$$R_2^{exch} = k_{exch} - \sqrt{\frac{1}{2}(G + |G|)}$$

where  $G = k_{exch}^2 - \pi^2 \Delta\nu$ , with  $k_{exch}$  the exchange rate and  $\Delta\nu$  the chemical shift difference between the isotropic frequencies of the observed site in forms *A* and *B* in absence of exchange and where  $R_2^{liquid}$  is the liquid-state transverse relaxation rate in the absence of the chemical exchange process. The exchange rate  $k_{exch}$  is related to the temperature by the Eyring relationship:

$$k_{exch} = \frac{k_B T}{h} \exp\left(-\frac{\Delta_r G^\ddagger}{RT}\right)$$

where  $\Delta_r G^\ddagger$  is the free activation energy of the chemical reaction.

In solids, the situation is significantly different. The transverse dephasing rate  $R_2' = 1/T_2'$  is for spin 1/2 nuclei in protonated materials dominated by the contribution of residual dipolar couplings  $R_2^{ResDip}$ . The incoherent (relaxation) contribution  $R_2^{solid}$  is generally expected to be much smaller than  $R_2^{ResDip}$  in the solid-state. Our hypothesis is that in the case presented here, in the critical exchange regime,  $R_2'$  is dominated by the contribution due to the chemical exchange process  $R_2^{exch}$ , and should therefore agree with the liquid-state model. The  $R_2'$  is modeled as follows:

$$R_2' = \frac{1}{T_2'} = R_2^{solid} + R_2^{ResDip} + R_2^{exch} = \frac{1}{T_2^{solid}} + \frac{1}{T_2^{ResDip}} + \frac{1}{T_2^{exch}}$$

with

$$R_2^{exch} > R_2^{ResDip} \gg R_2^{solid} \text{ in the intermediate exchange regime.}$$

In such a case, the transverse dephasing time  $T_2'$  can be used to quantitatively characterize the chemical exchange process even in the presence of

inhomogeneous broadening preventing the observation of the chemical exchange from the one-dimensional lineshapes.

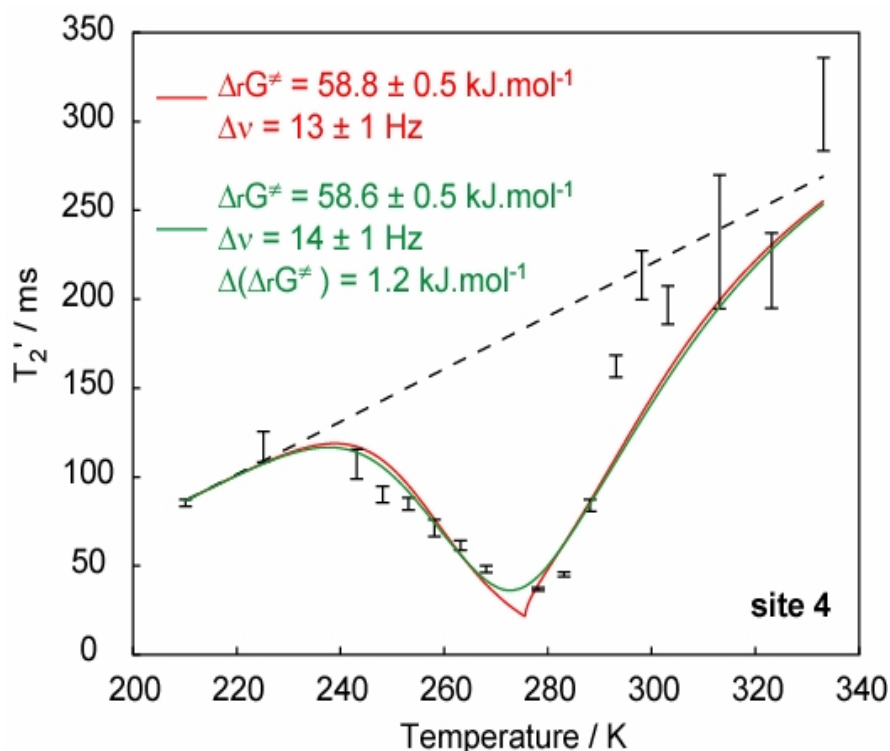
### B.3.3. Results

Figure B.13 shows the measured  $T_2'$  of site 4 as a function of temperature. Outside the region corresponding to the critical temperature regime, *i.e.* the intermediate exchange regime in our hypothesis,  $T_2'$  is dominated by the complicated spin dynamics responsible for residual heteronuclear dipolar couplings under heteronuclear decoupling and magic angle spinning. This regime is described purely phenomenologically by fitting the points at  $T < 240$  K and  $T > 300$  K to a straight line:

$$T_2^0(T) = 1 / (R_2^{solid}(T) + R_2^{ResDip}(T)) = aT + b$$

which is shown as a dashed line in figure B.13.  $R_2^0(T) = 1/T_2^0$  is then inserted in the model of equation of  $R_2$  instead of  $R_2^{liquid}$ .

The experimental  $T_2'$  values are then fitted to the resulting expression, with  $\Delta_r G^\ddagger$  and  $\Delta v$  being the adjustable parameters. The corresponding best fit and optimal values of  $\Delta_r G^\ddagger$  and  $\Delta v$  obtained for  $^{29}\text{Si}$  site 4 are shown in red in figure B.13.



**Figure B.13.** In black, plot of the measured  $T_2'$  for  $^{29}\text{Si}$  site 4 as a function of temperature. The black dashed line corresponds to the phenomenological description of the residual dipolar and relaxation contribution to the transverse dephasing rate  $R_2^{\text{resdip}} + R_2^{\text{relax}}$ , best fit of the external points ( $T < 230$  K and  $T > 295$  K) to a linear temperature-dependence function. In red is shown the best fit of the central region ( $230$  K  $< T < 295$  K) to the liquid-state-like  $T_2^{\text{exch}}$  function described in the text, using the free activation energy  $\Delta_r G^\ddagger$  and the low temperature splitting between the exchanging sites  $\Delta v$  as optimized parameters. In green is shown a similar fit including a Gaussian distribution of free activation energies whose standard deviation  $\Delta(\Delta_r G^\ddagger)$  is additionally optimized.

Our model is in extremely good agreement with the experimental data, and gives a free activation energy  $\Delta_r G^\ddagger = 58.8 \pm 0.2$  kJ.mol $^{-1}$  that is perfectly physically reasonable for a  $180^\circ$  rotation of the surfactant headgroup, and a low temperature  $^{29}\text{Si}$  splitting between the two orientations of the surfactant headgroup of  $13.1 \pm 0.4$

Hz<sup>a</sup> (*i.e.*  $0.132 \pm 0.004$  ppm at 11.74 Tesla). Free activation energies and low-energy splittings have been obtained in the same way for sites 1 and 5 from the measured  $T_2'$  values and the results are summarized in table B.1. Interestingly, the calculated free activation energies for the three sites are in excellent agreement with each other, which confirms the passive role of the silicon sites as a spectator of a single dynamic process. All the <sup>29</sup>Si sites are in addition affected in a similar way, since the measured low temperature splittings are also of similar magnitudes.

<sup>29</sup> Si Site	$\Delta_r G^\ddagger$ (kJ.mol <sup>-1</sup> )	$\Delta\nu$ (Hz)	$\Delta\nu$ (ppm)
1	$58.6 \pm 0.7$	$15 \pm 15$	$0.15 \pm 0.15$
4	$58.8 \pm 0.2$	$13.1 \pm 0.4$	$0.132 \pm 0.004$
5	$58.8 \pm 0.4$	$16 \pm 1$	$0.16 \pm 0.01$

**Table B.1.** Measured free activation energies and low-temperature splitting of the <sup>29</sup>Si sites from the surfactant headgroup two-site jump.

### B.3.4. Discussion

We now turn our attention to the temperature dependence of the apparent linewidths  $\Delta^*$  (figure B.9b). The inhomogeneous chemical shift distributions associated with the elongated two-dimensional lineshapes and the effects due to chemical exchange can be analyzed in a concerted manner. The first question is: does the exchange dynamics measured through  $T_2'$  explain the observed line broadening at low temperature?

Figure B.14a shows (in black solid line) the considered static inhomogeneous distribution of <sup>29</sup>Si site 4 taken from the experimental CP-MAS lineshape at 320 K.

This temperature corresponds to the fast exchange regime, and every individual position in the inhomogeneous distribution can thus be represented by a Lorentzian of FWHH  $\Delta' = 1/(\pi T_2')$ , where  $T_2'$  is the value measured at this temperature for site 4, as depicted for arbitrary positions by the blue, red, and yellow lines in figure B.14a. At lower temperature these individual lines are influenced by the chemical exchange process, as the intermediate exchange regime is reached. This regime is defined by<sup>72</sup>:

$$T_2^0 < \tau < \left( \frac{1}{2} \pi^2 \Delta \nu^2 T_2^0 \right)^{-1}$$

where

$$\tau(T) = 1/k(T) = \frac{h}{k_B T} \exp\left(\frac{\Delta_r G^\ddagger}{RT}\right)$$

with  $T_2^0(T)$ ,  $\Delta \nu = \nu_B - \nu_A$  and  $\Delta_r G^\ddagger$  being as determined in previous section. The shape  $f_{\text{exch}}(\nu)$  of the individual lines is then given by<sup>72</sup>:

$$f_{\text{exch}}(\nu) = \frac{2\tau(T)\Delta \nu^2}{(\nu - \nu_C)^2 + \pi^2 \tau(T)^2 (\nu - \nu_A)^2 (\nu - \nu_B)^2}$$

In analogy with liquid state NMR each individual line first broadens (figure B.14b) and then splits in two individual broad lines (figure B.14c) and these narrow at even lower temperatures (figure B.14d), until the slow exchange regime is reached, in which the linewidths are no longer affected by temperature.

In figure B.14 we show a simulated predicted lineshape as a solid black line which includes the effect of the above described exchange broadening calculated across the whole line. The experimental lineshapes at each temperature are shown as dashed lines (artificially shifted when required to match the maximum intensity of

the simulated lines). From this figure, it is clear that the two-site jump of the surfactant headgroup as characterized before is not responsible for the increase of the apparent FWHH  $\Delta^*$  from 67 to 178 Hz observed for site 4 when cooling the sample from 320 K down to 240 K. Therefore, another mechanism must be responsible for this broadening. However, the critical variations in  $\Delta^*$  observed in a temperature regime close to the intermediate exchange regime of the surfactant headgroup rotation (figure B.9b) indicates that the additional disordering process is nevertheless related to the headgroup rotation.

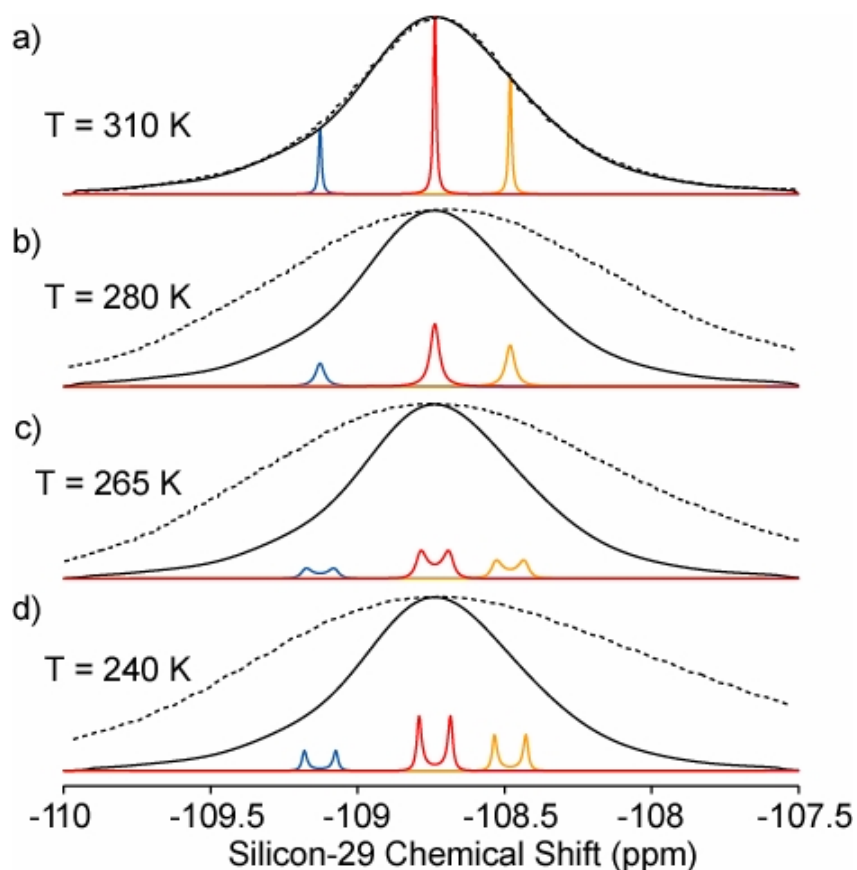


**Figure B.14.** Plots of the expected  $^{29}\text{Si}$  NMR lineshape variation of the apparent broadening of the line corresponding to site 4 as a function of temperature when considering the two-site exchange previously described as the only source of broadening. In blue, red, and yellow are shown the evolutions of the individual lines calculated from the exchange process. The experimental lines at the corresponding temperatures (artificially shifted to match the position of the simulated maximum) are shown for comparison as dashed lines. Obviously this simple model is not able to predict the broadening observed in figure B.9a when decreasing the temperature.

## B.4. Characterizing Static Structural Disorder in Disordered Solids

In section 2 and 3 it was assumed that the elongated 2D lineshapes are due to the presence of a static structural disorder, but the nature of this disorder was not discussed. In the following this disorder is probed on the basis of two-bond silicon-silicon scalar couplings across siloxane bonds  ${}^2J({}^{29}\text{Si-O-}{}^{29}\text{Si})$  at 298 K (above the critical regime). Then the two-site chemical shift correlations are compared with the temperature-dependent processes discussed previously, showing that they are probably of the same nature.

### B.4.1. Extraction of Site to Site Chemical Shift Correlation Slopes

It has been shown that inhomogeneous distributions of isotropic chemical shifts can be associated with distributions of  $J$ -couplings to the surrounding atoms<sup>12, 73</sup>. In particular, Massiot and coworkers have observed  ${}^2J({}^{29}\text{Si-O-}{}^{29}\text{Si})$  coupling distributions in fully  ${}^{29}\text{Si}$ -labelled silicate<sup>73</sup>.

The discussion above has revealed the presence of a disordering process which is concomitant with surfactant headgroup dynamics, when decreasing temperature. Information on the nature of this process can be extracted through a cross-analysis of the correlated lineshapes at 298 K (figure B.10a, black spectrum)

and the temperature dependence of the  $^{29}\text{Si}$  chemical shifts in figure B.8a. To do this, we must first define the notion of “degrees of correlation” observed in the 2D correlation spectra.

For each silicon-silicon pair, a chemical shift correlation slope was obtained using the following procedure. The 2D cross peak spectral intensities were extracted from zfr-INADEQUATE (for  $J$ -coupled pairs) or post-C7<sup>74</sup> DQ NMR spectra for the non- $J$ -coupled pairs (*i.e.* 1-4 and 2-3). For each cross peak two conditional probability matrices  $M_1$  and  $M_2$  were constructed<sup>46</sup>, and nearly all the pairs showed a highly linear correlation profile.

$$M_1(\omega_A^i, \omega_B^k) = P_{\omega_B^k}(\omega_A^i)$$

$$M_2(\omega_A^i, \omega_B^k) = P_{\omega_A^i}(\omega_B^k)$$

with  $P_{\omega_A^i}(\omega_B^k)$  as the probability that the B site resonates at the frequency  $\omega_B^k$  given that the A site resonates at  $\omega_A^i$  (and respectively by permutation for the other).

Correlation slopes  $c_{ij}^1$  and  $c_{ij}^2$  were extracted from matrices  $M_1$  and  $M_2$ , respectively.  $c_{ij}^1$  and  $c_{ij}^2$  are respectively the main directing coefficient of the matrices  $M_1$  and  $M_2$ . The significant differences observed between the slopes extracted from  $M_1$  and  $M_2$  provides an indication of the degree of correlation between the chemical shifts of the two sites. The larger the difference is, the weaker the correlation is, up to the limit where  $M_1$  has a strictly horizontal slope, and  $M_2$  a perfectly vertical slope, which would indicate the absence correlation. We thus define the overall chemical shift correlation  $c_{ij}$  between two  $^{29}\text{Si}$  sites to be the normalized geometric average of the two slopes:

$$c_{ij} = \frac{c_{ij}^1}{|c_{ij}^1|} (c_{ij}^1 c_{ij}^2)^{1/2}$$

Then, the *degree of chemical shift correlation*  $r_{ij}$ , is determined as follows :

$$r_{ij} = c_{ij} / \max(|c_{ij}^1|, |c_{ij}^2|)$$

It ranges from 0 to 1, 0 meaning no correlation, and 1 meaning a total correlation between the two sites.

## B.4.2. Static and Temperature-Dependent Disorder

### B.4.2.1. Results

The close examination of the reorientational dynamics of the surfactant headgroups as reflected in the  $^{29}\text{Si}$  transverse dephasing behavior has revealed the presence of a co-existing disordering process when decreasing temperature.

Information on the nature of this process can be extracted through a cross-analysis of the correlated lineshapes at 298 K (figure B.11a, black spectrum) and the temperature dependence of the  $^{29}\text{Si}$  chemical shifts in figure B.9a. For example sites 2 and 5 have an opposite temperature dependency (figure B.15a), and the 2D cross-peaks between 2 and 5 (in figure B.15b) have characteristic orientations of a correlation between high frequencies of one site with the low frequencies of the other site.

On the contrary, the peaks corresponding to  $^{29}\text{Si}$  sites 3 and 4 are both shifted to high frequencies when decreasing the temperature (figure B.15a), and the static 2D lineshapes at 298 K show remarkably parallel elongation (figure B.15b) which is a characteristic of a strong correlation between high frequencies of both sites, and between low frequencies of both sites.

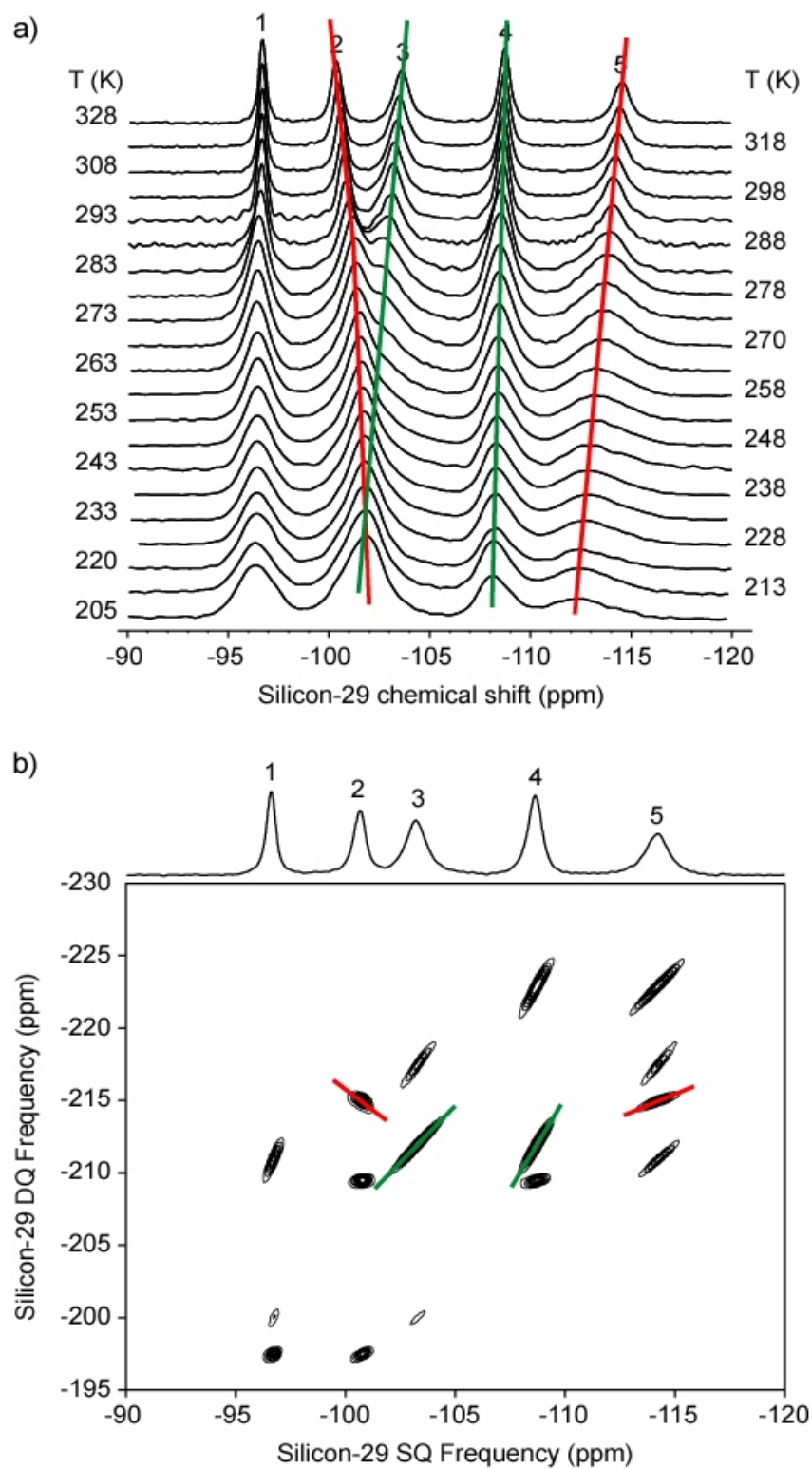


**Figure B.15.** (a) Temperature-dependent  $^{29}\text{Si}$  CP MAS NMR spectra of the surfactant-templated 50%  $^{29}\text{Si}$ -enriched silicate layers. (b) Silicon-29  $z$ -filtered refocused INADEQUATE spectrum of the  $\text{CH}_3(\text{CH}_2)_{15}\text{-NMe}_2\text{Et}^+$ -templated silicate layers at 298 K.

These observations have been quantified, and the results are summarized in table B.3. Figure B.16 displays the chemical shift variations  $\delta_i(T) - \delta_{i,\min}$  for each site  $i$  (ranging from 1 to 5) as a function of temperature (position of the maximum of the peak), where  $\delta_{i,\min}$  is the lowest shift observed for site  $i$  in the temperature range explored. As an estimate, these curves were fitted to linear functions of temperature, and slopes have thus been extracted for each site ( $a_i$  with  $i = 1, 2 \dots 5$ ) (see table B.2). For each pair of sites the ratio of the corresponding slopes  $a_i/a_j$  is displayed in table B.3 using the convention  $i > j$ , together with site-to-site chemical shift correlations  $c_{ij}$  ( $i > j$ ) extracted from 2D correlation spectra recorded at one temperature (298K) using the procedure described previously (examples in figures B.17a to B.17c). The latter provide a quantitative estimation of the relative variation of the chemical shifts associated to two different sites. They yield information on the static disorder at 298 K, by opposition with the temperature-dependent disordering process, and directly correspond to the relative orientation of the elongated 2D lineshapes in the zrf-INADEQUATE spectrum (figure B.11a in black). Finally, in the last column of table B.2 we give the degree of chemical shift correlation  $r_{ij}$  between sites  $i$  and  $j$ .

<sup>29</sup> Si Site (i)	$\delta(T)$ slopes $a_i$ (ppb.K <sup>-1</sup> )	<sup>29</sup> Si- <sup>29</sup> Si Pair	$\delta(T)$ slope ratio ( $a_i/a_j$ ) <sup>a</sup>	Chemical shift Correlation ( $c_{ij}$ ) <sup>b</sup>	$r_{ij}$
1	-3.5	1-2	-3.9	-1.32	0.44
2	14	1-3	5.5	2.47	0.48
3	-19	1-4	1.5	1.42	0.20
4	-5.3	1-5	5.7	2.60	0.62
5	-20	2-3	-1.4	-2.02	0.82
		2-4	-0.4	-1.32	0.68
		2-5	-1.5	-2.01	0.79
		3-4	0.3	0.71	0.76
		3-5	1.0	1.17	0.78
		4-5	3.7	1.78	0.78

<sup>a</sup> with  $i > j$

<sup>b</sup> with  $i > j$ . Extracted from the zfr-INADEQUATE spectrum at 298 K (figure B.11a)

**Table B.2.** Measured temperature-dependent shift slopes, and corresponding site to site ratios, experimental site to site chemical shift correlations, and correlation degrees.

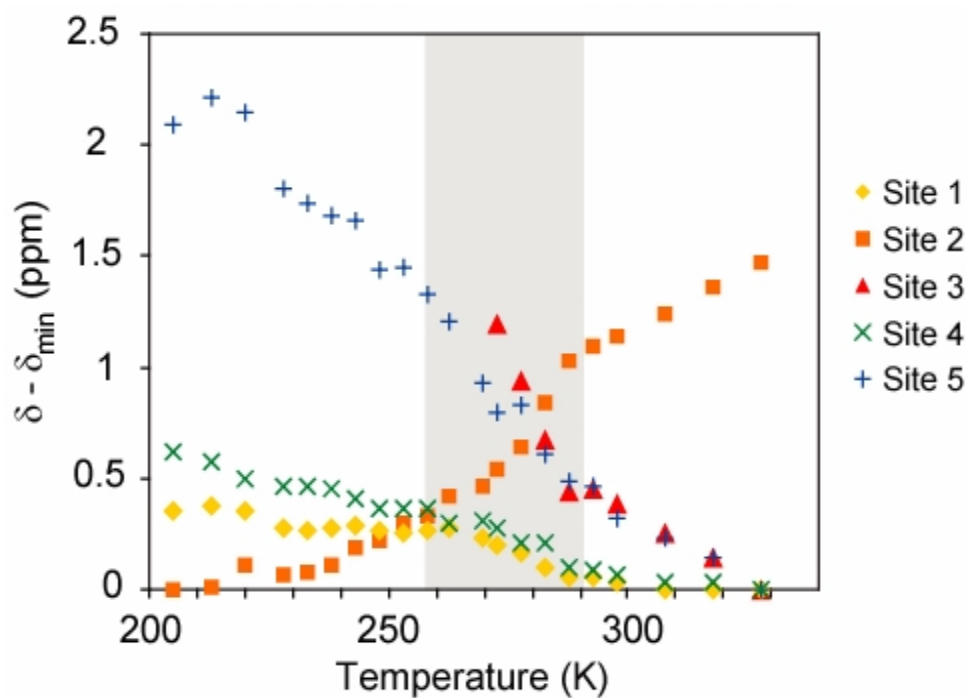


**Figure B.16.** Plot of the variation in the position of the maximum of each resolved peak in the series of  $^{29}\text{Si}$  CP MAS NMR spectra shown in figure B.18a as a function of temperature.

Chemical shift values reported here are of the form  $\delta_i(T) - \delta_{i, \min}$  with  $i = 1, 2 \dots 5$  corresponding to the  $^{29}\text{Si}$  site number,  $\delta_{i, \min}$  and being the minimum chemical shift value of site  $i$  over the temperature range considered. Site 1, 2, 3, 4 and site 5 shifts are respectively indicated by yellow diamonds, orange squares, red triangles, green “x”, and blue “+”.

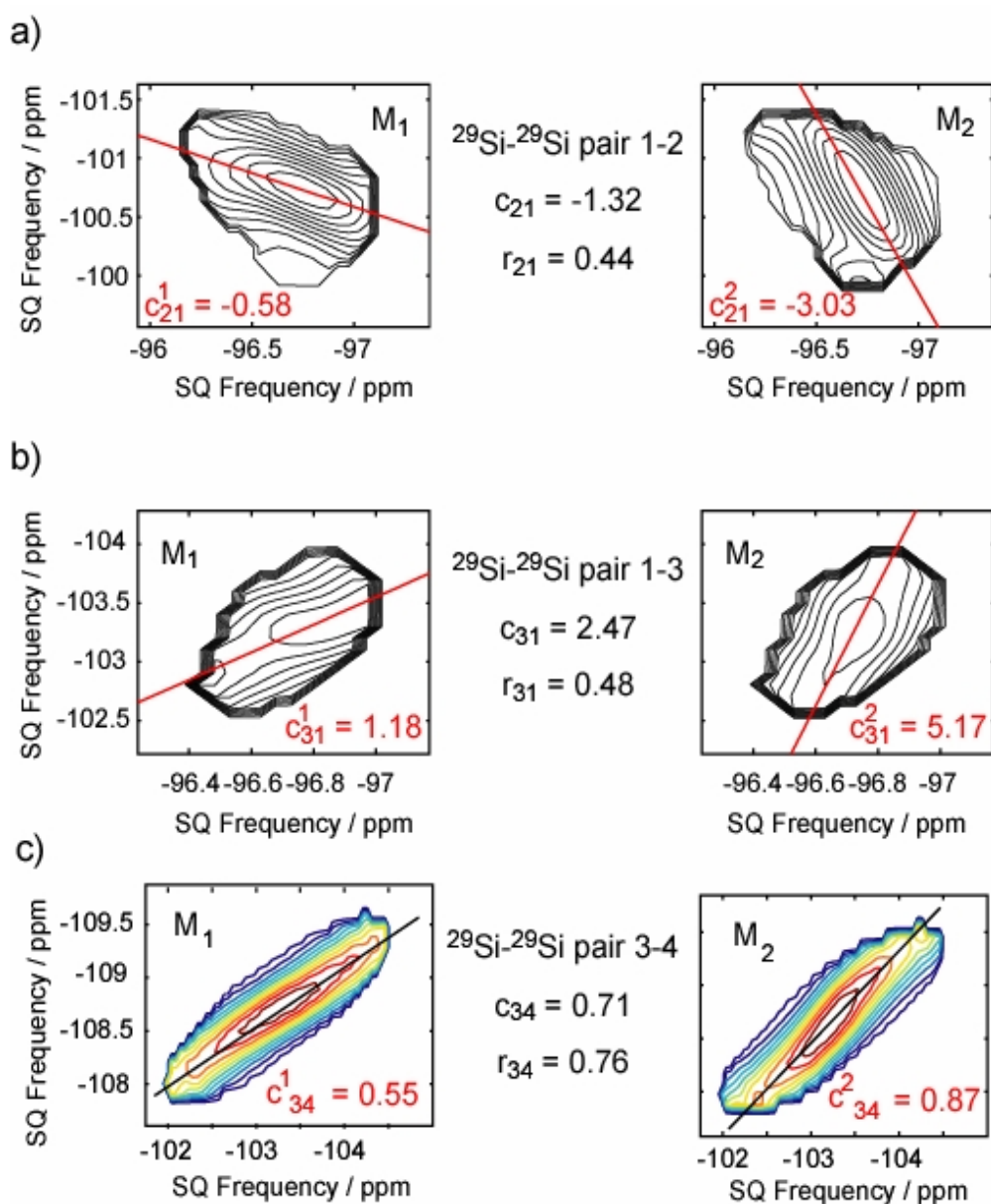


**Figure B.17.** Examples of conditional probability matrices extracted from the zfr-INADEQUATE spectrum (see section 4.4 for the extraction procedure) for the  $^{29}\text{Si}$ - $^{29}\text{Si}$  pairs 1-2 (a), 1-3 (b), and 3-4 (c). Superimposed in red (black for (c)) are the best fits of  $M_1$  and  $M_2$  maximum intensities to straight lines, and the associated  $c^1_{ij}$  and  $c^2_{ij}$  values (convention  $i > j$ ), and we show between the two matrices the calculated chemical shift correlation  $c_{ij}$ , and the degree of chemical shift correlation  $r_{ij}$ . Pairs 1-2 and 1-3 illustrate the case of a low degree of correlation, which results in significantly different slopes  $c^1_{ij}$  and  $c^2_{ij}$ , high frequencies being correlated with low frequencies of the other site for pair 1-2 ( $c_{ij} < 0$ ), whereas pair 1-3 shows

a high frequency-high frequency correlation ( $c_{ij} > 0$ ). Finally,  $^{29}\text{Si}$ - $^{29}\text{Si}$  pair 3-4 illustrates the case of a high degree of chemical shift correlation.

#### **B.4.2.2. Discussion**

In figure B.18, the chemical shift correlations  $c_{ij}$  at 298 K are linked to the  $a_i/a_j$  ratios for the different  $^{29}\text{Si}$ - $^{29}\text{Si}$  pairs. (The “error” bars are related to  $(r_{ij})^{-1}$ , and thus give an indication of the degree of correlation). The correlation between these two parameters is remarkable (close to a 1:1 correlation), which strongly indicates that the shift of the  $^{29}\text{Si}$  peaks as a function of temperature and the static disorder at 298 K have the exact same chemical origin.

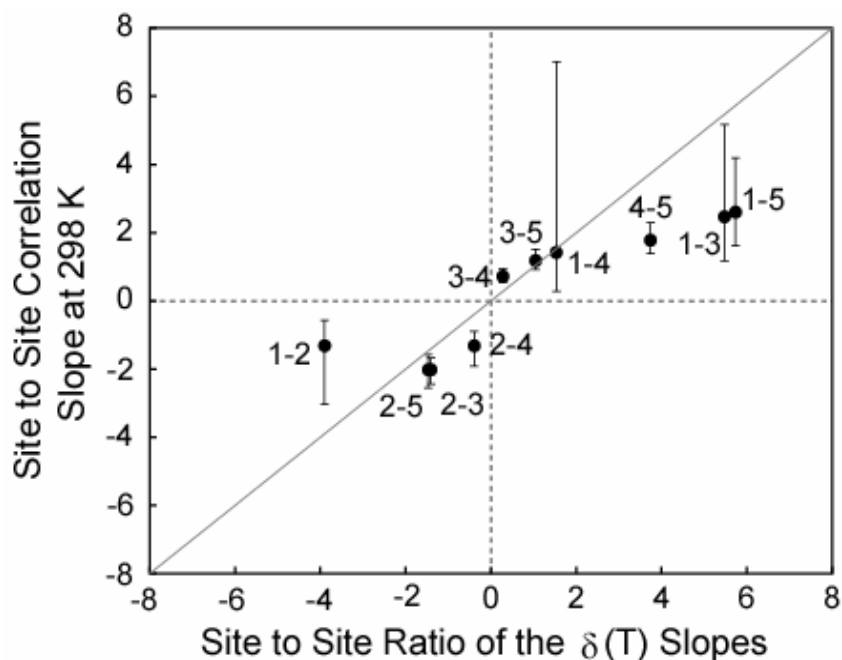


**Figure B.18.** Correlation plot between the ratio  $a_i/a_j$  ( $i > j$ ) of the linear slopes associated with the chemical shift variations of sites  $i$  and  $j$  as a function of temperature on the one hand, and the chemical shift correlation function between sites  $i$  and  $j$  obtained from 2D spectra at 298 K on the other hand. The “error” bars correspond to the slopes extracted from  $M_1$  and  $M_2$  matrices, and give an indication of the inverse of the degree of correlation for the  $(i, j)$  pair considered.

Although the temperature-dependent shifts in figure B.16 were considered linear in the above analysis, the chemical shift variations are in fact stronger between the temperature interval 260 to 290 K (shaded in grey in figure B.16). This temperature regime corresponds remarkably well to the critical temperature regime observed for the linewidths (see section B.2) as well as to the intermediate chemical-exchange regime of the surfactant headgroups discussed in section B.3.

Therefore, complementary information provided by the different analysis here suggest that the static disorder at ambient temperature, and the temperature-dependent shift and broadening of the  $^{29}\text{Si}$  NMR peaks arise from a single physical

process, which is likely related to the freezing of the surfactant motions around 270 K.

The exact nature of this process has not clearly been demonstrated here, but this study nevertheless provides a strong basis for a detailed analysis of its physical origins. Further investigations involving different sample compositions and preparation are on the way, which should hopefully answer to this question, and thus provide crucial information on how the synthetic conditions affect the molecular-level order of this class of layered materials.

In the following, we will see if the measurement of  ${}^2J({}^{29}\text{Si-O-}{}^{29}\text{Si})$  couplings can give some more information concerning this study.

### **B.4.3. Measuring ${}^2J({}^{29}\text{Si-O-}{}^{29}\text{Si})$ couplings in solid-state NMR**

#### **B.4.3.1. Introduction**

Because of the broad inhomogeneous chemical shift distributions arising from structural disorder which refocuses during a spin-echo, thus leading to long transverse dephasing times  $T_2'$  compared to the apparent dephasing time  $T_2^*$ ,  $J$  couplings can be measured in disordered solids<sup>18</sup>. However, this has so far essentially been exploited to observe the modulation of the integrated intensity of a given site under the effects of all its  $J$ -coupled neighbors. Nevertheless, a broad

chemical shift distribution resulting from a distribution of local environments, such as slightly distorted bond angles or dihedral angles, naturally also corresponds to distributions of  $J$ -coupling constants between the observed site and the connected neighbors.

Though it seems reasonable that  $J$ -coupling distributions may exist in disordered solids, few experimental observations have been reported so far. Fayon *et al.* have reported a distribution of  ${}^2J_{\text{PP}}$ -coupling constants along the barely resolved multi-site  ${}^{31}\text{P}$  chemical shift distribution in a phosphate glass<sup>12</sup>.  $J$ -coupling variations along slightly overlapped  ${}^{31}\text{P}$  sites have clearly been observed along the chemical shift distribution in  $J$ -resolved experiments, resulting in a more or less continuous  $J$ -coupling distribution. Massiot *et al.*<sup>73</sup> recently reported a site-specific  $J$ -coupling distribution in fully  ${}^{29}\text{Si}$ -enriched silicates using a  $J$ -resolved experiment. Variable splitting (in the  $J$ -resolved dimension) was observed due to variations in the  ${}^2J({}^{29}\text{Si}-\text{O}-{}^{29}\text{Si})$ -couplings along the broad peak corresponding to the  $\text{Q}^3$  sites in the direct ( ${}^{29}\text{Si}$  chemical-shift) dimension. However, though observed for a single site, this  $J$ -distribution was not specific of a single pair of sites. Indeed, in such a fully- ${}^{29}\text{Si}$ -enriched material,  $\text{Q}^3$  sites are (by definition) linked to 3 distinct  ${}^{29}\text{Si}$  sites via siloxane bridges, with potentially different associated  $J$ -coupling constants<sup>75</sup>, and the reported  $J$  values were thus averaged over several  $J$  couplings.

Recently it was demonstrated that two-dimensional  $J$ -coupling distributions can be measured using pseudo-3D methods combining refocused INADEQUATE spectra with a variable length spin echo that yields a third  $J$ -coupling dimension. Using this approach, distributions of  ${}^1J({}^{13}\text{C}-{}^{13}\text{C})$  and  ${}^2J({}^{31}\text{P}-\text{O}-{}^{31}\text{P})$  couplings have been observed in slightly disordered systems<sup>76</sup>.

In the following, we will show that a distribution can be observed between a single pair of sites in the sample, which is referred to in the following as a pair-specific J-coupling distribution.

### B.4.3.2. Experimental

To overcome this previous problem, a combination of a selective through-bond DQ filter and the z-filtered IPAP experiment was employed to overcome complications from partial  $^{29}\text{Si}$  enrichment and multiple couplings, respectively, using the pulse sequence shown in figure B.19a<sup>75</sup>. The selective DQ-filter first enables to transfer the magnetization from a selectively excited  $^{29}\text{Si}$  site S (by means of a frequency-semi-selective soft pulse) through the siloxane bridges via  ${}^2J(^{29}\text{Si-O-}^{29}\text{Si})$  couplings to the  $^{29}\text{Si}$ -labelled neighbors (e.g., site 4 in the example of figure B.8c). Then, the z-filtered IPAP block provides a J-coupling echo modulation under a selected pair of  $^{29}\text{Si}$  sites including the selectively excited site S and a coupled I site, by means of a sequential combination of semi-selective  $\pi$  pulses. By incrementing the  $\tau$  delay (see figure B.19a), the intensity of the observed site I experiences a pure cosine modulation under the  $J_{\text{IS}}$  coupling, from which the coupling-constant magnitude can be extracted with good accuracy. The I spins to be monitored should be from among the resolved  $^{29}\text{Si}$  moieties that are covalently bonded via siloxane bridges to the selectively excited S spin moieties.

Two representative examples of quantitative  ${}^2J(^{29}\text{Si-O-}^{29}\text{Si})$  measurements obtained by using this sequence are shown in figures B.19b and B.19c for the non-

crystalline lamellar silicate-surfactant mesophase  $\text{CH}_3(\text{CH}_2)_{15}\text{-NMeEt}_2^+$ . The experimental points correspond to the integrated signal intensities of the  $^{29}\text{Si}$  *I*-spin site of interest, and the error bars correspond to the standard deviation calculated from the noise regions in the spectrum.

The experimental errors of the NMR spectral integral intensities were estimated as the largest of the spectral noise (one standard deviation) or twice the standard deviation of the fitted goal function. Monte Carlo error analyses were applied to estimate the errors of the determined  $^2J(^{29}\text{Si-O-}^{29}\text{Si})$  couplings or transverse dephasing  $T_2'$  times. In these a large number of similar fits were repeated with the addition of random noise (with a standard deviation equal to the experimental error bar) to the experimental data. The errors on the measured  $^2J(^{29}\text{Si-O-}^{29}\text{Si})$  coupling on  $T_2'$  were then taken as the standard deviation of the series of *J* couplings on  $T_2'$  values thus obtained. In both cases (figures B.19b and B.19c), there is no systematic error detectable from the fits, and the same was true for all measurements made.

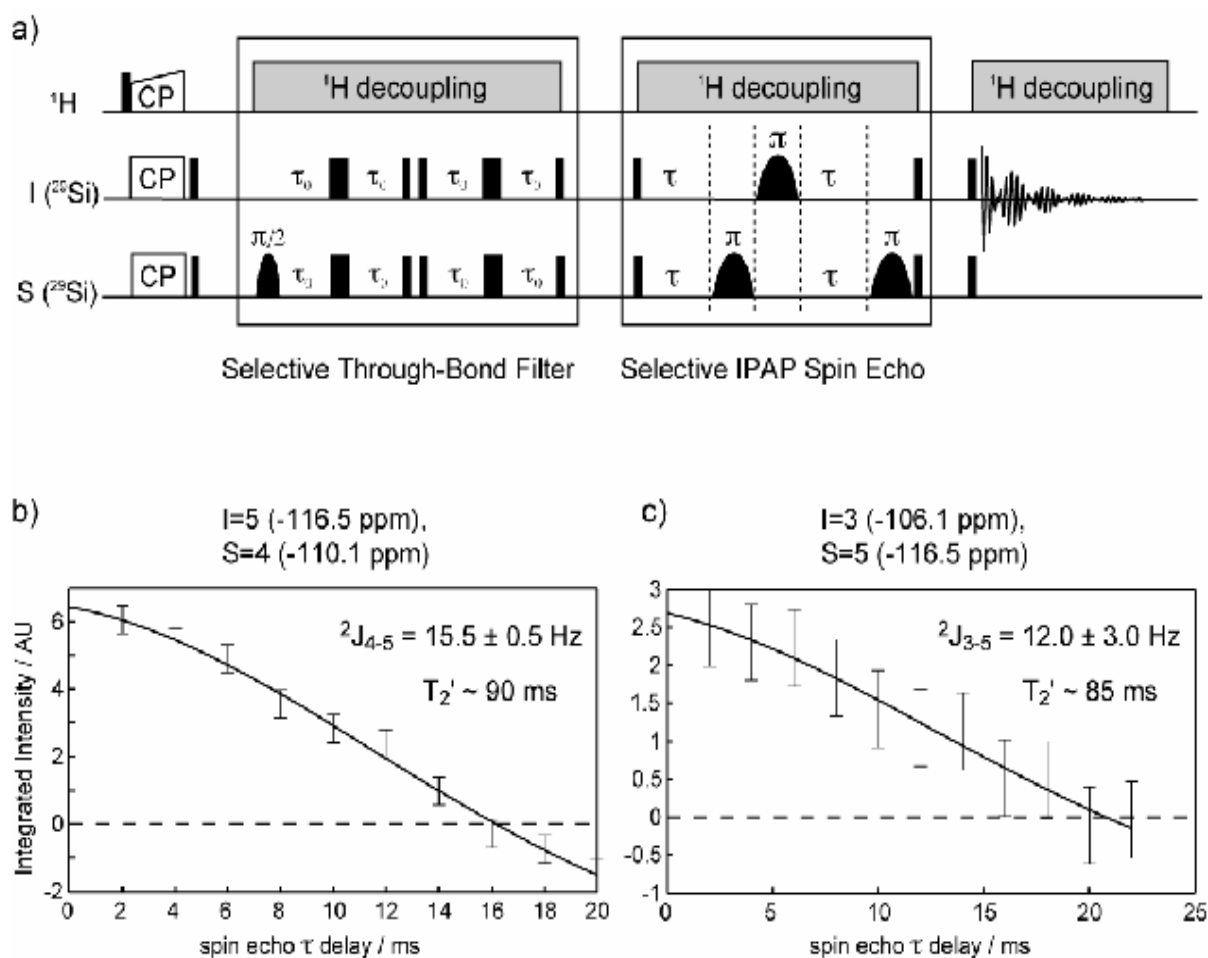


**Figure B.19.** (a) Pulse sequence of the DQ-filtered and  $z$ -filtered IPAP (DQ- $z$ -IPAP) experiment. (b) Evolution of integrated peak intensity of site 5 as a function of the  $\tau$  delay and corresponding fit to a pure cosine modulated function. The data were obtained by applying the pulse sequence described in (a) with  $I$  and  $S$  spins corresponding to sites 5 and 4 respectively. (c) Evolution of integrated peak intensity of site 5 as a function of the  $\tau$  delay and corresponding fit, with  $I$  and  $S$  spins corresponding to sites 5 and 3 respectively. The fitted values for the two-bond  $J$  coupling between the two silicon sites are indicated together with the refocused transverse dephasing time. The spinning frequency was 10 kHz and SPINAL64 heteronuclear decoupling at a proton nutation frequency of about 90 kHz was applied.

### B.4.3.3. Results and Discussion

All the results obtained for the second sample (e.g.  $\text{CH}_3(\text{CH}_2)_{15}\text{-NMeEt}_2^+$ ) are summarized in table B.3, where it can be seen that  ${}^2J_{\text{SiSi}}$  coupling constants were obtained for four of the eight types of  ${}^{29}\text{Si-O-}{}^{29}\text{Si}$  linkages in the 50%  ${}^{29}\text{Si}$ -enriched surfactant-templated silicate sample<sup>4</sup>. For the (4-5) and (3-5)  ${}^{29}\text{Si}$  spin pairs shown, the  $J$  couplings were separately measured in two different experiments by inverting the sites corresponding to the  $I$  and  $S$  spin moieties, and in these cases, both values were in excellent agreement, adding further confidence to the results.

${}^{29}\text{Si-}{}^{29}\text{Si}$ spin pair	Detected ${}^{29}\text{Si}$ spin, $I$	Excited ${}^{29}\text{Si}$ spin, $S$	${}^2J_{\text{SiSi}}$ (Hz)	$T_2'$ (ms)
4-5	4	5	$15.6 \pm 0.8$	55
	5	4	$15.5 \pm 0.5$	90
3-5	3	5	$12.0 \pm 3.0$	85
	5	3	$11.9 \pm 1.0$	100
2-5	2	5	$11.3 \pm 0.6$	85
1-5			Non measurable	
3-4			Non measurable	
2-4	2	4	$8.2 \pm 2.6$	70
1-3	1	3	< 8	
1-2			Non measurable	

**Table B.3.** Experimental  ${}^{29}\text{Si-O-}{}^{29}\text{Si}$   $J$ -coupling constants selectively measured for four tetrahedral-site pairs in a 50%  ${}^{29}\text{Si}$ -enriched surfactant ( $\text{CH}_3(\text{CH}_2)_{15}\text{-NMeEt}_2^+$ )-templated silicate with a molecularly ordered framework. The  $T_2'$  values are estimates, with uncertainties of ca.  $\pm 40$  ms, due to signal-to-noise limitations and the limited range of  $2\tau$  values used (from 2 to 48 ms).

Among the  $^{29}\text{Si-O-}^{29}\text{Si}$  spin-site pairs listed in table B.3, several are missing for different reasons that are detailed here (ignoring pairs 1-4 and 2-3 for which covalent linkages do not exist in this sample).

First, since each site-4  $^{29}\text{Si}$  is coupled to two site-3 nuclei, and each site 3 to two site-4  $^{29}\text{Si}$  nuclei, it is not possible to observe a single cosine modulation for pair 3-4. Indeed, if site 3 is the selectively excited  $^{29}\text{Si}$  site and site 4 is the detected  $^{29}\text{Si}$  moiety, the magnetization on site 4 comes from a  $^{29}\text{Si}$ -labeled site 3, but site 4 is also coupled to another site 3 that has 50% probability to be non-labeled. The consequence is a superposition of a single-cosine and a cosine-square modulation under  $J_{3-4}$  that interferes with observations of the root of the cosine modulation and makes the measurement of  $J_{3-4}$  unfeasible.

Second, no root could be observed for the  $^{29}\text{Si-O-}^{29}\text{Si}$  spin pair involving sites 1 and 5, which in this case was probably due to a short  $T_2'$  for site 1. For the 1-3  $^{29}\text{Si-O-}^{29}\text{Si}$  spin pair, which yields very weak intensity correlations in the refocused  $^{29}\text{Si}$  INADEQUATE spectrum (figure B.6) compared to the other pairs, the absence of observed zero-crossing indicates a  $J_{1-3}$ -coupling value that is significantly less than 8 Hz.

Finally, the only remaining  $^{29}\text{Si}$  spin pair involves sites 1 and 2, which cannot be accessed because of the small difference between the isotropic frequencies of these two peaks (ca. 200 Hz). Such closely spaced isotropic frequencies would require that all of the soft pulses be very long (8 ms for each  $180^\circ$  pulse and about 15 ms for the  $90^\circ$  pulse on the *S* spins), whereas for  $^{29}\text{Si-O-}^{29}\text{Si}$  pairs 2-4 and 2-5, for which only the *I* spins (site 2) required such long soft pulses, experimental conditions were already near the limit of feasible probehead high-power-decoupling tolerances.

More generally, the small differences in isotropic frequency among the different resolved resonances (from 200 to 700 Hz at 11.7 Tesla) require the use of long selective pulses, during which high power proton decoupling must be applied. These limitations, in addition to the long  $\tau_0$  delays required for coherence transfer through small  ${}^2J_{\text{SiSi}}$  couplings and the long contact time used for CP, lead to particularly long high-power irradiation periods. As a result, to prevent probehead damage, long z-filters (500 ms each) without heteronuclear decoupling were applied after CP and between the DQ-filter and the IPAP block, and an additional shorter z-filter (50 ms) was inserted before acquisition.

Previous observations of Harris and co-workers in the characterization of aqueous  ${}^{29}\text{Si}$ -enriched silicate anions in liquid-state  ${}^{29}\text{Si}$  NMR measurements reported no clear correlation between  ${}^{29}\text{Si}$   $J$ -couplings and extent of silicate site condensation<sup>77</sup>. The  ${}^2J({}^{29}\text{Si-O-}{}^{29}\text{Si})$ -coupling values reported in the literature for silicate anions in solution, which range between 3.6 and 10.2 Hz<sup>77-83</sup>, are significantly smaller than the values obtained here (except for  ${}^2J_{2-4}$ ,  ${}^2J_{1-5}$ , and  ${}^2J_{2-3}$ ), which may be due to solvent or internal motions effects. Renewed interest has very recently emerged for the characterization of silicate anions in solution<sup>84, 85</sup>, and new structures have been proposed with the help of quantum mechanical methods. The  ${}^2J_{\text{SiSi}}$  scalar coupling constants reported in references 84 and 85 (and the values and structures reported by Harris and coworkers<sup>77</sup>) are expected to be useful as a database for establishing  $J$  coupling constant trends, as functions of the local structure, either empirically or by using *ab initio*  $J$ -coupling calculations, since significant progress has been made in these areas<sup>86, 87</sup>.

Nevertheless, in solids, variations in the local geometries of relatively static Si-O-Si framework fragments and ligands, especially Si-O-Si bond angles and Si-Si distances, are expected to dominate the variation in  $^{29}\text{Si}$   $J$ couplings between different sites.

#### **B.4.4. Distribution of $^2J_{\text{SiSi}}$ Couplings: Results and Interpretation**

This approach can be implemented on the basis of the DQf-zf-IPAP experiment shown in figure B.19a. A double-quantum evolution period is inserted between the two subsequent  $\pi/2$  pulses of the DQ-filter block, as shown in figure B.20a. Applied to the surfactant-templated layered silicate, a 2D  $^2J(^{29}\text{Si-O-}^{29}\text{Si})$  coupling distribution is expected, for a selected pair of  $^{29}\text{Si}$  sites, along the 2D chemical shift dispersion of a cross peak (figure B.5b).

Figures B.20b to B.20e shows the result obtained by using the pulse sequence of figure B.20a, the selectively excited site  $S$  being the  $^{29}\text{Si}$  site 5, and the detected site  $I$  being the  $^{29}\text{Si}$  site 4. One 2D spectrum has been obtained for each value of the half-spin-echo delay  $\tau$ , in which a single 4-5 cross peak is observed at the frequency of the detected  $^{29}\text{Si}$  site 4. The intensity of the experimental cross peak is converted from double quantum – single quantum to a single quantum – single quantum representation using a shearing transformation<sup>46, 88</sup> as shown in figure B.21. The intensity distribution is modulated under the  $J_{4-5}$  coupling as a function of  $\tau$ , and this

modulation is modeled with a damped cosine function for every point in the 2D cross peak in order to extract the  $J$ -coupling constant, whose value is reported in the two-dimensional plot of figure B.20b. Figures B.20d and B.20e shows two examples of the  $J$ -coupling modulations for two distinct points in the 2D cross peak, with the corresponding best fit to a function:

$$I(\tau) = A \cos(2\pi J\tau) \exp(-2\tau T_2')$$

The observation of the two-dimensional  $J_{4-5}$  coupling plot of figure B.20b shows a significant variation in the  ${}^2J({}^{29}\text{Si-O-}{}^{29}\text{Si})$  coupling distribution. The bottom-left area of this plot in particular, which corresponds to local environments that result in high frequencies of both sites 4 and 5 yields significantly smaller coupling constants (c.a.  $13.0 \pm 0.8$  Hz) than in the central area of the peak (c.a.  $14.8 \pm 0.2$  Hz).  $J$  couplings are in most cases sensitive to highly local geometry effects<sup>89, 90</sup>.

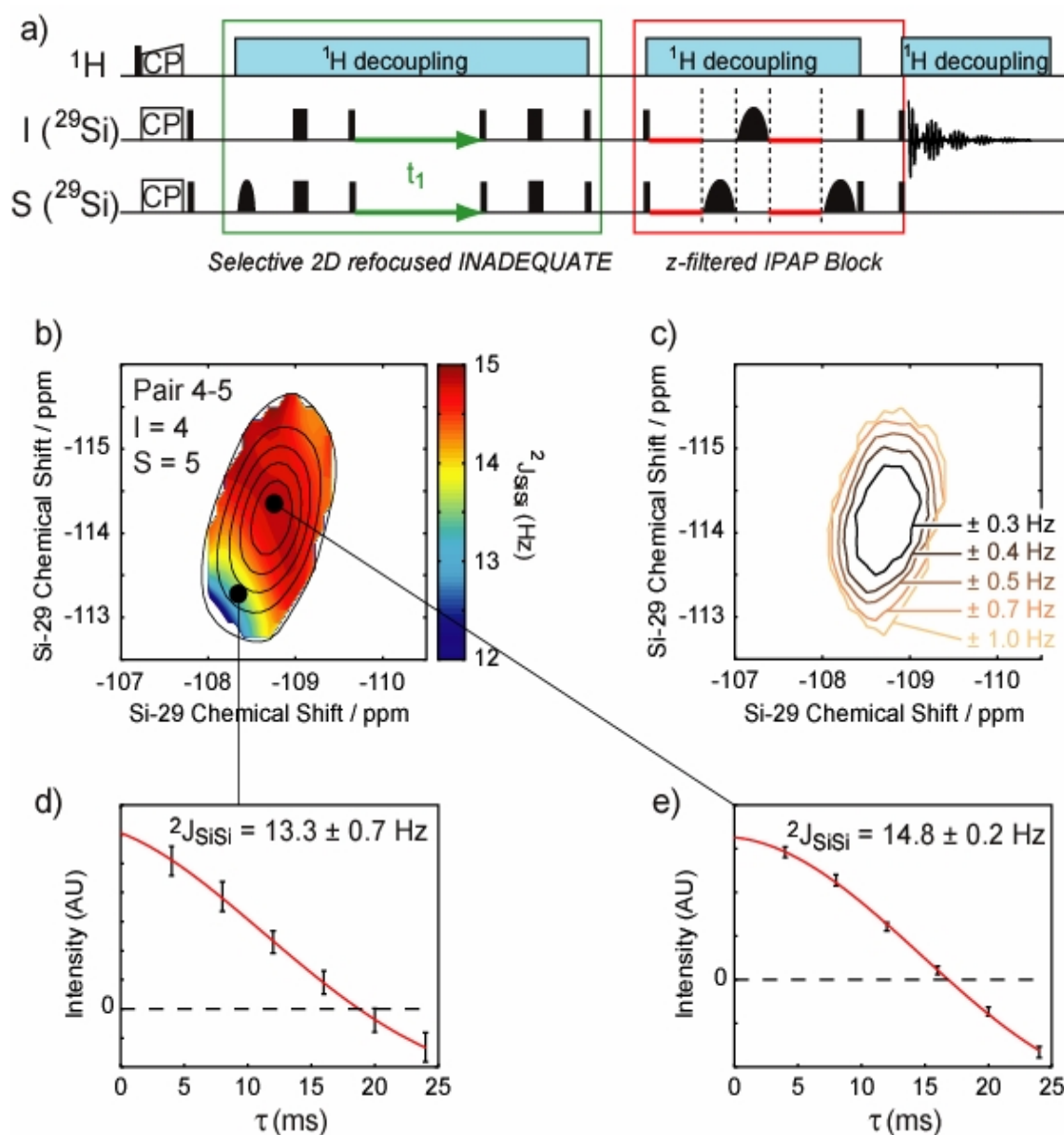


**Figure B.20.** (a) Pulse sequence of the (DQf-zf-) IPAP sequence for measuring selectively 2D  $J$ -coupling distributions in multispin solids.  $I$  and  $S$  designate two nuclei of the same type. (b) 2D  $^{29}\text{Si}\{^{29}\text{Si}\}$  NMR spectrum obtained by applying the pulse sequence shown in (a) to the sample 50%  $^{29}\text{Si}$ -enriched surfactant-templated silicate, selectively exciting  $^{29}\text{Si}$  site 5 ( $S$  spin) and detecting  $^{29}\text{Si}$  site 4 ( $I$  spin). It shows the  $^2J_{4-5}$  coupling obtained by model fitting the spin-echo modulation as a function of  $\tau$  for every point in the 2D 4-5 cross peak, as a function of the SQ frequencies in  $F_1$  and  $F_2$ . (c) Two-dimensional plot of the errors on the

$^2J(^{29}\text{Si-O-}^{29}\text{Si})$  couplings, calculated for every point in the 2D cross peak. In (d) and (e), are two examples of the spin-echo modulations and associated fits from which the J-coupling values in (b) were obtained, at the frequencies (-114.4, -108.8) and (-113.3, -108.3) respectively.

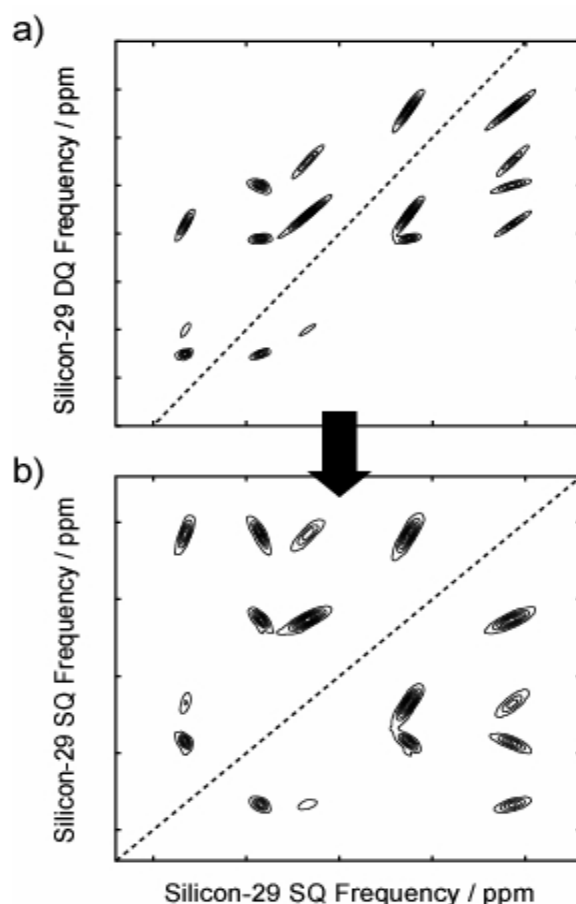


**Figure B.21.** (a) zfr-INADEQUATE spectrum of the silicate layers (same as in figure B.5b), with a lowest contour level of 8%. (b) SQ-SQ spectrum obtained by applying a shearing transformation to the zfr-INADEQUATE spectrum in (a). Pairs of cross peaks are here symmetric with respect to the diagonal.

Therefore, the observation of a distribution of  $^2J(^{29}\text{Si-O-}^{29}\text{Si})$  couplings between these two tetrahedrally condensed  $Q^4$   $^{29}\text{Si}$  sites suggests that the elongated

2D lineshapes (at 298 K) could arise from slight local static distortions of the silicate structure. In particular, these subtle structural distortions could be associated with the modulation of curvature of the silicate layers on a length scale of tens of nanometers that has been observed from transmission electron micrographs of a similar sample reported elsewhere. However, the influence of the presence of adsorbed solvent molecules, or electrostatic effects due to the proximity of the cationic surfactant headgroup on the electron spin density at the  $^{29}\text{Si}$  nuclei could potentially both affect the chemical shifts and the often dominant Fermi-contact contribution to the isotropic  $J$  coupling. This important issue is currently under study, through the use of various synthesis conditions and sample compositions in particular and still doesn't provide any important information.

## B.5. Conclusion

In this part, temperature-dependent  $^{29}\text{Si}$  NMR studies of short-range ordered surfactant templated layered silicate materials prepared with 50% enrichment in  $^{29}\text{Si}$  are reported. On the basis of two-dimensional NMR, the effects of homogeneous and inhomogeneous broadening have been differentiated. This allowed the quantitative characterization of the templating surfactant headgroup motions at the interface of the silicate layers ( $\Delta_r G^\ddagger = 58.8 \pm 0.3 \text{ kJ.mol}^{-1}$ ) through  $^{29}\text{Si}$  transverse dephasing time ( $T_2'$ ) measurements as a function of temperature, thus demonstrating that the  $T_2'$  can in some cases be used as a probe of dynamics in solid-state NMR.

Then the slight static disorder responsible for the observation of elongated 2D lineshapes has been probed by the means of  ${}^2J({}^{29}\text{Si}-\text{O}-{}^{29}\text{Si})$  distribution measurements. In the case of disordered solids, we have demonstrated the robustness of  $J$ -coupling measurements by spin-echo modulation with respect to the presence of a  $J$  distribution. In addition, we have shown that two-dimensional (2D)  $J$ -coupling distributions can be obtained from pseudo-three-dimensional approaches that combine the high resolution lineshapes of  $J$ -mediated correlation spectra to the high sensitivity of the  $J$ -couplings to the structural information. These methods open new fields for the characterization of the structural disorder with the help of  $J$  couplings complementary to the chemical shift distributions.

Finally, a detailed cross analysis of the temperature-dependent shifts and broadening of the  ${}^{29}\text{Si}$  NMR lines and the static disorder at ambient temperature strongly indicates that these phenomena all arise from a single chemical process, which is likely to be related the freezing of the surfactant headgroup motions.

Further investigations are on the way that should hopefully allow discrimination between slight mechanical distortions of the silicate layers due to expansion/contraction of the surfactant domains, dispersion of electrostatic environment at the interface, involving both the cations, surfactant headgroups and solvent used for the synthesis of these fundamentally interesting and technologically important materials.

Deuterium experiments have been carried out by Chmelka *et al.*<sup>91</sup> on similar samples prepared with deuterated surfactant headgroups  $-\text{N}(\text{CD}_3)_2(\text{CH}_2\text{CH}_3)^+$ , where

lineshape analysis have revealed the presence of a two-site jump of the surfactant headgroup.

## B.6. References

1. Salmon, P.S.; Martin, R.A.; Mason P.E.; Cuello, G.J., Topological versus chemical ordering in network glasses at intermediate and extended length scales. *NATURE*. 2005, 435 (7038), 75-78.
2. Kumar, R.; Mager, R.; Phillipp, F.; Zimmermann, A.; Rixecker, G., High-temperature deformation behavior of nanocrystalline precursor-derived Si-B-C-N ceramics in controlled atmosphere. *Int. J. Mat. Research*. 2006, 97 (5), 626-631.
3. Preezant, Y.; Tessler, N., Carrier heating in disordered organic semiconductors. *Phys. Rev. B*. 2006, 74 (23), 235202.
4. Hahn, H.; Chakraborty, A.K.; Das, J.; Pople, J.A.; Balsara, N.P., Order-disorder transitions in cross-linked block copolymer solids. *Macromolecules*. 2005, 38 (4), 1277-1285.
5. Saalwachter, K.; Heuer, A., Chain dynamics in elastomers as investigated by proton multiple-quantum NMR. *Macromolecules*. 2006, 39 (9), 3291-3303.
6. Schmidt-Rohr, K.; Spiess, H.W., *Multi-dimensional solid-state NMR and polymers*. Academic Press, San Diego, 1994.
7. DeAzevedo, E.R.; Tozoni, J.R.; Schmidt-Rohr, K.; Bonagamba, T.J., Analysis of one-dimensional pure-exchange NMR experiments for studying dynamics with broad distributions of correlation times. *J. Chem. Phys.* 2005, 122 (15), 154506-154516.
8. Stebbins, J.F.; Xu, Z, NMR evidence for excess non-bridging oxygen in an aluminosilicate glass. *Nature*. 1997, 390 (6655), 60-62.
9. Farnan, I.; Grandinetti, P.J.; Baltisberger, J.H.; Stebbins, J.F.; Werner, U.; Eastman, M.A.; Pines, A. Quantification of the disorder in network-modified silicate-glasses. *Nature*. 1992, 358 (6381), 31-35.
10. Clark, T.M.; Grandinetti, P.J., Dependence of bridging oxygen O-17 quadrupolar coupling parameters on Si-O distance and Si-O-Si angle. *J. Phys.-Condes. Matter*. 2003, 15 (31), S2387-S2395.

11. Alonso, B.; Massiot, D., Multi-scale NMR characterisation of mesostructured materials using H-1 → C-13 through-bond polarisation transfer, fast MAS, and H-1 spin diffusion. *J. Magn. Reson.* 2003, 163 (2), 347-352.
12. Fayon, F.; King, I.J.; Harris, R.K.; Evans, J.S.O.; Massiot, D., Application of the through-bond correlation NMR experiment to the characterization of crystalline and disordered phosphates. *C. R. Chim.* 2004, 7 (3-4), 351-361.
13. Massiot, D.; Fayon, F.; Alonso, B.; Trebosc, J.; Amoureux, J.P., Chemical bonding differences evidenced from J-coupling in solid state NMR experiments involving quadrupolar nuclei. *J. Magn. Reson.* 2003, 164 (1), 160-164.
14. Sakellariou, D.; Brown, S.P.; Lesage, A.; Hediger, S.; Bardet, M.; Meriles, C.A.; Pines, A.; Emsley, L., High-resolution NMR correlation spectra of disordered solids. *J. Am. Chem. Soc.* 2003, 125 (14), 4376-4380.
15. Fayon, F.; Le Saout, G.; Emsley, L.; Massiot, D., Through-bond phosphorus-phosphorus connectivities in crystalline and disordered phosphates by solid-state NMR. *Chem. Commun.* 2002, 16, 1702-1703.
16. Kaji, H.; Schmidt-Rohr, K., Selective observation and quantification of amorphous trans conformers in doubly C-13-labeled poly(ethylene terephthalate), PET, by zero-quantum magic-angle-spinning solid-state NMR. *Macromolecules.* 2002, 35 (21), 7993-8004.
17. Hedin, N.; Graf, R.; Christiansen, S.C.; Gervais, C.; Hayward, R.C.; Eckert, J.; Chmelka, B.F., Structure of a surfactant-templated silicate framework in the absence of 3D crystallinity. *J. Am. Chem. Soc.* 2004, 126 (30), 9425-9432.
18. Lesage, A.; Bardet, M.; Emsley, L., Through-bond carbon-carbon connectivities in disordered solids by NMR. *J. Am. Chem. Soc.* 1999, 121 (47), 10987-10993.
19. Nishiyama, Y.; Langan, P.; Chanzy, H., Crystal structure and hydrogen-bonding system in cellulose 1 beta from synchrotron X-ray and neutron fiber diffraction. *J. Am. Chem. Soc.* 2002, 124 (31), 9074-9082.
20. Elena, B.; Emsley, L., Powder crystallography by proton solid-state NMR spectroscopy. *J. Am. Chem. Soc.* 2005, 127 (25), 9140-9146.
21. Brouwer, D.H.; Darton, R.J.; Morris, R.E.; Levitt, M.H., A solid-state NMR method for solution of zeolite crystal structures. *J. Am. Chem. Soc.* 2005, 127 (29), 10365-10370.
22. Elena, B.; Pintacuda, G.; Mifsud, N.; Emsley, L., Molecular structure determination in powders by NMR crystallography from proton spin diffusion. *J. Am. Chem. Soc.* 2006, 128 (29), 9555-9560.
23. Hodgkinson, P.; Emsley, L., Numerical simulation of solid-state NMR experiments. *Prog. Nucl. Magn. Reson. Spectrosc.* 2000, 36 (3), 201-239.

24. Bak, M.; Rasmussen, J.T.; Nielsen, N.C., SIMPSON: A general simulation program for solid-state NMR spectroscopy. *J. Magn. Reson.* 2000, 147 (2), 296-330.
25. Veshtort, M.; Griffin, R.G., SPINEVOLUTION: A powerful tool for the simulation of solid and liquid state NMR experiments. *J. Magn. Reson.* 2006, 178 (2), 248-282.
26. Epping, J.D.; Chmelka, B.F., Nucleation and growth of zeolites and inorganic mesoporous solids: Molecular insights from magnetic resonance spectroscopy. *Curr. Opin. Colloid. In.* 2006, 11, 81-117.
27. Christiansen, S.C.; Zhao, D.Y.; Janicke, M.T.; Landry, C.C.; Stucky, G.D.; Chmelka, B.F., Molecularly ordered inorganic frameworks in layered silicate surfactant mesophases. *J. Am. Chem. Soc.* 2001, 123, 4519-4529.
28. Terao, T.; Miura, H.; Saika, A., High-resolution J-resolved NMR-spectra of dilute spins in solids. *J. Chem. Phys.* 1981, 75 (3), 1573-1574.
29. Zilm, K.W.; Grant, D.M., High-resolution NMR-spectra with J-couplings in solids. *J. Magn. Reson.* 1982, 48 (3), 524-526.
30. Early, T.A.; John, B.K.; Johnson, L.F., Observation of homonuclear double-quantum correlations in plastic crystals using cross polarization and magic-angle spinning. *J. Magn. Reson.* 1987, 75 (1), 134-138.
31. Gay, I.D.; Jones, C.H.W.; Sharma, R.D., INADEQUATE in the solid-state homonuclear couplings in  $[(\text{CH}_3)_2\text{SNE}]_3$ . *J. Magn. Reson.* 1991, 91 (1), 186-189.
32. Pines, A.; Gibby, M.G.; Waugh, J.S., Proton-enhanced NMR of dilute spins in solids. *J. Chem. Phys.* 1973, 59 (2), 569-590.
33. Benn, R.; Grondey, H.; Brevard, C.; Pagelot, A., The detection of connectivities of rare spin-1/2 nuclei in the solid-state using natural abundance samples C-13 and Si-29 INADEQUATE and COSY type experiments. *J. Chem. Soc.-Chem. Commun.* 1988, 2, 102-103.
34. Fyfe, C.A.; Gies, H.; Feng, Y., Demonstration of 3-dimensional lattice connectivities in zeolites by two-dimensional high-resolution solid-state NMR-spectroscopy. *J. Chem. Soc.-Chem. Commun.* 1989, 17, 1240-1242.
35. Fyfe, C.A.; Gies, H.; Feng, Y., 3-dimensional lattice connectivities from two-dimensional high-resolution solid-state NMR Si-29 MAS NMR investigation of the silicate lattice of zeolite ZSM-39 (dodecasil-3C). *J. Am. Chem. Soc.* 1989, 111 (20), 7702-7707.
36. Fyfe, C.A.; Gies, H.; Feng, Y.; Kokotailo, G.T., Determination of 3-dimensional lattice connectivities in zeolites using natural abundance Si-29 two-dimensional NMR and the direct observation of Si-29-O-Si-29 couplings. *Nature* 1989, 341 (6239), 223-225.

37. Knight, C.T.G.; Kirkpatrick, R.J.; Oldfield, E., The connectivity of silicon sites in silicate-glasses, as determined by 2-dimensional Si-29 NMR spectroscopy. *J. Non-Cryst. Solids*. 1990, 116 (2-3), 140-144.
38. Sakellariou, D.; Emsley, L., Through-bond experiments in solids; *Encyclopaedia of NMR*, Grant, D. M.; Harris, R. K. Wiley, London, 2002, 196-211.
39. Bax, A.; Freeman, R.; Frenkiel, T.A., An NMR technique for tracing out the carbon skeleton of an organic molecule. *J. Am. Chem. Soc.* 1981, 103 (8), 2102-2104.
40. Lesage, A.; Auger, C.; Caldarelli, S.; Emsley, L., Determination of through-bond carbon-carbon connectivities in solid-state NMR using the INADEQUATE experiment. *J. Am. Chem. Soc.* 1997, 119 (33), 7867-7868.
41. Maudsley, A.A.; Wokaun, A.; Ernst, R.R., Coherence transfer echoes. *Chem. Phys. Lett.* 1978, 55 (1), 9-14.
42. Verel, R.; van Beek, J.D.; Meier, B.H., INADEQUATE-CR experiments in the solid state. *J. Magn. Reson.* 1999, 140 (1), 300-303.
43. Nielsen, N.C.; Thogersen, H.; Sorensen, O.W., Doubling the sensitivity of INADEQUATE for tracing out the carbon skeleton of molecules by NMR. *J. Am. Chem. Soc.* 1995, 117 (45), 11365-11366.
44. Mueller, L.J.; Elliott, D.W.; Kim, K.C.; Reed, C.A.; Boyd, P.D.W., Establishing through-bond connectivity in solids with NMR: Structure and dynamics in HC60+. *J. Am. Chem. Soc.* 2002, 124 (32), 9360-9361.
45. Fayon, F.; King, I.J.; Harris, R.K.; Gover, R.K.B.; Evans, J.S.O.; Massiot, D., Characterization of the room-temperature structure of SnP2O7 by P-31 through-space and through-bond NMR correlation spectroscopy. *Chem. Mat.* 2003, 15 (11), 2234-2239.
46. Cadars, S.; Lesage, A.; Emsley, L., Chemical shift correlations in disordered solids. *J. Am. Chem. Soc.* 2005, 127 (12), 4466-4476.
47. Olsen, R.A.; Struppe, J.; Elliott, D.W.; Thomas, R.J.; Mueller, L.J., Through-bond C-13-C-13 correlation at the natural abundance level: Refining dynamic regions in the crystal structure of vitamin-D-3 with solid-state NMR. *J. Am. Chem. Soc.* 2003, 125 (39), 11784-11785.
48. Fayon, F.; Roiland, C.; Emsley, L.; Massiot, D., Triple-quantum correlation NMR experiments in solids using J-couplings. *J. Magn. Reson.* 2006, 179 (1), 49-57.
49. Duma, L.; Hediger, S.; Lesage, A.; Emsley, L., Spin-state selection in solid-state NMR. *J. Magn. Reson.* 2003, 164 (1), 187-195.

50. Duma, L.; Hediger, S.; Brutscher, B.; Bockmann, A.; Emsley, L., Resolution enhancement in multidimensional solid-state NMR spectroscopy of proteins using spin-state selection. *J. Am. Chem. Soc.* 2003, 125 (39), 11816-11817.
51. Bermel, W.; Bertini, I.; Duma, L.; Felli, I.C.; Emsley, L.; Pierattelli, R.; Vasos, P.R., Complete assignment of heteronuclear protein resonances by protonless NMR spectroscopy. *Angew. Chem.-Int. Edit.* 2005, 44 (20), 3089-3092.
52. Brown, S.P.; Perez-Torralba, M.; Sanz, D.; Claramunt, R.M.; Emsley, L., The direct detection of a hydrogen bond in the solid state by NMR through the observation of a hydrogen-bond mediated N-15-N-15 J coupling. *J. Am. Chem. Soc.* 2002, 124 (7), 1152-1153.
53. Grasso, G.; de Swiet, T.M.; Titman, J.J., Electronic structure of the polymer phase of CsC60: Refocused INADEQUATE experiments. *J. Phys. Chem. B.* 2002, 106 (34), 8676-8680.
54. De Paepe, G.; Giraud, N.; Lesage, A.; Hodgkinson, P.; Bockmann, A.; Emsley, L., Transverse dephasing optimized solid-state NMR spectroscopy. *J. Am. Chem. Soc.* 2003, 125 (46), 13938-13939.
55. Kono, H.; Numata, Y.; Erata, T.; Takai, M., C-13 and H-1 resonance assignment of mercerized cellulose II by two-dimensional MAS NMR spectroscopies. *Macromolecules.* 2004, 37 (14), 5310-5316.
56. Pham, T.N.; Masiero, S.; Gottarello, G.; Brown, S.P., Identification by N-15 refocused inadequate MAS NMR of intermolecular hydrogen bonding that directs the self-assembly of modified DNA bases. *J. Am. Chem. Soc.* 2005, 127 (46), 16018-16019.
57. Kono, H.; Erata, T.; Takai, M., Determination of the through-bond carbon-carbon and carbon-proton connectivities of the native celluloses in the solid state. *Macromolecules.* 2003, 36 (14), 5131-5138.
58. De Paepe, G.; Lesage, A.; Steuernagel, S.; Emsley, L., Transverse dephasing optimised NMR spectroscopy in solids: Natural-abundance C-13 correlation spectra. *ChemPhysChem.* 2004, 5 (6), 869-875.
59. Harris, R.K.; Joyce, S.A.; Pickard, C.J.; Cadars, S.; Emsley, L., Assigning carbon-13 NMR spectra to crystal structures by the INADEQUATE pulse sequence and first principles computation: a case study of two forms of testosterone. *Phys. Chem. Chem. Phys.* 2006, 8 (1), 137-143.
60. Bodenhausen, G.; Kogler, H.; Ernst, R.R., Selection of coherence transfer pathways in NMR pulse experiments. *J. Magn. Reson.* 1984, 58 (3), 370-388.
61. Geen, H.; Freeman, R., Band selective radiofrequency pulses. *J. Magn. Reson.* 1991, 93 (1), 93-141.

62. Bennett, A. E.; Rienstra, C. M.; Auger, M.; Lakshmi, K. V.; Griffin, R. G., Heteronuclear decoupling in rotating solids. *J. Chem. Phys.* 1995, 103 (16), 6951-6958.
63. Detken, A.; Hardy, E. H.; Ernst, M.; Meier, B. H., Simple and efficient decoupling in magic-angle spinning solid-state NMR: the XiX scheme. *Chem. Phys. Lett.* 2002, 356 (3-4), 298-304.
64. Fung, B. M.; Khitrin, A. K.; Ermolaev, K., An improved broadband decoupling sequence for liquid crystals and solids. *J. Magn. Reson.* 2000, 142 (1), 97-101.
65. De Paepe, G.; Elena, B.; Emsley, L., Characterization of heteronuclear decoupling through proton spin dynamics in solid-state nuclear magnetic resonance spectroscopy. *J. Chem. Phys.* 2004, 121 (7), 3165-3180.
66. Langan, P.; Nishiyama, Y.; Chanzy, H., X-ray structure of mercerized cellulose II at 1 angstrom resolution. *Biomacromolecules.* 2001, 2 (2), 410-416.
67. Nishiyama, Y.; Sugiyama, J.; Chanzy, H.; Langan, P., Crystal structure and hydrogen bonding system in cellulose 1(alpha), from synchrotron X-ray and neutron fiber diffraction. *J. Am. Chem. Soc.* 2003, 125 (47), 14300-14306.
68. Brown, S. P.; Emsley, L., The 2D MAS NMR spin-echo experiment: the determination of C-13-C-13 J couplings in a solid-state cellulose sample. *J. Magn. Reson.* 2004, 171 (1), 43-47.
69. Leigh, J.S.Jr., Relaxation times in systems with chemical exchange: some exact solutions. *J. Magn. Reson.* 1971, 4, 308-311.
70. Jen, J., Chemical exchange and NMR T<sub>2</sub> relaxation – the multisite case. *J. Magn. Reson.* 1978, 30, 111-128.
71. Bain, A.D., Chemical exchange in NMR. *Prog. in Nucl. Magn. Reson. Spec.* 2003, 43, 63-103.
72. Harris R.K., Nuclear magnetic resonance spectroscopy. Longman, Harlow, 1986.
73. Massiot, D.; Fayon, F.; Montouillout, V.; Iuga, D.; Morais, C.; Gan, Z., J-coupling based homo- and hetero-nuclear correlations involving quadrupole in crystalline and amorphous solids. 4th Alpine Conference on Solid-State NMR. 2005.
74. Hohwy, M.; Jakobsen, H.J.; Eden, M.; Levitt, M.H.; Nielsen, N.C., Broadband dipolar recoupling in the nuclear magnetic resonance of rotating solids: A compensated C7 pulse sequence. *J. Chem. Phys.* 1998, 108, 2686-2694.
75. Cadars, S.; Lesage, A.; Hedin, N.; Chmelka, B.F.; Emsley, L., Selective NMR measurements of homonuclear scalar couplings in isotopically enriched solids. *J. Phys. Chem. B.* 2006, 110 (34), 16982-16991.

76. Cadars S.; Lesage A.; Trierweiler M.; Heux, L.; Emsley, L., NMR measurements of scalar-coupling distributions in disordered solids. *Phys. Chem. Chem. Phys.* 2007, 9(1), 92-103.
77. Harris, R.K.; Knight, C.T.G., Si-29 nuclear magnetic resonance studies of aqueous silicate solutions. 6. 2<sup>nd</sup> order patterns in potassium silicate solutions enriched with Si-29. *J. Chem. Soc.-Faraday Transactions II.* 1983, 79, 1539-1561.
78. Marsmann, H.C., Silicon-29 NMR; *Encyclopaedia of NMR*, Grant, D.M.; Harris, R.K. Wiley, London, 1997; 4386-4398.
79. Harris, R.K.; Oconnor, M.J.; Curzon, E.H.; Howarth, O.W., Two dimensional Si-29 NMR studies of aqueous silicate solutions. *J. Magn. Reson.* 1984, 57 (1), 115-122.
80. Knight, C.T.G.; Kirkpatrick, R.J.; Oldfield, E., Si-29 NMR structural characterization of two novel germanosilicate cages in a tetramethylammonium germanosilicate solution. *J. Am. Chem. Soc.* 1986, 108 (1), 30-33.
81. Knight, C.T.G.; Kirkpatrick, R.J.; Oldfield, E., Si-29 2D NMR evidence of four novel doubly germanium substituted silicate cages in a tetramethylammonium germanosilicate solution. *J. Am. Chem. Soc.* 1987, 109 (6), 1632-1635.
82. Harris, R.K.; Parkinson, J.; SamadiMaybodi, A., A novel symmetric silicate anion. *J. Chem. Soc.-Dalton Trans.* 1997, 15, 2533-2534.
83. Kinrade, S.D.; Donovan, J.C.H.; Schach, A.S.; Knight, C.T.G., Two substituted cubic octameric silicate cages in aqueous solution. *J. Chem. Soc.-Dalton Trans.* 2002, 7, 1250-1252.
84. Haouas, M.; Taulelle, F., Revisiting the identification of structural units in aqueous silicate solutions by two-dimensional silicon-29 INADEQUATE. *J. Phys. Chem. B.* 2006, 110 (7), 3007-3014.
85. Cho, H.; Felmy, A.R.; Craciun, R.; Keenum, J.P.; Shah, N.; Dixon, D.A., Solution state structure determination of silicate oligomers by Si-29 NMR spectroscopy and molecular modeling. *J. Am. Chem. Soc.* 2006, 128 (7), 2324-2335.
86. Helgaker, T.; Jaszunski, M.; Ruud, K., Ab initio methods for the calculation of NMR shielding and indirect spin-spin coupling constants. *Chem. Rev.* 1999, 99 (1), 293-352.
87. Vaara, J.; Jokisaari, J.; Wasylishen, R.E.; Bryce, D.L., Spin-spin coupling tensors as determined by experiment and computational chemistry. *Prog. Nucl. Magn. Reson. Spectrosc.* 2002, 41 (3-4), 233-304.
88. Ernst, R.R.; Bodenhausen, G.; Wokaun, A., *Principles of Nuclear Magnetic Resonance in One and Two Dimensions*; Oxford Science Publications: New York, 1987.

89. Contreras, R.H.; Peralta, J.E.; Giribet, C.G.; De Azua, M.C.; Facelli, J.C., In *Annual Reports on NMR Spectroscopy*. 2000; Vol. 41, p 55-184.

90. Contreras, R.H.; Peralta, J.E., Angular dependence of spin-spin coupling constants. *Prog. Nucl. Magn. Reson. Spectrosc.* 2000, 37, 321-425.

91. Rapp, A.; Hedin, N.; Chmelka, B.F., *Personal Communication*.

## GENERAL CONCLUSION

In this manuscript it has been shown that high resolution proton solid NMR spectroscopy can be achieved using rotation of the sample at the magic-angle, that averages the spatial part of interaction Hamiltonians and coherent averaging methods for removal of residual dipolar interactions. The quality of proton homonuclear dipolar averaging is such that it should now be feasible to reach detailed information about the chemical environment of protons in solids. The enhanced performance of proton homonuclear dipolar averaging schemes discloses additional perspectives in the area of heteronuclear correlation spectroscopy, in particular for the development of selective through-bond correlation techniques via J couplings.

Thus, combining CRAMPS and INEPT methods, it is possible to assign powders of organic compounds at natural abundance to crystal structures. CRAMPS spectroscopy can be in particular implemented for recording high resolution proton spectra both in a direct or indirect dimension of NMR acquisition. In both cases, the observed proton resolution under MAS is extremely dependent on the pulse scheme

used for proton homonuclear dipolar decoupling. Moreover, as it has been illustrated in this study, NMR and quantum mechanical calculations will increasingly be used in concert. The remarkable accuracy already obtained by computational methods and the increasing complexity of the systems that can be accessed make solid-state DFT approaches in particular extremely attractive to exploit the exceptional sensitivity of NMR parameters to structure.

Then, proton-proton multidimensional correlation spectroscopy in powdered solids constantly benefits from the continuous progress in proton resolution. In this thesis, we mainly described two types of proton homonuclear correlation schemes, that involve either a double-quantum single-quantum correlation mechanism, or a polarization transfer through  $^1\text{H}$ - $^1\text{H}$  spin diffusion, driven by direct proton-proton dipolar couplings. We investigated more precisely the proton-proton spin diffusion case, and proposed a phenomenological model, based on standard complete relaxation matrix analysis and a molecular dynamics program, for simulation and structural interpretation of the proton spin-diffusion build-up curves. Within this framework, it should be possible to determine the molecular structure of small organic powders at natural abundance. Thus this approach provides us with very encouraging basis for the development of more advanced methodology, towards powder crystallography by proton high-resolution NMR spectroscopy.

In the other part of this manuscript, we have made an extensive use of through-bond correlation methods in solids, and demonstrated their utility as building blocks for the development of complicated pulse sequences that probe a given type of information in a specific way. The simplicity of spin-echo based methods, and

more specifically of the refocused INADEQUATE experiment makes them extremely conveniently inserted in multiple-pulse experiments.

In order to extend the range of systems where J-couplings can be measured and potentially provide crucial structural information, the z-filtered IPAP experiment was introduced, which enables to measure selectively and accurately J couplings in isotopically enriched multi-spin systems. Despite the limitations mentioned above, the refocused INADEQUATE has been successfully used as a selective DQ filter making the z-filtered IPAP experiment applicable to partially enriched solids as well. This was illustrated by the measurement of  $^2J(\text{Si-O-Si})$  couplings in layered silicates lacking long-range 3D crystallinity.

In the limits of high resolution, that is when the residual homogeneous contributions to the linewidths no longer dominate the 2D lineshapes obtained from disordered solids, we have shown that their information content can be analyzed in terms of conditional probability distributions. These methods open new fields for the characterization of the structural disorder with the help of  $J$  couplings complementary to the chemical shift distributions.